The Combined Impact of Ionizing Radiation and Momentum Winds from Massive Stars on Molecular Clouds

Judith Ngoumou Y Ewondo

München 2014

The Combined Impact of Ionizing Radiation and Momentum Winds from Massive Stars on Molecular Clouds

Judith Ngoumou Y Ewondo

Dissertation
an der Fakultät für Physik
der Ludwig–Maximilians–Universität
München

vorgelegt von
Judith Ngoumou Y Ewondo
aus Yaoundé, Kamerun

München, den 23.07.2014

Erstgutachter: Prof. Dr. Andreas Burkert
Zweitgutachter: Prof. Dr. Thomas Preibisch
Tag der mündlichen Prüfung: 15.10.2014

Contents

List of Figures

List of Tables

Zusammenfassung

Sternentstehung findet auf Skalen von Hunderten von Lichtjahren im inneren dichter Molekülwolken statt. Sehr unterschiedliche physikalische Prozesse spielen dabei eine Rolle. Die klumpigen Wolken besitzen komplexe, turbulente dynamische Eigenschaften. Die dichtesten Bereiche werden gravitativ instabil, kollabieren und bilden neue Sterne. Im Gegenzug beeinflussen aber auch Sterne die umgebenden Molekülwolken. Dabei spielen insbesondere massereiche Sterne - also Sterne mit mehr als das 8-fache der Masse unserer Sonne - eine wichtige Rolle.

Obwohl diese Stern-"Giganten", aus astronomischer Sicht, nur relativ kurzlebig sind (einige 10^6 Jahren), emittieren diese während ihrer Lebenszeit stark ionisierende ultraviolette (UV) Strahlung und Sternenwinde. Beobachtungen und numerische Simulationen haben gezeigt, dass diese *Feedback*-Mechanismen die Wolkenstruktur verändern. Insbesondere die UV-Strahlung der massiven Sterne, heizt die Sternumgebung auf und treibt Schockwellen durch das Gas. Dadurch werden Teile der Wolken zerstreut und zerstört, während weitere Bereiche zusammengeschoben und komprimiert werden. Eine Vielfalt an Strukturen, wie Gasblasen, Gassäulen und Filamente werden erzeugt. In den verdichteten Regionen, wie beispielsweise in den Spitzen der Gassäulen, können, gegebenenfalls, neue Sterne entstehen. Man spricht dabei von induzierter Sternentstehung.

Neben der UV-Strahlung emittieren die massereichen Sterne, aufgrund ihrer hohen Leuchtkraft, starke Winde. Diese enstehen, wenn das Material aus den äusseren Schichten des Sterns durch den Strahlungsdruck weggeblasen wird. Die Winde bestehen aus Teilchen, die mit sehr hoher Geschwindigkeit in das umgebende Gas hineinrasen.

Der Carina Nebel ist ein beeindruckendes Beispiel für den Einfluss, den massive Sterne auf ihre Umgebung haben. Mit einer Entfernung von 2.3 kpc, ist er die nächstgelegene Sternentstehungsregion mit mehr als 65 massiven O-Sterne. Beobachtungen des Nebels in einer Vielzahl von Wellenlängen, geben Aufschluss auf die dynamische Entwicklung der Region. In dieser Arbeit, wird ein kleiner Beitrag zum Verständnis der komplexen Dynamik in Sternentstehungsregionen geleistet. Insbesondere, wird untersucht, mithilfe numerischer Simulationen, welchen Einfluss der Impuls Übertrag der Winde auf die umgebende Gas-Verteilung hat. Dazu wird, in den *Smoothed Particle Hydrodynamics* (SPH) Code SEREN, ein Verfahren implementiert, welches den Wind-Impuls isotropisch auf das umgebende Gas verteilt. Dieses Verfahren kann zusammen mit dem Modul für ionisierender Strahlung benutzt werden. Dadurch können die Einflüsse der beiden Feedback Mechanismen verglichen werden.

Das Verfahren wird auf verschiedene Dichte-Verteilungen angewendet. Zum Testen unserer Methode wird der Wind in einer kalten (10 K) gleichförmig-verteilten Wolke eingesetzt. Die Expansion der entstehenden Schock Front wird mit der bekannten analytischen Lösung verglichen. Danach wird der Einfluss des Feedbacks eines O-Sterns auf eine selbstgravitative Sphäre untersucht und zuletzt wird die Entwicklung einer turbulenten Wolke unter den Einfluss des Feedbacks einer externen Quelle betrachtet. Dabei wird die Entwicklung der kalten Gasstrukturen für drei verschiedenen Feedback Fälle verglichen: i) unter den Einfluss des Windes allein, ii) unter den Einfluss der puren ionisierenden Strahlung, und iii) wenn beide Mechanismen gleichzeitig wirken. Diese Arbeit zeigt, dass die ionisierende UV-Strahlung der wichtigste Akteur in dem komplexen Zusammenspiel ist. Der Windimpuls spielt, im Vergleich zum ionisierenden Prozess, eine untergeordnete Rolle, wenn es um die Dynamik des molekularen Gases geht.

Zusätzlich, wird auch über die Beobachtung einer sichel-förmigen Struktur im Carina Nebel und eines dichten Klumpens an der gleichen Stelle, berichtet. Die Sichel wird als Spitze des Bugschocks des superschnellen Sterns *Trumpler 14 MJ 218* interpretiert. Ein möglicher Zusammenhang zwischen dem Stern, dem Sichel-Nebel und dem Klumpen wird untersucht. Die Asymmetrie des Bugschocks, weist darauf hin, dass sich der Stern durch den Dichte-Gradienten am Rande des Klumpens bewegt.

Die Ergebnisse dieser Arbeit deuten an, dass die Winde der Massenreichen Sterne eine untergeordenete Rolle spielen. Dieses Resultat, sowie die Präsenz eines superschnellen Sterns im Carina Nebel deuten an, dass die Region möglicherweise Schauplatz eines weiteren energiereichen Ereignisses, einer Supernova, gewesen ist.

Abstract

Star-formation occurs on scales of hundreds of light years inside dense molecular clouds and involves a number of physical processes. The structured clouds exhibit complex and dynamical properties. The densest regions become unstable due to their own gravity and collapse to form new stars. In return, the stars themselves affect the molecular clouds, they live in. In particular the most massive ones, with more than eight times the mass of our Sun, play an important role.

Despite their short lifetime, in astronomical terms (a few 10^6 years), they emit strong ionizing ultraviolet radiation and powerful winds. Observations and numerical simulations have shown that these *Feedback* mechanisms impact the structure of the clouds. The UV-radiation, in particular, heats up the circumstellar material and drives shocks through the gas. Parts of the clouds get dispersed and destroyed, while other regions can be swept-up and compressed. A multitude of structures like bubbles, pillars, clumps and filaments, are formed through stellar feedback mechanisms. In the compressed and densest parts of these structures, like the tips of the pillars, new stars can be formed. This is referred to as triggered star formation.

In addition to the UV-radiation, massive and very luminous stars emit powerful winds. These are made of material expelled from the outer layers of the stars by radiation pressure. The ejecta reach very high velocities and are rushed into the ambient medium.

The Carina Nebula is a particularly impressive example of the complex interaction between the feedback from massive stars and the ambient gas. Located at a distance of 2.3 kpc, it is the most nearby region with a population of more than 65 O-type stars. Multi-wavelength observations have provided a deep insight into the dynamical evolution of the region. This work addresses the "stellar feedback – cloud" interaction from the numerical side. The intention is to make a small contribution towards understanding the complex dynamics in star forming regions. For that purpose, a method is implemented, into the *Smoothed Particle Hydrodynamics* (SPH) Code SEREN, to isotropically distribute the momentum from the wind's ejecta to the circumstellar material. This method, used in conjunction with a module for ionizing radiation, allows for the study and comparison of the impact of the two types of feedback mechanisms.

The wind method is applied to different ambient gas density distributions. To begin, the implementation is tested by studying the expansion of the wind front into a cold (10 K) uniform density distribution and comparing it to the well-known analytical solution. Then, the impact of an O-type star on a self-gravitating sphere is investigated and finally the

evolution of a turbulent cloud under the impact of the feedback from an external source is considered. The evolution of the different gaseous density structures is compared for three cases of stellar feedback: i) the result of the pure momentum wind, ii) the effect of the ionizing radiation only, and iii) the combined impact of the two mechanisms. This study shows that the ionizing UV-radiation is the main agent shaping and compressing the cold gas. The momentum wind plays only a subordinate role in the dynamical evolution of the molecular gas.

Additionally, multi-wavelength observations of a crescent-shaped nebulosity and a denser molecular clump at seemingly the same location in the Carina Nebula are presented. The observed crescent-shaped nebulosity, called the "Sickle", is interpreted as the tip of a bow shock associated with the runaway star *Trumpler 14 MJ 218*. A possible link between the star, the Sickle and the clump is investigated. It is argued that the star is moving supersonically through the ambient density gradient on the front side of the observed compact clump.

The little impact of the winds of massive stars on the dynamics of molecular clouds, together with the presence of the high-velocity star *Trumpler 14 MJ 218* and the associated peculiar Sickel object, could perhaps indicate that the highly complex structure of the Carina Nebula has experienced a supernova event in its recent past.

Chapter 1

Introduction

The aim of this work is to investigate the combined impact of the ionizing radiation and the momentum output from the wind of a massive star on molecular clouds. This study was carried out in hopes of making a small contribution towards understanding the physics involved in shaping the amazingly complex Carina Nebula. This thesis is structured as follows:

In the present chapter, we intend to provide an overview of the content of the interstellar medium, as the astrophysical context for the objects and phenomena we study. We briefly present some properties of molecular clouds and their role as "stellar nurseries". We then introduce the main driving agents for the effects we investigate in this thesis: Massive stars and their winds. As an example of the beauty and complexity of the systems we observe, which ultimately drive our motivation to explore the physical mechanisms impacting their evolution, we take a look at the Carina Nebula.

After the present introduction, we continue by reviewing the theoretical framework we use in our investigation of stellar feedback-affected gas-dynamics. In chapter 2 we present the equations of hydrodynamics, which are used to describe the dynamical evolution of the interstellar gas we study. Chapter 3 addresses the analytical expressions for the expansion of stellar wind bubbles and H II regions.

A quick introduction to the numerical tools used in our simulations is given in chapter 4, where we present the *Smoothed Particle Hydrodynamics* (SPH) method. In chapter 5 we describe some aspects of the HEALPix tessellation scheme (Górski et al., 2005) and present our implementation of the HEALPix-based momentum wind scheme in the SPH code SEREN (Hubber et al., 2011).

We proceed to present the results of our investigation on the impact of momentum winds and ionizing radiation on a self-gravitating core in chapter 6, and on a structured and turbulent cloud in chapter 7. In chapter 8 we report on a particular object that caught our attention during the examination of multi-wavelength observations of the Carina Nebula. We summarize, conclude and discuss future work in chapter 9.

1.1 The Interstellar Medium

A single galaxy is made of many billions of stars. They are embedded in a tenuous environment known as the *interstellar medium* (ISM). In our Galaxy, the Milky Way, the ISM is filled with matter in the form of gas and dust (tiny solid carbon or silicate grains), relativistic charged particles known as cosmic rays and magnetic fields. Approximately 99% of the mass of the ISM is in gaseous form and the remaining 1% is composed of dust. With an average density of only about one particle per cubic centimetre, interstellar matter accounts for $\sim$ 10 - 15% of the total mass of our Galactic disc. It reveals itself through obscuration of more distant field stars, reddening and scattering of stellar light, through the presence of absorption lines in stellar spectra, and through emission mechanisms, both continuum and at specific wavelengths. The main chemical constituent of the interstellar gas is hydrogen in its various forms (ionized, atomic and molecular), existing under a wide range of physical conditions. Based on the gas' temperature and its chemical state the gaseous ISM can be classified into five thermal phases (see Table 1.1).

Component	Temperature (K)	Particle Density (cm^{-3})	Filling Factor
hot ionized	10^6	$\sim 6.5 \times 10^{-3}$	$\leq 50\%$
warm ionized	8000	0.2 - 0.5	$\geq 15\%$
warm neutral	6000 - 10000	0.2 - 0.5	$\leq 30\%$
cold atomic	50 - 100	20 - 50	≤ 2 - 4%
molecular clouds	10 - 20	10^2 - 10^6	$< 1\%$

Table 1.1: The thermal gas phases of the ISM. Adapted from Table I in Ferrière (2001) with filling factors from Brinks (1990).

1.1.1 The Gaseous Phase

The hot ionised medium (HIM): The hot, very low-density ($n < 0.003\,cm^{-3}$) gas is detected in diffuse soft X-ray emission and in absorption lines seen towards hot stars in the far-UV (e.g. O IV, N V, and C IV). The hot gas is often associated with bubbles and fountains high above the Galactic disk. It is heated by supernovae explosions to temperatures $T > 10^6\,K$. The explosions drive rapidly propagating shock waves in the ISM, which produce cavities filled with hot rarefied gas and surrounded by a colder thin and dense shell of swept up interstellar matter. The cavities eventually overlap to form superbubbles. McKee & Ostriker (1977) developed a model of the local multiphase ISM, in which about 70 % of interstellar space is filled with hot dilute gas produced in supernovae explosions. Models taking into account the effects of magnetic fields and the tendency of supernovae to be clustered and create superbubbles reduced the filling factor down to $< 20\%$ (Heiles, 1990; Ferrière, 1998).

The information contained in Section 1.1 is based on Osterbrock & Ferland (2006) and the review by Ferrière (2001). Original references to the information cited here can be found therein.

The very hot gas is ionized by collisions with electrons. At very high temperatures, processes involving inner-shell electrons become important. Double excited states and autoionization processes might occur. The hot plasma is heated primarily by mechanical input of energy, either from supernova blast waves or hot superwinds from massive stars (e.g., Wolf-Rayet stars). Cooling in a hot, collisionally-ionized plasma can be due to the collisional excitation of electronic states in ions, followed by the spontaneous emission of photons which carry away a portion of the kinetic energy. Radiative recombination processes, where a free electron recombines with an ion producing a photon, also lead to cooling in the gas. At temperatures above $10^7\,\mathrm{K}$ (at solar metallicity[1]), Bremsstrahlung cooling becomes important. The free-free emission is produced by the deceleration of electrons in the Coulomb field of positive ions. The electron loses kinetic energy, which is converted into a photon able to escape the plasma. The cooling timescale of the hot plasma is of order $\sim 10^8\,\mathrm{yr}$, which is longer than the dynamical timescale for the evolution of a supernova remnant (SNR), therefore cooling in SNR is likely dominated by adiabatic cooling due to the expansion of the gas.

The warm ionized medium (WIM): The warm gas with temperatures of $\sim 8000\,\mathrm{K}$, and densities $\sim 0.2\,\mathrm{cm}^{-3}$ is ionized and heated by the UV radiation emitted by massive O and B type stars. It is associated with well-defined regions called H II regions, with sizes and shapes determined by the balance between photoionization and recombination. Another more extended and diffuse ionized component is also found outside of H II regions, in the *Reynolds layer* of our Galaxy. It is the main form of interstellar gas above $\sim 700\,\mathrm{pc}$ from the Galactic plane (Reynolds, 1991). It is possibly ionized by the photons escaping the cavities blown by associations of massive stars.

In H II regions, the temperature is set by the balance of photoionization heating and radiative cooling. When an electron is freed from an atom due to the absorption of a UV photon, it carries kinetic energy away equal to the difference between the photon energy and the ionization potential, which goes into heating the gas. The cooling in H II regions is dominated by the emission of photons originating from the decay of excited low-lying (a few eV) energy states as a result of collisions between electrons and metal-ions (oxygen in particular) with a contribution from free-free emission. Figure 1.1 shows an example for a heating function $\Gamma(T)$ (dashed line) and a cooling function $\Lambda(T)$ (solid line labelled cooling function) for an H II region as function of temperature. The other solid line represent the contribution to the cooling function from the main oxygen and nitrogen transitions considered. The dashed line shows the cooling due to free-free emission. The ionizing star was assumed to have an effective temperature of $\sim 3.5 \times 10^4\,\mathrm{K}$ and the density of the H II region was set at $100\,\mathrm{cm}^{-3}$. The heating function and the total cooling function intersect at a temperature of $\sim 8000\,\mathrm{K}$ which represents the equilibrium temperature T_i of the ionized region. The heating rate Γ depends on the effective temperature of the ionizing star and on the optical depth of the gas. For an increased optical depth or an

[1]The metallicity of an object is the proportion of metals it contains; where any chemical elements other than hydrogen and helium are referred to as metals.

increased stellar temperature, the increase in Γ leads to an increase in T_i. The equilibrium temperature is generally around $\sim 10^4$ K (Osterbrock & Ferland, 2006).

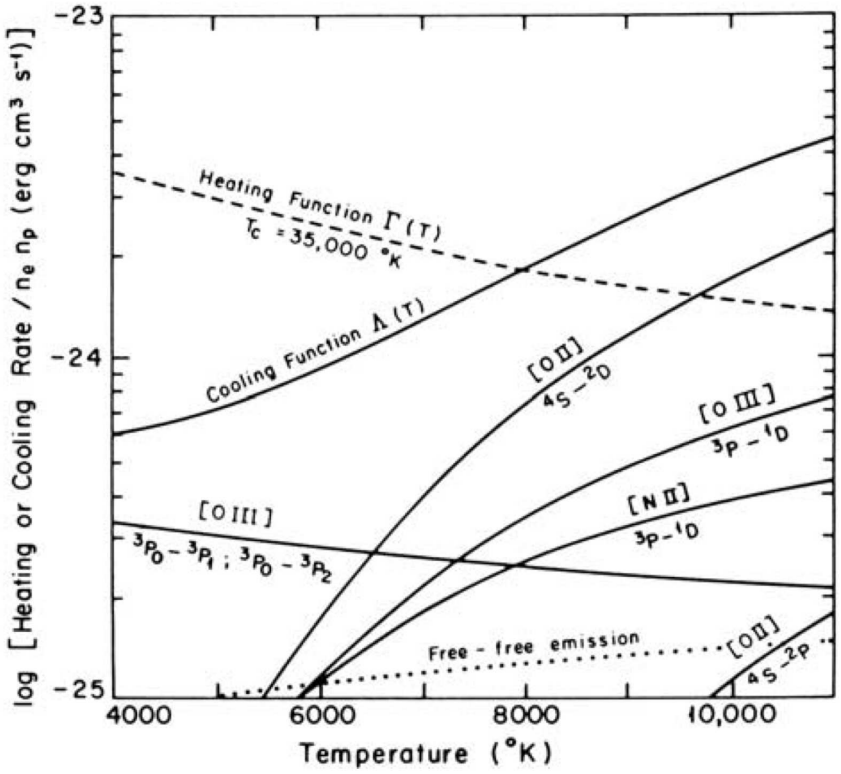

Figure 1.1: Example of a heating function $\Gamma(T)$ (dashed line) and a cooling function $\Lambda(T)$ (solid line labelled cooling function) for an H II region as function of temperature. The other solid line represent the contribution to the cooling function from the main oxygen and nitrogen transitions considered. The dashed line shows the cooling due to free-free emission. The ionizing star was assumed to have an effective temperature of $\sim 3.5 \times 10^4$ K and the density of the H II region was set at $100\,\mathrm{cm}^{-3}$. Image from Lequeux (2005) (itself from (Spitzer, 1978)).

The ionized gas can be observed in radio continuum radiation originating from the free-free emission from accelerating electrons, and in emission lines due to radiative recombination of ions with free electrons (e.g. Hα, O II, O III at optical wavelengths, Brγ in the near infrared).

The Atomic Phase: The neutral atomic phase consists primarily of H I gas. Two components with similar thermal pressure but different temperatures and densities are observed (Wolfire et al., 1995):

The Warm Neutral Medium (WNM): This phase occupies $\sim 30\%$ of the volume of the ISM, and is located mainly in photodissociation regions (PDR) on the boundaries

of H II regions and molecular clouds. It has characteristic temperatures of $\sim 8000\,\mathrm{K}$ and densities of $\sim 0.5\,\mathrm{cm}^{-3}$. It is traced by the 21-cm H I emission line.

The Cold Neutral Medium (CNM): The cold neutral gas is distributed in sheets and filaments occupying $\sim$ 1 - 4% of the ISM with temperatures of $\sim$ 80 - 100 K and densities of $\sim 50\,\mathrm{cm}^{-3}$. The main tracers are UV and optical H I absorption lines seen towards bright stars or quasars.

The main heating mechanism in the atomic phase is the photoelectric effect on small dust grains. The ultraviolet photons emitted by hot, massive stars can eject electrons from dust grains and large molecules. When a photon with energy larger than the work function of the grain material gets absorbed, an electron can be expelled from the grain's surface The excess energy of the photon heats up the grain and gives the ejected electron kinetic energy, thereby injecting thermal electrons which can heat the gas. Small grains and large molecules like Polycyclic Aromatic Hydrocarbons (PAHs) dominate this method of heating. Cooling in the atomic phase is mainly due to the de-excitation of collisionally excited fine-structure lines in metals, like the C II 158 μm line. It is particularly effective in the denser CNM phase. Lyman α cooling becomes a relevant mechanism at the higher temperatures observed in the WNM. Collisions can excite the $n = 2$ level of hydrogen which, upon de-excitation, releases a Lyα photon. Figure 1.2 shows the cooling rate as a function of temperature. The sharp increase at $\sim 10^4\,\mathrm{K}$ corresponds to cooling by the Lyα-line of hydrogen. For $T > 10^4\,\mathrm{K}$, the cooling is due to the excitation of various lines and to free-free radiation.

The presence of two gas phases in near pressure equilibrium at the densities and temperatures observed for the CNM and the WNM has been predicted by Field et al. (1969) in their static two phase equilibrium model of the ISM. Considering the balance of the heating and cooling rate equilibrium curve for optically-thin atomic gas, they found that for a pressure corresponding the mean pressure of the ISM ($n \times T \approx 10^3\,\mathrm{K\,cm}^{-3}$) there are three possible equilibria. These are the warm phase, at temperature $\sim 10^4\,\mathrm{K}$, the intermediate-temperature phase ($\sim$ 100 – 5000 K), and a cold phase (T $\sim$ 10 K). The warm and cold phases are thermally-stable, while for the intermediate-temperature phase small perturbations about the equilibrium result in increasing heating or cooling until a stable equilibrium point is reached. This picture has been revised. In a turbulent ISM the separation between the two phases is less pronounced. Numerical simulations (e.g Audit & Hennebelle, 2005; Ntormousi et al., 2011) and observations of the 21-cm emission and absorption (e.g Heiles & Troland, 2003) indicate the presence of out-of-equilibrium gas.

The Molecular Phase: These are molecular H_2 clouds at temperatures of $\sim$ 10 - 20 K and number densities $> 10^2\,\mathrm{cm}^{-3}$. Molecular clouds comprise $\sim$ 30% of the mass of the ISM, but occupy only $\sim$ 0.05% of its volume. The main tracers are mm-wavelength molecular emission lines. The primary tracer used is CO. Direct observations of H_2 molecules are difficult. As a homonuclear diatomic molecule, it does not possess a permanent electric dipole moment.

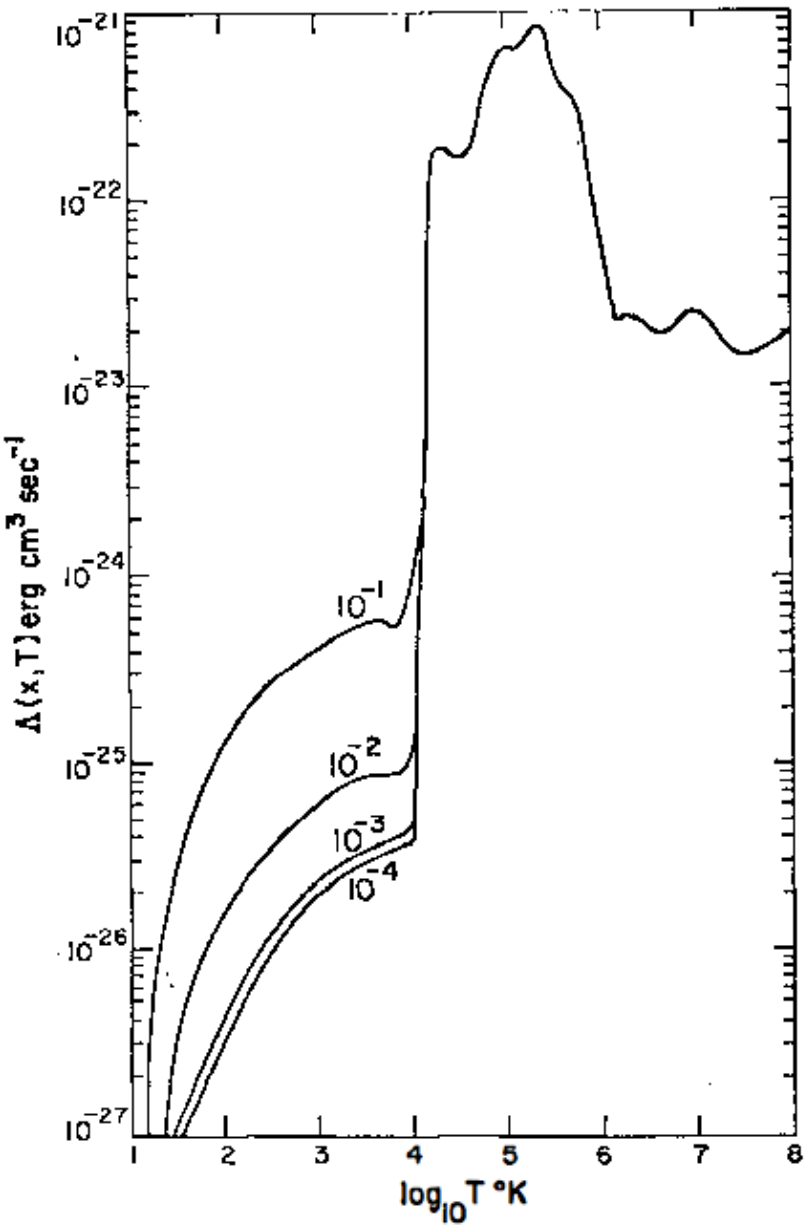

Figure 1.2: Cooling rate $\Lambda(T)/n_H^2$ for the interstellar gas as a function of temperature for different values of the ionization fraction n_e/n_H (n_e being the electron density and n_H being the hydrogen density). At $\sim 10^4$ K cooling by the Lyα -line sets in. For $T > 10^4$ K, the cooling is due to the excitation of various lines and to free-free radiation. From Dalgarno & McCray (1972).

The temperatures are mostly set by radiative processes. Low-energy cosmic rays are an efficient heating agent in molecular clouds. They can reach the innermost regions of the cloud and transfer energy to the gas through molecule dissociation, excitation and

ionization. The two main cooling processes in molecular clouds are molecular line emission and dust radiation. In particular, the excitation of rotational lines of CO by inelastic collisions with H_2 molecules is important. The excited molecule eventually returns to a lower energy state, emitting a photon which can escape the region. The cloud thus cools. Cooling by dust radiation is more effective at higher number densities $\sim 10^4\,\mathrm{cm}^{-3}$ where collisions between dust grains and molecules are frequent. The dust radiates away some of the energy by emitting mostly in the infrared (IR). This cooling mechanism is particularly relevant in very high density regions and collapsing cores.

1.1.2 Dust

Interstellar dust plays a fundamental role in the physical and chemical processes in the ISM although it only accounts for up to 1% in mass of the total interstellar matter. It mainly consists of carbonaceous particles and silicates. The origin of interstellar dust is not entirely understood. A fraction of the grains form by condensation in the outflows of late-stage stars (Matsuura et al., 2004), in stellar winds (Ferrarotti & Gail, 2002), and in the rapidly expanding gas shells of nova and supernova explosions (Starrfield et al., 1997; Pontefract & Rawlings, 2004). Shock waves in the ISM tend to rapidly destroy dust grains (Seab & Shull, 1983; Jones et al., 1997). This indicates that an appreciable amount of dust must be regrown in the ISM (Draine & Salpeter, 1979; Dwek & Scalo, 1980; Jones et al., 1994; Draine, 2009).

Dust particles absorb and scatter light. Indeed, the existence of interstellar dust was first deduced by Trumpler (1930) who noted that the light from the stars was dimmed by some interstellar material while propagating through space. This extinction process is more effective at shorter wavelengths so that red light is less affected than blue light. This effect is therefore also referred to as *reddening*. Comparing the extinction towards individual stars of the same spectral type allows one to constrain the nature and size of the obscuring dust grains, since wavelengths close to the obscuring grain size are most strongly affected. The wavelength-dependence of interstellar extinction, represented by extinction curves, allows one to derive a grain size distribution. Dust grains are estimated to have radii between 0.005 and $1\,\mu$m. Models of the extinction curve of the ISM suggest that the size distribution of the grains follows a power law with index -3.5 (Mathis et al., 1977).

Spectral features in the extinction curves also reveal the chemical composition. They are interpreted as signatures of specific radiative transitions. For example, a prominent bump in the UV at a wavelength $\sim 2175\,\text{Å}$, is attributed to graphite particles, the IR bands at $9.7\,\mu$m and $18\,\mu$m are attributed to amorphous silicates and a set of five mid-IR emission lines between 3.3 and $11.3\,\mu$m are indicators of polycyclic aromatic hydrocarbons (PAHs).

Dust is a dominant heating source by providing photoelectrons in the diffuse ISM (see the paragraph about the atomic gas phase in section 1.1.1) and an important cooling agent in dense regions by radiating in the infrared due to collisions between gas and dust grains. The infrared emission from dust provides an additional tool to study the properties of interstellar dust. It is best observed with space telescopes, since absorption and emission

processes in the Earth's atmosphere are important at longer wavelengths.

Dust plays an essential role in the formation of molecules. The grains serve as catalysts by allowing atoms to recombine on their surface. They also shield the resulting molecules from photodissociation by the ambient UV radiation field. H_2 formation in particular is very efficient on grain surfaces (Cazaux & Tielens, 2004).

1.1.3 Cosmic Rays

Cosmic rays are primarily high-energy protons and atomic nuclei with small fractions of electrons, positrons and antiprotons. They have velocities close to the speed of light but span several orders of magnitude in kinetic energies. Most of the low energy cosmic rays with energies $\leq 0.1\,\mathrm{GeV}$ measured on Earth originate from the Sun. Those below $\sim 10^9\,\mathrm{GeV}$ in energy are called Galactic cosmic rays. Above that energy, they are referred to as extragalactic cosmic rays (Butt, 2009).

The origin of the more energetic cosmic rays is still under debate. Supernova remnants (SNRs) are thought to be the most plausible source of Galactic cosmic rays (Ackermann et al., 2013; Blasi, 2013). The charged particles entering the supernova shock front can be accelerated to high energies during the lifetime of SNR by diffusing back and forth due to magnetic fluctuations of the plasma flow on both sides of the shock (Tatischeff, 2008). Cosmic rays play a key role in the pressure support of the ISM. They ionize and heat the gas even in denser neutral and molecular regions shielded from the UV radiation. The small ionizing effect they provide inside molecular clouds plays an important role in the coupling of the gas to the magnetic field.

1.1.4 Magnetic Fields

The observed polarization of the light emitted by the stars has uncovered the presence of magnetic fields in our Galaxy. Non-spherical, spinning dust grains align with their longer axes perpendicular to the local magnetic field, thereby preferentially blocking light perpendicular to the magnetic field. Hence, polarization measurements of starlight provide information on the direction of the magnetic field. The strength of the magnetic field can be determined from observations of the Zeeman splitting of the H I 21 cm in radio lines. The Faraday rotation of linearly polarized radio signals, and the radio synchrotron emission from relativistic electrons provide additional ways to determine the field strength.

Typical values of a few μG have been found in regions with gas number densities $n \approx 1$ - $100\,\mathrm{cm}^{-3}$ with a tendency to increase with increasing n. In the higher density range $n \approx 10^2$ - $10^4\,\mathrm{cm}^{-3}$, the magnetic field strength can reach up to a few tens of μG.

Magnetic fields can affect the dynamics of the gas in the ISM, since there is a sufficient degree of ionization in all phases for magnetic fields to be coupled to the gas (Elmegreen, 1981). Magnetic torques allow for the transport of angular momentum from a rotating cloud to its environment (Mouschovias & Paleologou, 1979). This mechanism plays a role during the collapse of protostellar cores as it helps to redistribute angular momentum (Hennebelle et al., 2011).

Magnetic fields can also be a source of additional pressure, able to counteract the selfgravity of the gas (Shu et al., 1987). Although observations indicate that they are not always strong enough to provide sufficient support (Bourke et al., 2001; Crutcher et al., 2009; Crutcher et al., 2010). But even weak magnetic fields affect the fragmentation process in cores (Price & Bate, 2007; Hennebelle & Teyssier, 2008; Peters et al., 2011). They affect the outflows from stars and the coupling between outflow driven processes and the circumstellar environment (Krumholz et al., 2007; Nakamura & Li, 2007).

1.1.5 The Role of the Stars

As already indicated in the previous sections, stars play an important role in the dynamical, thermal and chemical evolution of the ISM. In particular, the most luminous and most massive O and B stars play a key role although they represent only a small fraction of the stellar population. They are responsible for the hot and the warm phases in the ISM. Their stellar radiation photons are able to dissociate molecules at the surface of molecular clouds and to ionize and heat up the surrounding neutral regions. Stars return matter to the ISM and inject momentum and energy into the ISM through jets, stellar winds and supernova explosions, thereby producing hot gas that expands and rises above the Galactic disc.

Stellar feedback also affects the colder phases in the ISM. Its impact can be twofold. On the one hand, the radiation fields, the winds and the supernova explosions of OB-stars, disrupt and expel the gas from the natal molecular clouds. This can delay and even bring the star formation to a halt. On the other hand, the different feedback mechanisms drive shocks into the surrounding medium and generate bubbles that can sweep up and compress the gas. The dense shells can then cool and fragment into cold clumps and cores. The shocks can trigger the collapse of dense cores possibly leading to new localized star formation.

Beside their important contribution to the gas phases, stars and their feedback also play a fundamental role for the other constituents in the ISM. Stellar winds and supernovae are notable suppliers of dust, cosmic-rays are accelerated in supernova remnants and magnetic fields can be amplified by the turbulent motions generated by supernova explosions.

1.2 Properties of Molecular Clouds

Star formation is mainly associated with the dense and cold molecular phase of the ISM which takes the form of coherent highly substructured clouds. They can be observed in radio and infrared molecular emission and absorption lines, and cover a wide range of scales, with sizes of a few to several tens of parsecs. They contain about 50% of the total interstellar gas of the Galaxy but occupy only 1% of the volume. They are cold concentrations of dust and gas which are sufficiently dense to shield their contents against

The information contained in Section 1.2 is based on Ward-Thompson & Whitworth (2011) and reviews by McKee & Ostriker (2007); Klessen (2011) and Dobbs et al. (2013). Original references to the information cited here can be found therein.

the destructive ambient ultraviolet (UV) radiation field, allowing for the formation and survival of molecules. They are dense and massive enough to be self-gravitating, meaning that they are held together by the gravitational attraction of their constituent parts. They exhibit complex, often filamentary like structures. In their capacity as "stellar nurseries", their properties are both affected and affecting in the interwoven mechanisms regulating the star formation process.

Molecular clouds span a wide range of sizes and masses. The common parameters are their relatively high average number densities $> 10^2\,\mathrm{cm}^{-3}$ and their low temperatures $< 100\,\mathrm{K}$. Under these conditions and in the presence of dust, molecular hydrogen (H_2) and other molecules can be formed.

	Molecular Cloud	Cluster-forming Clumps	Protostellar Cores
Size (pc)	2 - 20	0.1 - 2	≤ 0.1
Mean density ($H_2\,\mathrm{cm}^{-3}$)	10^2 - 10^3	10^3 - 10^5	$> 10^5$
Mass ($M_\odot$)	10^2 - 10^6	10 - 10^3	0.1 - 10
Temperature (K)	10 - 30	10 - 20	7 - 12
Line width ($\mathrm{km\,s}^{-1}$)	1 - 10	0.5 - 3	0.2 - 0.5
RMS Mach number	5 - 50	2 - 15	0 - 2
Column density ($\mathrm{g\ cm}^{-2}$)	0.03	0.03 - 1.0	0.3 - 3
Crossing time (Myr)	2 - 10	≤ 1	0.1 - 0.5
Free-fall time (Myr)	0.3 - 3	0.1 - 1	≤ 0.1

Table 1.2: Excerpt from Klessen (2011): Physical properties of molecular cloud and cores ed from Cernicharo (1991) and Bergin & Tafalla (2007)

1.2.1 The Larson Relations

Observations of molecular clouds have uncovered their highly structured and filamentary nature. Although the mean densities are about $\sim 100\,\mathrm{cm}^{-3}$, molecular clouds are inhomogeneous and exhibit much higher-density in small scale structures called clumps and cores. Table 1.2 summarizes the properties of molecular structures of different sizes.

At the scales of giant molecular clouds (GMCs), the internal motions appear chaotic. However, molecular clouds seem to follow very general empirical scaling relations although the degree of universality and the interpretation of these relations is still being debated. These scaling relations appear to hold over a wide range of molecular structures, masses and environments. They were first established by Larson (1981) who included whole cloud complexes, individual clouds, and density enhancements or clumps within clouds. Larson (1981) and subsequent surveys of molecular clouds in the Galaxy (Solomon et al., 1987; Heyer & Brunt, 2004) have revealed that the internal velocity dispersion σ, which is a measure of the width of the velocity distribution, systematically increases with cloud radius R,

$$\sigma \propto R^{1/2} \qquad \text{(Larson's first law)}. \tag{1.1}$$

Figure 1.3 illustrates this relation. Similarly, the velocity dispersion also scales with the

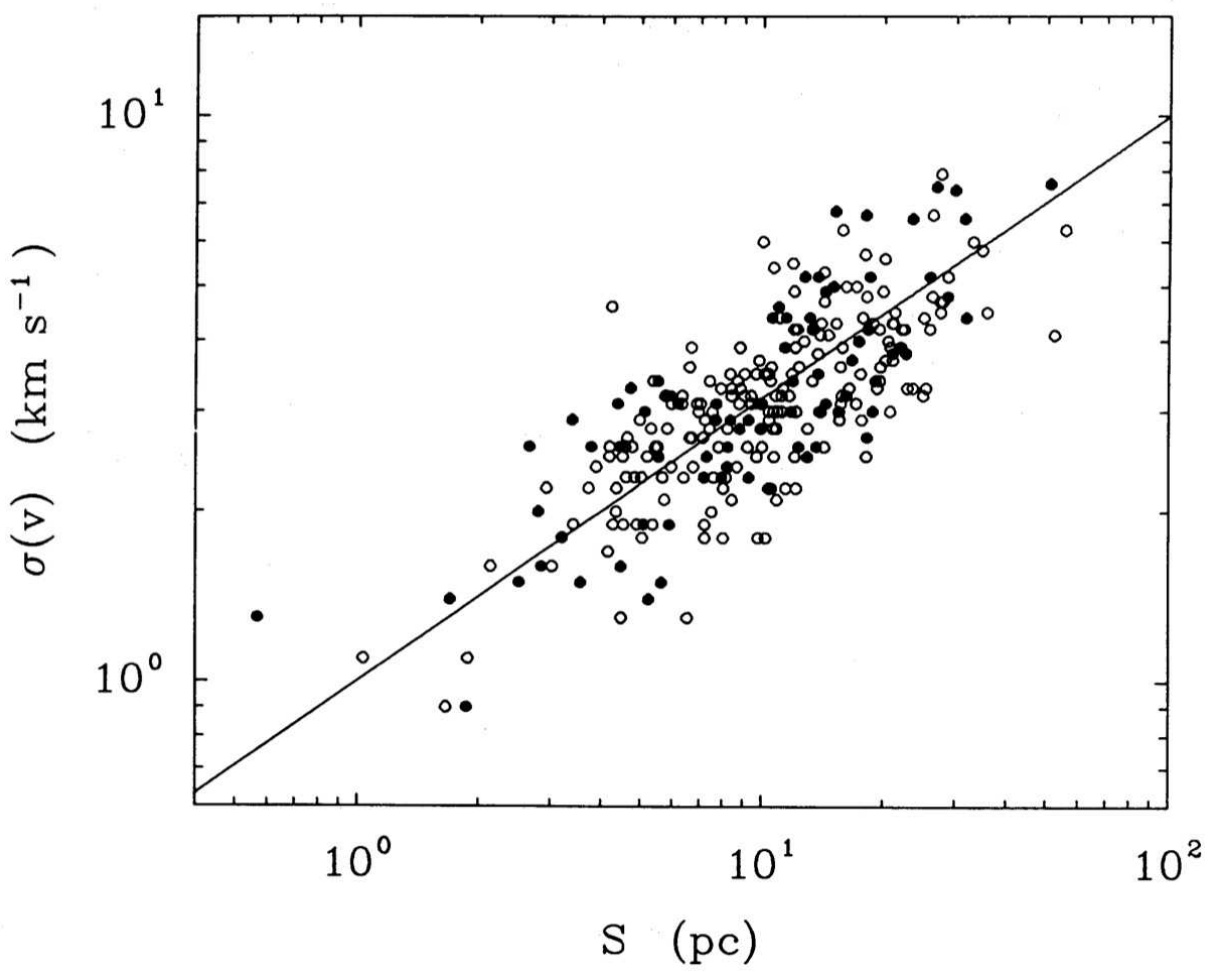

Figure 1.3: Velocity dispersion $\sigma(v)$ as a function of size S for a sample of 273 molecular clouds from the Galaxy. Image from Solomon et al. (1987).

cloud mass M according to

$$\sigma \propto M^{1/4}. \tag{1.2}$$

From equations 1.1 and 1.2 we obtain

$$\sigma^2 \propto \frac{M}{R}. \tag{1.3}$$

Introducing the density $\rho \propto M/R^3$, we can derive

$$\sigma \propto \rho^{1/2} R \qquad \text{(Larson's second law)}. \tag{1.4}$$

Which can be rewritten as

$$\frac{M}{R\sigma^2} = constant. \tag{1.5}$$

Therefore

$$\frac{M}{R^2} = constant, \tag{1.6}$$

and the density ρ is related to the radius of the molecular cloud, following

$$\rho \propto R^{-1} \qquad \text{(Larson's third law)}. \tag{1.7}$$

The apparently "universal" properties of molecular clouds have been interpreted as indications for fundamental physical processes like gravity or turbulence governing the state and evolution of molecular clouds.

1.2.2 The Virial Interpretation

The virial theorem relates the gravitational potential energy of a system to its kinetic or thermal energy

$$\Omega_G + 2K = 0, \tag{1.8}$$

where K is the total kinetic energy, due to both random thermal motions and to bulk flow of the clouds constituents. Ω_G is the self-gravitational potential energy of the cloud. For a stable, self-gravitating, spherical cloud of mass M, radius R and velocity dispersion σ

$$\Omega_G \approx -\frac{GM^2}{R}, \tag{1.9}$$

$$K = \frac{1}{2}M\sigma^2. \tag{1.10}$$

This leads to

$$\frac{M}{R\sigma^2} \approx \frac{1}{G}. \tag{1.11}$$

The equivalence of equations 1.11 and 1.5 can be interpreted as an indication for the virialized state of molecular clouds.

1.2.3 The Role of Turbulence

The existence of the linewidth-size relation (Larson's first law, equation 1.1) can also be interpreted as a result of a turbulent energy cascade, where energy is transported from large scales down to small scales until it is dissipated by heating the cloud.

In an incompressible fluid, the turbulent cascade produces a characteristic relation between the size-scale of a turbulent eddy L and the velocity dispersion σ of that eddy

$$\sigma \propto L^{1/3}. \tag{1.12}$$

This is known as the Kolmogorov-law.

Observed line-widths in molecular clouds are usually larger than the thermal velocity dispersion $\sigma_{th} = (kT/m)^{1/2}$, where k is the Boltzmann constant, m the mean molecular

weight of the observed gas and T is the gas temperature. This means that shocks where energy is dissipated must be present and the Kolmogorov theory does not apply anymore. However in the compressible, shock-dominated case (Burgers, 1974), the energy decay also leads to power-law scaling relations for the velocity correlations

$$\sigma \propto L^{1/2}. \tag{1.13}$$

This is referred to as Burgers turbulence or "Burgulence" (Frisch & Bec, 2000). Equation 1.1 exhibits the same power-law index as equation 1.13, prompting the interpretation of supersonic turbulence as the origin of Larson's laws (Kritsuk et al., 2013).

1.3 Star Formation

Stars form by the gravitational collapse of dense regions in the ISM. A region of cold gas will collapse when its gravitational self-attraction is greater than the hydrostatic pressure support of the gas. This gravitational instability is described by the Jeans length and Jeans mass. For gas of uniform density ρ, the Jeans length λ_J is the diameter of a region of the gas that is just large enough for the gravitational force to exceed the pressure support. It is given by

$$\lambda_J = c_s \sqrt{\frac{\pi}{G\rho}}. \tag{1.14}$$

where c_s is the speed of sound in the gas and G is the gravitational constant. The Jeans mass is the mass of a region that has a diameter equal to the Jeans length

$$M_J = \frac{4\pi}{3}\left(\frac{\lambda_J}{2}\right)^3 \rho = \frac{\pi}{6}\rho\lambda_J^3 \tag{1.15}$$

The characteristic timescale on which collapse occurs is given by the free-fall time t_{ff}. For a spherically symmetric distribution of mass with a total mass M and initial radius R it is given by

$$t_{ff} = \pi\sqrt{\frac{R^3}{8GM}} = \sqrt{\frac{3\pi}{32G\rho}}. \tag{1.16}$$

A molecular cloud with a mass $M > M_J$ becomes gravitationally unstable and contracts. The density in the cloud increases and therefore the Jeans mass decreases. This might cause parts of the cloud to become unstable and contract on their own, leading to the fragmentation of the cloud. Turbulence also plays a role in the fragmentation process. The density distribution resulting from turbulence, provides the denser "seed"-clumps, which if massive enough, can undergo gravitational collapse and subsequent fragmentation. This process is known as *gravoturbulent* fragmentation (Klessen, 2011).

The fragmentation process leads to a distribution of clumps and cores. The mass spectrum of clumps appears to follow a power law

$$\frac{dN}{dm} \propto m^{-\alpha}, \tag{1.17}$$

m being the clump mass and the exponent being in the range $1.3 < \alpha < 2.0$ (Stutzki & Guesten, 1990; Williams et al., 1994; Kramer et al., 1998; Pekruhl et al., 2013). The power law appears valid for clump masses between $\sim 1\,M_\odot$ and $\sim 10^3\,M_\odot$. For protostellar cores with masses ranging from $1\,M_\odot - 10\,M_\odot$ and sizes ≤ 0.1 pc, the exponent becomes $\alpha \approx -2.5$ (Motte et al., 1998). This core mass function (CMF) exhibits a turnover with a peak at $\sim 1\,M_\odot$ (André et al., 2010; Könyves et al., 2010). The CMF shape appears very similar to the shape of the observed stellar initial mass function (IMF) but is shifter towards higher masses by a factor of ~ 3. The IMF exhibits a power law index $\alpha \approx 2.35$ for the mass range above $\sim 1\,M_\odot$ (Salpeter, 1955). The low mass $< 1\,M_\odot$ can be fitted by a lognormal distribution (Chabrier, 2003; Chabrier, 2005).

The origin of a "universal" IMF is still being debated. The similarity between the CMF and the IMF has prompted thoughts of a possible link between the two distributions. Stellar masses could be resulting directly from the progenitor core masses which are set by gravoturbulent processes (Padoan & Nordlund, 2002; Hennebelle & Chabrier, 2008; Hennebelle & Chabrier, 2009). The shift by a factor of 3 could be the result of protostellar outflows that limit gas accretion onto a forming star (Matzner & McKee, 2000). This is known as the *core accretion* model. In contrast, the *competitive accretion* model assumes that all the gas fragments down to one Jeans Mass. The stellar masses are then determined by the interactions between protostars competing for the surrounding gas (Bonnell et al., 2001; Bate et al., 2003; Clark et al., 2007). The similarity between the IMF and the CMF would then only be a coincidence.

1.4 Massive Stars and their Winds

Nuclear fusion is the main source of energy during the lifetime of a star. In a stellar core, densities and temperatures are high enough to overcome the repulsive Coulomb forces between protons. Hydrogen is converted into helium through nuclear fusion. Stars spend most of their lifetime in this first evolution stage, which is known as the *main sequence*.

The stellar mass is the dominant parameter determining the post main-sequence evolution. Once the hydrogen in the core is consumed, the core of the star contracts, heats up and Hydrogen burning ignites in a shell around the helium core. As a result the star expands and cools at the surface. If the star is massive enough, the contraction of the core leads to temperatures high enough to start the nuclear fusion of helium producing a carbon (C) and oxygen (O) core. When the fusion process in the core is terminated, the core collapses while He-burning is ignited in a shell around the core. More massive stars are able to fuse and produce even heavier elements (up to iron). This leads to a sequence of concentric shells containing heavier elements towards the center at the end of a massive star's evolution (see figure 1.4).

The term *massive star* is generally used to designate stars with masses above $8\,M_\odot$.

The information contained in Section 1.4 is based on Lamers & Cassinelli (1999) and the reviews by Kudritzki & Puls (2000), Woosley et al. (2002) and Langer (2012). Original references to the information cited here can be found therein.

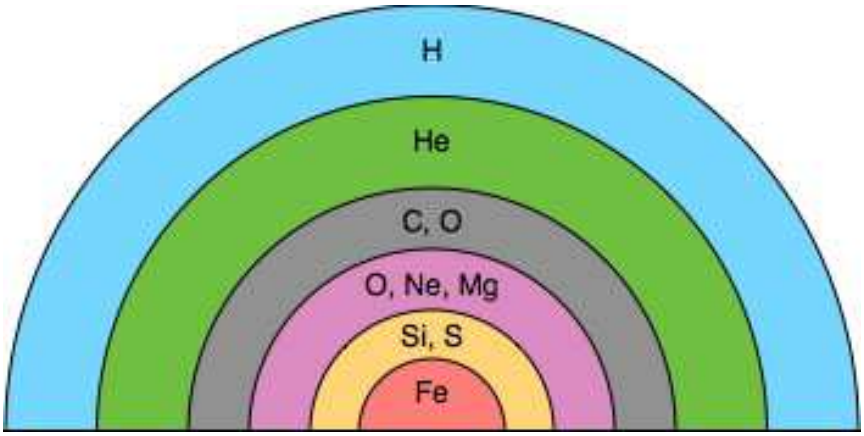

Figure 1.4: Sketch of the onion like structure of a massive star at the end of its evolution.

They are massive enough to undergo non-degenerate carbon ignition in their cores. During the main-sequence phase, the dominant source of energy for stars more massive then $\sim 2\,M_\odot$ is a chain of reactions referred to as the CNO-cycle. It involves catalyst species such as carbon, nitrogen, and oxygen which allow four protons to be merged into one helium nucleus.

The analysis of stellar spectra allows to determine the temperature at the surface of the star. The standard spectral class classification is thus based on temperature. The spectral classes O, B, A, F, G, K, M go from hot to cool with O being the hottest. Each letter is again subdivided, the subdivisions being numbered from 0 to 9, in order of decreasing temperature.

Massive stars are very luminous and hence very hot. In their outer atmospheres, radiation and gas pressure forces can counteract and overcome gravity, leading to outflows of gas referred to as winds. During the main-sequence phase, the winds of hot and luminous OB-type stars are driven by line interactions. The gas in the atmosphere of massive stars mostly consists of free electrons, ionized hydrogen and helium, and multiply-ionized species of more complex atoms.

Photons from the photosphere with energies corresponding to transitions between electronic energy levels in the ions excite the bound electrons to higher energy levels. When the electrons fall back to their original energy level, new photons are emitted. In this way, energy and momentum are exchanged between the radiation field and the absorbing gas. In a static outer atmosphere or in a medium with constant velocity, the number of photons with energies corresponding to an atomic transition is limited. These photons would be absorbed in the lower layers of the atmosphere and the outer layers would be significantly less affected. In an accelerated atmosphere however, the radiation from the photosphere would appear redshifted towards the atoms in the atmosphere. As a result, outer layers are able to absorb photons with the right Doppler-shifted frequency. This leads to further acceleration of the atmosphere and thereby drives the outflow of material from the surface of the star. So called *line driven winds* are launched.

The main parameters characterizing the winds from massive stars are the mass-loss rate $\dot{M}$ and the terminal velocity v_∞. They can be derived from observed spectral lines. [2]Two types of lines can be used. So called *P Cygni* profiles in metal species such as carbon, nitrogen, oxygen result from the spontaneous reemission or scattering after the absorption of the photons. They are a type of spectroscopic feature where the presence of both absorption and emission at different Doppler shifts in the line profile indicate expanding material or outflow. Another type of line used for stellar wind diagnostics are recombination or emission lines of hydrogen or helium in the optical and near-infrared. In particular Hα is used as an indicator of mass-loss rates since it traces gas outflow in the vicinity of the star.

The post main-sequence evolution of massive stars is complex and may involve many phases such as the red supergiant, the blue supergiant, and the Wolf-Rayet phase. The evolutionary path followed by the star, depends on many factors: e.g. its metal content, its mass, its rotational velocity, whether it is magnetic or not, and whether it is a single star or part of a multiple system (Langer, 2012).

1.5 The ISM and Feedback of Massive Stars

Observations show that stars form in a clustered environment (Lada & Lada, 2003; Portegies Zwart et al., 2010). In clusters containing less than ~ 100 OB-type stars, the maximum stellar mass appears to scale with the mass of the cluster (Weidner & Kroupa, 2006; Oey & Clarke, 2005). Although the most massive stars are also the shortest-lived, they have the ability to profoundly impact the evolution of the surrounding cluster environment even before they explode in a supernova.

The powerful winds they produce (see section 1.4) can reach velocities of the order $10^3\,\mathrm{km\,s^{-1}}$. These are highly supersonic velocities with respect to the ionized gas at temperatures of $10^4\,\mathrm{K}$ where the sound speed is of order $10\,\mathrm{km\,s^{-1}}$. They can create shocks and blow bubbles filled with hot plasma into the gas. Massive stars also emit strong UV-radiation in the form of Lyman continuum photons which can very efficiently ionize and heat atomic and molecular gas to create H II-regions (see section 3.2 for an overview on the evolution of H II regions) and photodissociation regions (PDRs) at the interface between the ionized gas and the cold molecular phase. Besides stellar winds and ionizing radiation, the radiation pressure, which is basically the injection of momentum into the gas due to the absorption of photons, also plays a role. The latter effect is however not considered in this thesis. After a few $\sim 1-3\,\mathrm{Myr}$ the most massive stars explode as supernovae of Type II (SN II), creating supernova remnants (SNRs) that sweep up the remaining ambient medium. The feedback bubbles of neighboring stars can overlap and create superbubbles with sizes of several kpc.

Theoretical studies have examined the impact of massive star feedback on idealized smoothed surrounding media and derived analytical descriptions for the evolution and

[2]Detailed description of the observational methods used to derive properties of stellar winds can found in e.g. Kudritzki & Puls (2000) and Lamers & Cassinelli (1999)

structures of spherical HII regions and stellar wind bubbles. The pioneering work of Strömgren (1939) introduced the concept of the Strömgren sphere, allowing one to derive the time evolution of an ionization front (Spitzer, 1978). The effects of stellar winds have been studied in detail analytically (see e.g. Weaver et al., 1977; Lamers & Cassinelli, 1999; Capriotti & Kozminski, 2001, for details of the models). Ostriker & McKee (1988) presented a general and very thorough study of spherical blastwaves. These theoretical descriptions are at the core of our understanding of the evolution of HII regions, wind bubbles and supernova remnants.

Observations and numerical simulations have shown that the above feedback mechanisms can produce a variety of structures, including superbubbles at large scales (Oey & García-Segura, 2004; Ntormousi et al., 2011), cavities (Fierlinger et al., 2012), shells (Deharveng et al., 2010; Walch et al., 2012), pillars and filaments (Gritschneder et al., 2010; Preibisch et al., 2011a; Walch et al., 2012). Some stars with velocities $\geq 30\,\mathrm{km\,s^{-1}}$, so called *runaway stars*, can even produce bow-shocks while rushing through their ambient medium (Kobulnicky et al., 2012; Gvaramadze et al., 2012; Mohamed et al., 2012; Mackey et al., 2013; Ngoumou et al., 2013).

The impact of the above feedback mechanisms on the star formation process is twofold. On one side, they disperse and destroy the neutral gaseous environment, thereby delaying or even stopping further star formation (negative feedback). On the other side, they lead to cold regions of enhanced densities in the strong shocks which can compress clouds while sweeping through the ambient gas medium. This, in return can lead to more stars forming (positive feedback). Although the overall picture is well-established, the details of the feedback-ISM interactions and the relative importance of the various feedback mechanisms are not entirely understood. The Carina Nebula, presented in the next section, might serve as a perfect example of the complex interplay between the massive stars and their cluster environment.

1.6 The Carina Nebula: Massive Stars in Action

The Carina Nebula (NGC 3372) is located in the Sagittarius-Carina Spiral arm of the Galaxy at a distance of 2.3 kpc. It hosts an important population of massive stars including 65 O-type stars, 3 Wolf-Rayet stars and the Luminous Blue Variable η Carina (Smith & Brooks, 2008). The center of the Carina Nebula contains the two open clusters Trumpler 14 (Tr 14) and Trumpler 16 (Tr 16), which is the home of the Luminous Blue Variable η Carina (η Car). Tr 14 is one of the youngest known star clusters in Carina with $< 1\,\mathrm{Myr}$ (Sana et al., 2010) while Tr 16 has an age of $\sim 3\,\mathrm{Myr}$ (Wolk et al., 2011). Another open cluster, Trumpler 15 (Tr 15), located North of Tr 14 and Tr 16, exhibits an age $\sim 5 - 10\,\mathrm{Myr}$ (Wang et al., 2011). The Carina Nebula is a region of active star formation, which is profoundly influenced by the UV-radiation and the winds from massive stars. Multi-wavelength observations reveal the young stellar population, the complex structures of the gas and the interplay with the stellar feedback in the Carina Nebula.

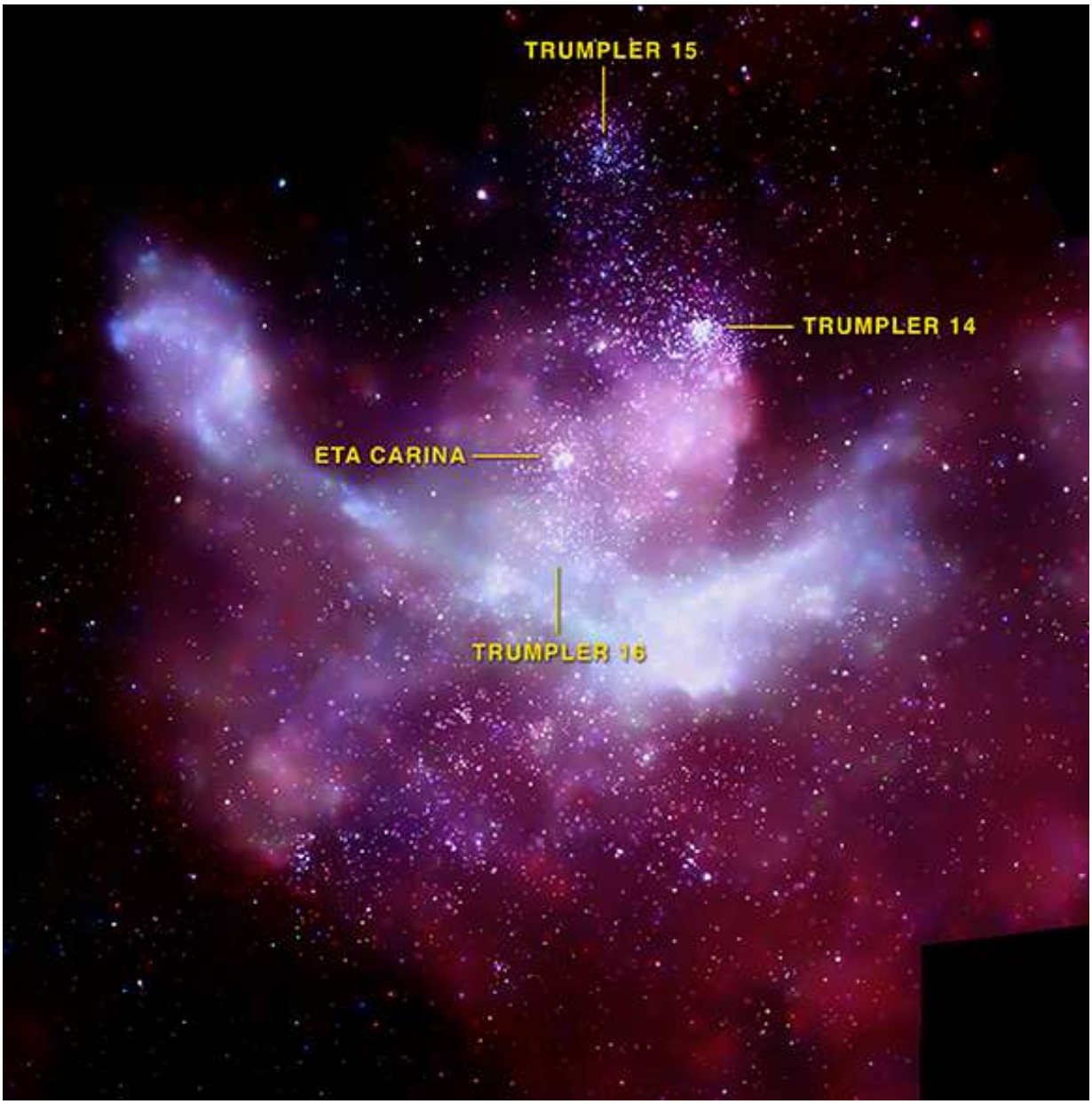

Figure 1.5: Image of the Carina Nebula Chandra image shows the 14000+ stars and the soft extended X-ray emission. Color Code: X-ray 0.5-0.7 keV (Red), 0.7-0.86 (Green), 0.86-0.96 (Blue). The location of η Car and the star clusters Tr 16, Tr 15 and Tr 14 are labelled. Image credit: NASA/CXC/PSU/L.Townsley et al.

1.6.1 Multi-Wavelength Observations

X-rays: The large scale X-ray survey of the Carina Nebula performed with the *Chandra* X-ray satellite in the framework of the *Chandra* Carina Complex Project (CCCP Townsley et al., 2011a), helped unveil the vast numbers of young stellar objects in the Ca-

rina Nebula. It produced a catalog a point-sources of which most are believed to be young stars (Broos et al., 2011). Townsley et al. (2011b); Townsley et al. (2011c) also reported on the observed diffuse soft X-ray component in Carina which traces the hot plasma filling the bubble, possibly produced by the winds from the massive stars and/or one or more supernova explosions in the region. The diffuse emission observed by *Chandra* seems to support the idea that supernovae have already occurred in Carina.

Figure 1.6: Dust pillars in the Carina Nebula. The image from the *Hubble* Space Telescope (HST) shows the narrow jets of gas ejected by young stars embedded in the tips of the pillars. Color code: 502 nm-line (Blue), 657 nm-line (Green), 673 nm-line (Red). Image credits: NASA, ESA, and M. Livio and the Hubble 20th Anniversary Team (STScI).

Optical: At optical wavelengths, Hα observations with the Advanced Camera for Surveys (ACS) on the *Hubble* Space Telescope (HST) uncovered protostellar outflows and jets, which indicate a large population of accreting young protostars and Young Stellar Objects (YSOs) in the region (Smith et al., 2010a). Figure 1.6 shows the dusty pillars located North of η Car and two Herbig Haro objects (HH 901/902), which are narrow jets of gas ejected by newly born stars. The YSOs appear embedded in the heads of the pillars.

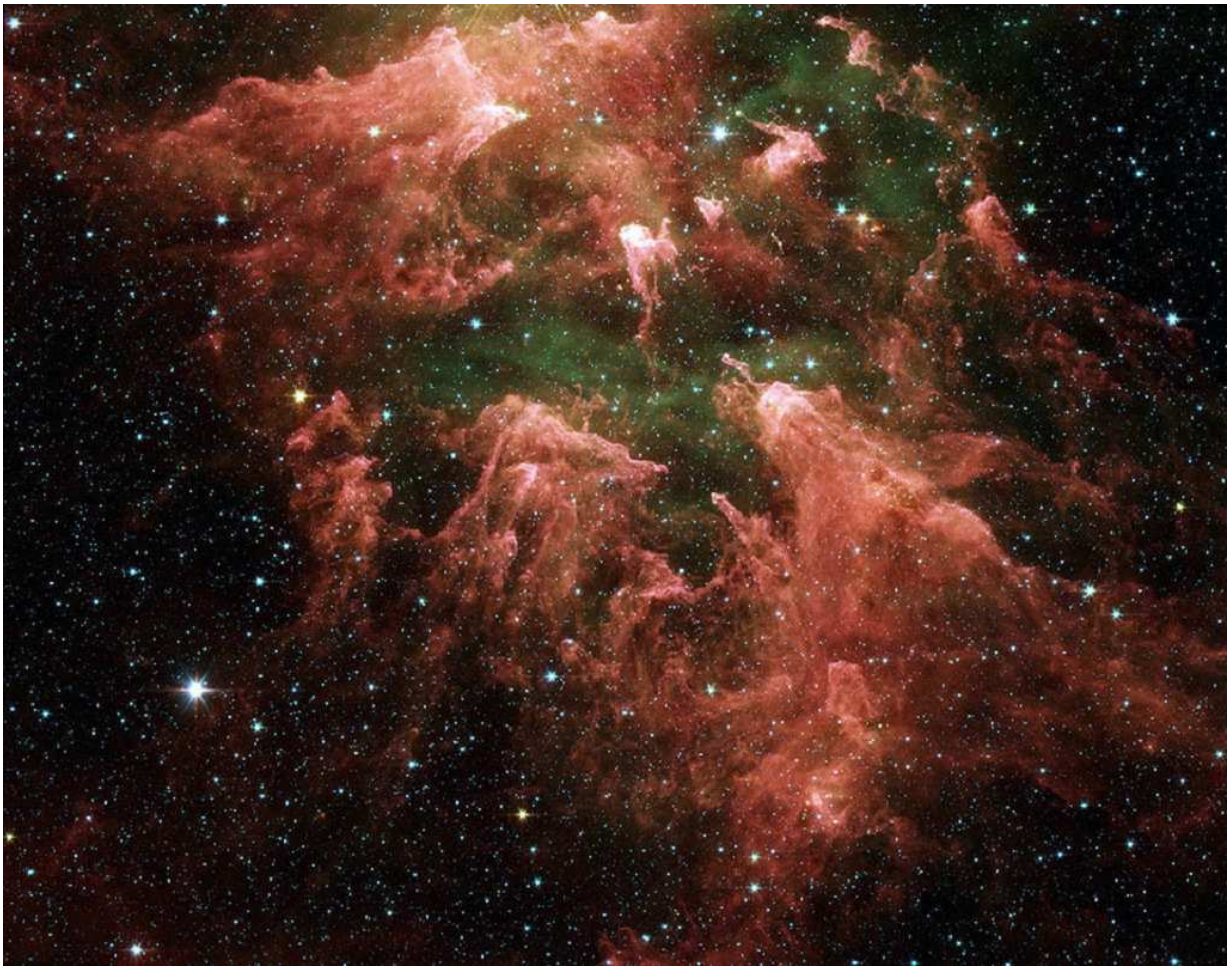

Figure 1.7: Image of the South Pillars in the Carina Nebula from the *Spitzer Space Telescope* using the using the Infrared Array Camera (IRAC). Color Code: 3.6 μm (Blue), 4.5 μm (Green), 5.8 μm (Orange), and 8.0 μm (Red). Image credit: NASA, SSC, JPL, Caltech, Nathan Smith (Univ. of Colorado), et al.

Near and Mid-Infrared: *Spitzer* observations in the mid-infrared show warm gas and dust on the surface of the many pillars, clouds and clumps seen in the region (Smith et al., 2010b). Figure 1.7 shows the giant pillars located South-East of η Car. They are believed to be shaped and eroded by the feedback from the massive stars, as almost all of them

Figure 1.8: Image of the Carina Nebula, taken using the HAWK-I camera on ESO's Very Large Telescope. RGB image, color code: J band 1.25 μm (Blue), H band 1.65 μm (Green), K_s band 2.2 μm (Red). Image credit: ESO/T. Preibisch.

are oriented towards the central region containing η Car and the Tr 16 cluster. These structures often harbor young stellar objects as found in a near-infrared survey with the HAWK-I wide-field imager on the Very Large Telescope (VLT) by Preibisch et al. (2011b). Figure 1.8 shows the numerous stars in Carina including the very bright η Car on the lower left of the image. It also shows some diffuse irradiated gas structures and the more dense and opaque dark clumps.

Far-Infrared: The *Herschel* view of the Carina Nebula is very impressively displayed in figure 1.9. It traces the warm ($\sim 15 - 40$ K) and diffuse gas found in cavities and on the surface of irradiated structures, revealing the small-scale structure of the dense clouds (Preibisch et al., 2012; Roccatagliata et al., 2013). It beautifully illustrates the impact of the feedback from the massive stars on their natal cloud and the range of morphologies and structures like pillars, filaments, clumps, cavities and bubbles they create. The *Herschel* maps (figure 1.9) uncovered the embedded protostars whose location seem to coincide with the irradiated edges of clouds and pillars (Gaczkowski et al., 2013).

Figure 1.9: *Herschel* view of the Carina Nebula. Color code: 70 μm (Blue), 160 μm (Green), 250 μm (Red). Image credits: ESA/PACS/SPIRE/Thomas Preibisch, Universitäts-Sternwarte München and the Ludwig-Maximilians-Universität München.

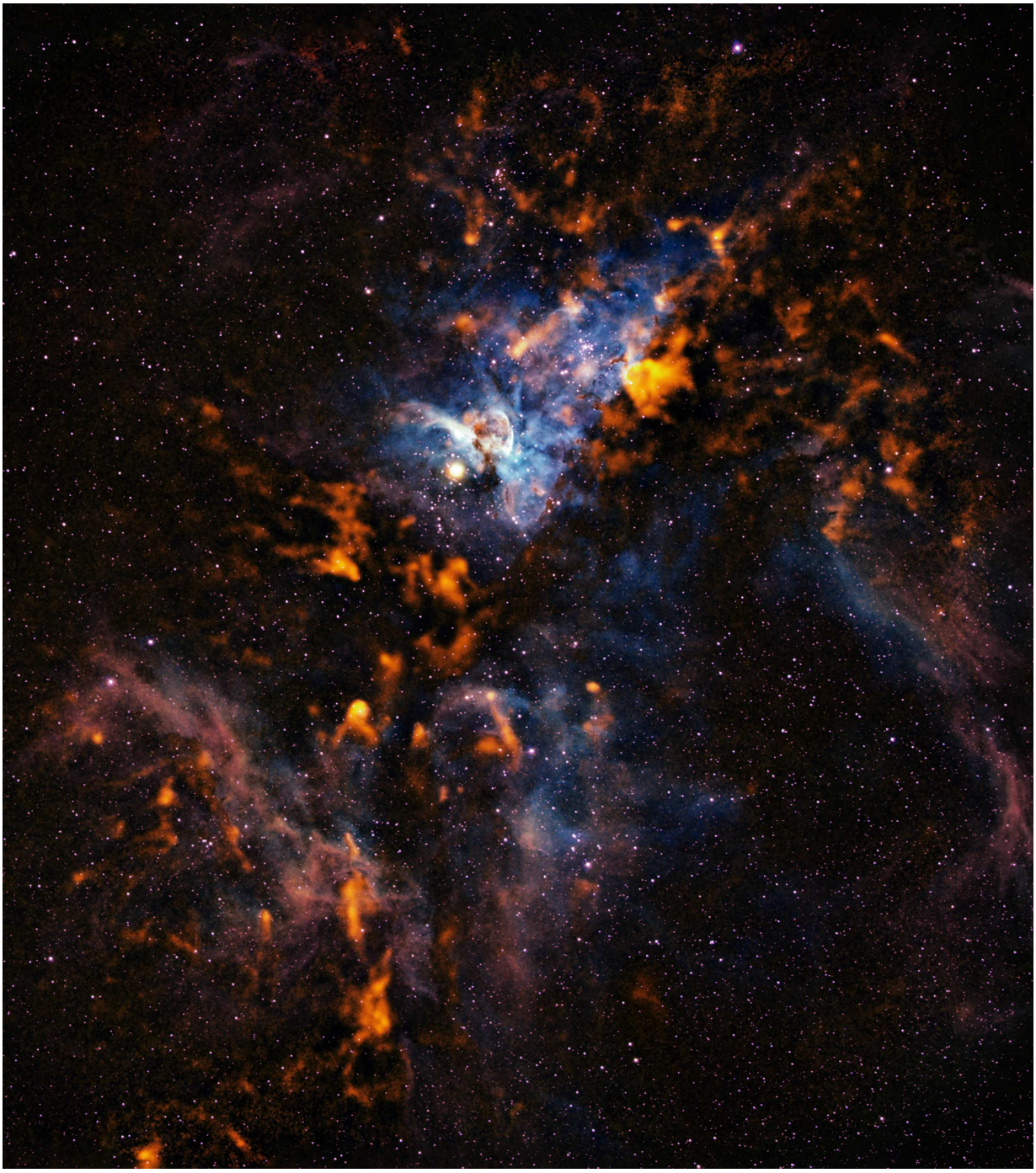

Figure 1.10: Submillimeter view of the Carina Nebula taken at the APEX telescope with the LABOCA camera at 870 μm in orange, combined with a visible light image from the Curtis Schmidt telescope at the Cerro Tololo Interamerican Observatory. Image credits: ESO/APEX/T. Preibisch et al. (Submillimetre); N. Smith, University of Minnesota/NOAO/AURA/NSF (Optical).

Submillimeter: The very cold molecular component is visible in observations of the region at sub-mm wavelengths by Preibisch et al. (2011a). They used the Large APEX Bolometer Camera LABOCA at the APEX telescope to obtain a map of the cold clumps in Carina (figure 1.10). They find a wide range of cloud sizes and masses ranging from several $10^3\,M_\odot$, to smaller clouds of the order of $1\,M_\odot$, which allowed them to determine a clump mass function as described in Pekruhl et al. (2013).

1.6.2 Evidence for Triggered Star Formation

The rich young stellar component of the Carina Nebula, offers some clue on the possible impact of massive star feedback on the formation of new stars. The age spread among

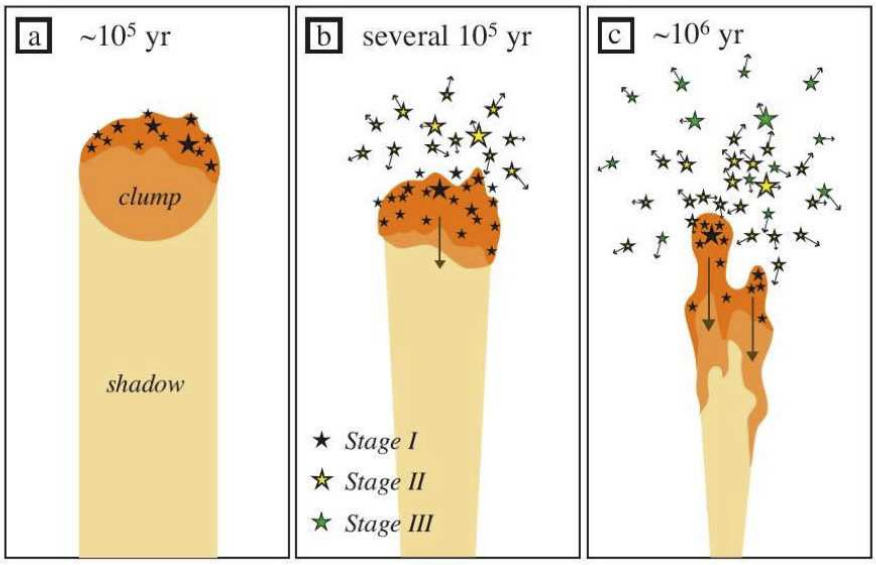

Figure 1.11: Illustration of the triggering of new stars at the tip of a pillar. Image credit: Figure 15 in Smith et al. (2010b).

the stellar objects obtained from the analysis of the X-ray data (Povich et al., 2011) and the photometry in the near- and mid-infrared of the detected sources (Preibisch et al., 2011c) provided evidence for a spread of the ages of the sources between $< 1\,$Myr and almost 8 Myr. This is possibly an indication for a time sequence of star-forming events. The spatial distribution of protostars and YSOs detected by *Herschel* (Gaczkowski et al., 2013) as well as the protostellar outflows identified in the optical by HST/ACS (Smith et al., 2010a) and in the infrared by *Spitzer* (Ohlendorf et al., 2012), clearly show the tendency of YSOs to be concentrated at the edges and tips of irradiated clouds and pillars. These pillars, exhibit a preferential orientation towards the central clusters containing the massive stars in the complex (Smith et al., 2010b; Roccatagliata et al., 2013).

This would appear consistent with a triggered star formation scenario. Smith et al. (2010b) have presented a qualitative description of this process. Figure 1.11 illustrates

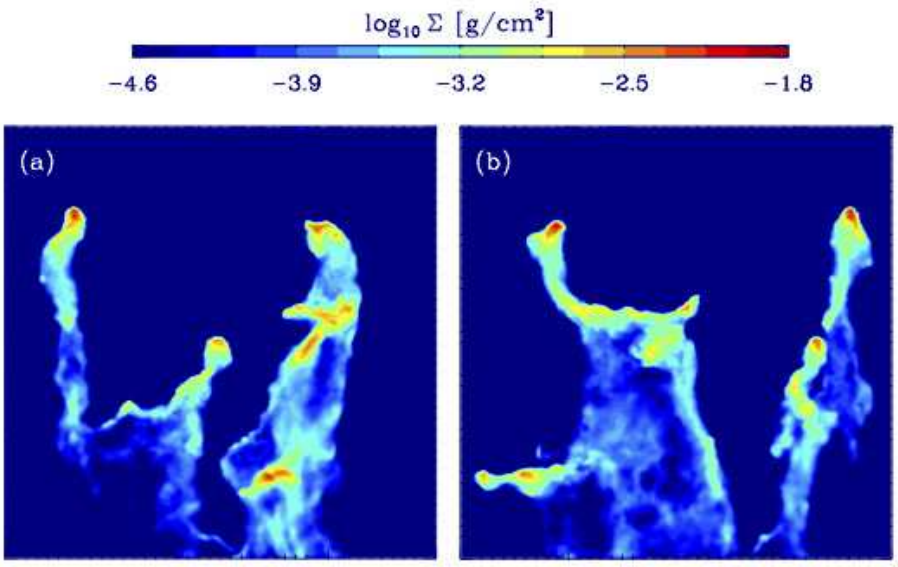

Figure 1.12: Projected surface density of the pillars formed in a simulation by Gritschneder et al. (2010) of the external irradiation of a turbulent cloud. Panel (a) shows the x - y projection, panel (b) is the x - z projection. The surface density is color-coded. The enhanced density tips of the pillars are seen in red. Image credit: Figure 6 in Gritschneder et al. (2010).

this mechanism. The three panels represent different stages of a clouds evolution along a time sequence. First, in panel (a), the gas clump (orange blob) is compressed by the feedback from the star inducing the formation of a first generation of new stars at its upper edge (Stage I protostars; black stars). In the middle panel the clump is accelerated downwards. The first generation of stars is now outside the clump or pillar while a second generation is formed in the compressed tip of the accelerating clump. The third panel (c) shows a later stage where the clump has been swept even further away. The different generations of triggered star can be identified. Those stars that formed in panel (a) have lost much of their disk material (Stage III YSOs; green stars) and have had time to be broadly dispersed. Those formed in panel (b) are in the process of losing their disks (Stage II YSOs; yellow stars) and are becoming more spatially extended thereby mixing with the green stars. While the youngest objects formed in panel (c) are still embedded in the dusty pillar.

Simulations by Gritschneder et al. (2010) of externally irradiated clouds show that the ionizing radiation is able to create pillar structures with enhanced densities at the tips (see figure 1.12). Their results attest to the plausibility of the proposed triggering scenario.

Chapter 2

Basic Principles of Hydrodynamics

In this chapter we present the set of equations used to describe the macroscopic behavior of interstellar gas. The Boltzmann transport equation describes the statistical behavior of a system which is not in thermodynamical equilibrium. Under the assumption of local thermodynamical equilibrium (LTE), and if the mean free path ℓ between the gas' constituents is very small compared to the characteristic size L of the system described, the state of the gas can be described in terms of average properties of an ensemble of individual particles, like temperature, pressure, density and velocity. In the case of an inviscid flow, the usage of the Euler equations of hydrodynamics to describe a medium becomes appropriate. To describe a medium subject to viscous stress the Euler equations can be extended to the Navier-Stokes equations which include the effect of viscous forces.

In the case of molecular clouds, the mean free path for neutral atoms and molecules is given by

$$\ell = (\sigma n)^{-1}, \tag{2.1}$$

where $\sigma \approx 1 \times 10^{-15}\,\mathrm{cm}^2$ is the effective cross section for proton-proton collisions scattering and n is the mean number density of the cloud (see e.g. Shu, 1991). For a cloud average density of $n = 100\,\mathrm{cm}^{-3}$, the mean free path is then $\ell = 10^{14}\,\mathrm{cm} \approx 3.2 \times 10^{-5}\,\mathrm{pc}$, which is many orders of magnitude lower than the typical sizes L of $10 - 100\,\mathrm{pc}$ for molecular clouds. $\ell \ll L$ is verified and the fluid treatment of molecular gas clouds is thus justified. The fluid approach is valid for most of the thermal gas in the ISM (Shu, 1992, chap. 1).

Two methods can be used to model the evolution of the gas. The first one, the Eulerian method, uses a fixed grid of coordinates in space and calculates the physical parameters of the gas flowing through the coordinate frame. The second approach, the Lagrangian method, uses comoving coordinates. The coordinates trace the movement of a gas element in space and time and the physical parameters are computed in the evolving coordinate frame. In the next sections, we will show both representations of the equations of fluid mechanics (Ward-Thompson & Whitworth, 2011).

2.1 The Euler Equations

The dynamical evolution of a non-viscous fluid is governed by laws describing the conservation of mass, momentum and energy. Together with an equation of state, which relates the density, the temperature and the pressure of the gas, they form a closed set of equations specifying the evolution of the fluid.

The Continuity Equation In a volume V with a surface S, the variation of the mass is due to matter flowing in or out of V through its surface S:

$$\begin{aligned}\frac{\partial}{\partial t}\int \rho dV &= -\int_S \rho\vec{v}\cdot\vec{n}dS \\ &\overset{\text{Gauss's theorem}}{=} -\int_V \nabla\cdot(\rho\vec{v})dV.\end{aligned} \tag{2.2}$$

This gives us the equation of continuity which describes the conservation of mass in a fluid volume:

$$\frac{\partial\rho}{\partial t} + \nabla\cdot(\rho\vec{v}) = 0. \tag{2.3}$$

The Momentum Equation The momentum density of the gas is $\rho\vec{v}$. As above, the change of the total momentum in volume V is determined by how much momentum is flowing in or out and by any external force acting on the volume of gas, which can be expressed as pressure force $-P\vec{n}$ acting on each surface of V

$$\frac{\partial}{\partial t}\int \rho\vec{v}dV = -\int_S \rho\vec{v}\vec{v}\cdot\vec{n}dS - \int_S P\mathbf{I}\cdot\vec{n}dS, \tag{2.4}$$

where we introduced the unit tensor $\mathbf{I}$. Using Gauss' theorem, we obtain:

$$\frac{\partial}{\partial t}\int \rho\vec{v}dV = -\int_V \nabla\cdot(\rho\vec{v}\vec{v} + P\mathbf{I})\,dV. \tag{2.5}$$

Which leads to:

$$\frac{\partial(\rho\vec{v})}{\partial t} + \nabla\cdot(\rho\vec{v}\vec{v}) + \nabla P = 0. \tag{2.6}$$

Equation 2.6 can be rewritten as:

$$\vec{v}\frac{\partial\rho}{\partial t} + \rho\frac{\partial\vec{v}}{\partial t} + \vec{v}\nabla\cdot(\rho\vec{v}) + \rho\vec{v}\cdot\nabla\vec{v} + \nabla P = 0. \tag{2.7}$$

Using equation 2.3 one obtains:

$$\rho\frac{\partial\vec{v}}{\partial t} + \rho\vec{v}\cdot\nabla\vec{v} + \nabla P = 0. \tag{2.8}$$

The Energy Equation The total energy of a fluid element can be expressed as the sum its internal energy and its kinetic energy

$$\rho e_{tot} = \rho\epsilon + \frac{1}{2}\rho v^2, \tag{2.9}$$

where e_{tot} is the total specific energy and ϵ is the specific internal energy.

The change in energy in V is determined by the transport of energy through the volume surface and the work imparted by the external medium, which at a given position can be expressed in terms of the pressure by $P\vec{v}\cdot\vec{n}$. The conservation equation is then:

$$\frac{\partial}{\partial t}\int \rho\left(\epsilon+\frac{1}{2}v^2\right)dV = -\int_S \rho\left(\epsilon+\frac{1}{2}v^2\right)\vec{v}\cdot\vec{n}dS - \int_S P\vec{v}\cdot\vec{n}dS, \tag{2.10}$$

Which leads to:

$$\begin{aligned}\frac{\partial}{\partial t}\int \rho\left(\epsilon+\frac{1}{2}v^2\right)dV &= -\int_S \rho\left(\epsilon+\frac{1}{2}v^2\right)\vec{v}\cdot\vec{n}dS - \int_S P\vec{v}\cdot\vec{n}dS \\ &\overset{\text{Gauss's theorem}}{=} -\int_V \nabla\cdot\left[\left(\rho\epsilon+\frac{1}{2}\rho v^2+P\right)\vec{v}\right]dV,\end{aligned} \tag{2.11}$$

and can be written as:

$$\frac{\partial}{\partial t}\ (\rho e_{tot}) + \nabla\cdot\left[\left(\rho e_{tot}+P\right)\vec{v}\right] = 0. \tag{2.12}$$

Using equation 2.3 we obtain:

$$\rho\frac{\partial e_{tot}}{\partial t} + \nabla\cdot(P\vec{v}) = 0. \tag{2.13}$$

2.2 The Lagrangian Form of the Euler Equations

The Euler equations describe the independent physical quantities $\rho(\vec{x},t)$, $\vec{v}(\vec{x},t)$ and $e(\vec{x},t)$ as time dependent field variables at a position $\vec{x}$. The Lagrangian picture follows the motion of a fluid element and describes as the physical quantities change along its path. This requires the introduction of the comoving time derivative:

$$\frac{d}{dt} \equiv \frac{\partial}{\partial t} + \vec{v}\cdot\nabla. \tag{2.14}$$

The Continuity Equation Equation 2.3 can now be written as:

$$\frac{d\rho}{dt} = -\rho\nabla\cdot\vec{v}. \tag{2.15}$$

This means that the divergence of the velocity field leads to a change in density.

The Momentum Equation Using the comoving derivative, equation 2.8 can be rewritten as:

$$\frac{d\vec{v}}{dt} = -\frac{\nabla P}{\rho}. \tag{2.16}$$

This means that a gradient in pressure leads to an acceleration of the gas.

The Energy Equation As above, using the definition 2.14, equation 2.13 becomes:

$$\frac{de_{tot}}{dt} = -\frac{P}{\rho}\nabla \cdot \vec{v} - \frac{1}{\rho}\vec{v} \cdot \nabla P, \tag{2.17}$$

with $e_{tot} = \epsilon + \|\vec{v}\|^2/2$. One can write:

$$\frac{d\epsilon}{dt} + \vec{v} \cdot \frac{d\vec{v}}{dt} = -\frac{P}{\rho}\nabla \cdot \vec{v} - \frac{1}{\rho}\vec{v} \cdot \nabla P. \tag{2.18}$$

Using the momentum equation 2.16, one obtains:

$$\frac{d\epsilon}{dt} = -\frac{P}{\rho}\nabla \cdot \vec{v}. \tag{2.19}$$

This means that the thermal energy of the gas changes as a result of adiabatic expansion or compression.

2.3 Short Excursus into Turbulence

As mentioned in subsection 1.2.3, molecular clouds exhibit complex and irregular gas motions. The observed supersonic linewidths have been interpreted as evidence for supersonic turbulence (Zuckerman & Evans, 1974). Larson (1981) presented data showing that the cloud velocity dispersion and cloud size follow a power-law relation, similar to the Kolmogorov-law for subsonic turbulence.

Even though the nature of turbulent flows is still not entirely understood, some fundamental properties have been derived from the properties of the flow (Kolmogorov, 1941; Burgers, 1974). For a viscous, incompressible flow, the continuity and momentum equations (equations 2.3 and 2.8) take the form of the Navier-Stokes equations:

$$\nabla \cdot \vec{v} = 0 \tag{2.20}$$

$$\rho\left(\frac{\partial \vec{v}}{\partial t} + \vec{v} \cdot \nabla \vec{v}\right) = -\nabla P + \rho\nu\nabla^2\vec{v}, \tag{2.21}$$

with ν being the kinematic viscosity of the gas.

The incompressible nature of the flow keeps the density constant. This is essentially described by equation 2.20. The motion of the gas then depends on the relative importance of the inertial forces and the viscous forces, which is given by the Reynolds number.

It is dependant on the flow's kinematic viscosity ν, on a characteristic velocity v_l at a characteristic length l of the fluid system.

$$R_e \equiv \frac{l v_l}{\nu} \tag{2.22}$$

When the viscous force $\nu\nabla^2\vec{v}$ is large enough to dampen out variations in the velocity, the Reynolds number is small ($R_e < 100$). The flow appears more ordered and laminar. When the inertial $\vec{v}\cdot\nabla\vec{v}$ force exceeds the viscous $\nu\nabla^2\vec{v}$ force, $R_e \gg 100$ increases, nonlinear effects and small scale motions become more relevant. The laminar flow becomes unstable and turbulent. Energy is transferred to smaller scales. This is called the turbulent energy cascade, which develops between a driving scale, L, at which energy is injected, and a dissipation scale l_ν comparable to the mean free path ℓ, where viscous effects become relevant.

On scales $L \gg l \gg l_\nu$ also called the inertial range, the dynamics are dominated by the advection term $\vec{v}\cdot\nabla\vec{v}$ in equation 2.21, and can be treated as non-dissipative. On these scales the properties of turbulence can be considered independent of the boundary conditions, i.e. how energy is injected at the scale L or how it is dissipated at the scale l_ν. The transfer rate of specific energy in this range is independent of scale, therefore depends on the kinetic energy per unit mass at a scale l (which is of order v_l^2) during a transfer time $t_l \approx l/v_l$

$$\varepsilon \propto v_l^2/t_l = v_l^3/l. \tag{2.23}$$

This results in

$$v_l \propto \varepsilon^{1/3} l^{1/3}. \tag{2.24}$$

This leads to the Kolmogorov energy spectrum in k-space ($k_l = 2\pi/l$):

$$E(k_l) \propto \varepsilon^{2/3} k_l^{-5/3}, \tag{2.25}$$

and to the power spectrum of velocity fluctuations in 3D

$$P_v(k_l) \propto k_l^{-11/3}, \tag{2.26}$$

which translates into a root mean square velocity fluctuation:

$$\langle \delta v^2 \rangle^{1/2} \propto l^{1/3}. \tag{2.27}$$

In numerical simulations the dissipation scale l_ν is not given by the mean free path ℓ but rather by the numerical dissipation that occurs at the resolution limit of the numerical calculations.

The ISM exhibits strong shocks which are an indication of compressible, supersonic turbulence which is better described by Burgers turbulence which yields an energy spectrum

$$E(k_l) \propto k_l^{-2}, \tag{2.28}$$

and a 3D power spectrum

$$P_v(k_l) \propto k_l^{-4}. \tag{2.29}$$

The root mean square velocity fluctuation follow

$$\langle \delta v^2 \rangle^{1/2} \propto l^{1/2}. \tag{2.30}$$

As mentioned in section 1.2.3, the velocity power spectrum in equation 2.29 and the corresponding expression for the velocity fluctuations (equation 2.30) are compatible with the observed *size – linewidth* relation in molecular clouds (equation 1.1 in section 1.2.1).

Chapter 3

The Physics of Stellar Wind Bubbles and H II Regions

In this chapter, we review the development and evolution of stellar wind bubbles and H II regions in a uniform density environment. We present the analytical 1D-expansion laws derived for the feedback-blown bubbles during the main sequence phase of a massive star. We briefly mention the main hydrodynamical instabilities associated with expanding shells.

3.1 Theory of Stellar Wind Bubbles

The evolution of stellar wind bubbles (SWBs) has been studied in great detail analytically (Castor et al., 1975; Weaver et al., 1977; Ostriker & McKee, 1988; Capriotti & Kozminski, 2001). In the classical picture, the wind bubble expansion into a uniform medium during the main sequence stage can be divided into three stages (Lamers & Cassinelli, 1999). The first two phases, the free-expansion phase and the fully adiabatic phase, are of very short duration ($\sim 10^2$ yrs and $\sim 10^3$ yrs respectively; Lamers & Cassinelli 1999). The third phase, the snowplow phase, is the longest ($\geq 10^6$ yrs) and lasts for most of the star's main sequence life and is therefore more likely to be observed. This phase describes the evolution of a cold shell of swept-up interstellar gas, encompassing the shocked wind material.

The shocked stellar wind can reach temperatures $> 10^7$ K and might not cool efficiently. Depending on whether or not the hot shocked wind region can cool on a timescale shorter than the dynamical expansion timescale, one can distinguish between two regimes. The first one is an *energy conserving* snowplow phase where the hot shocked wind remains almost adiabatic and the high pressure drives the expansion of a thin shell of swept up nebular material (see e.g. Castor et al., 1975). The second is a *momentum conserving* snowplow regime where the wind material has cooled and collapsed and the thin shell is driven by the momentum of the wind (see e.g. Steigman et al., 1975).

The question of whether or not the hot interior is able to cool has not been fully answered yet. Different scenarios for the evolution of SWBs have been considered. Weaver

et al. (1977) showed, assuming that the shocked wind region is delimited by a collisionless shock at the interior and by an insulating contact discontinuity from the outside, that the hot wind material would mainly cool by adiabatic expansion, with cooling timescales of the order of the main-sequence life of a massive star. The inclusion of thermal conduction effects at the contact discontinuity do not lead to a drastically different evolution. Capriotti & Kozminski (2001) revisited and expanded the description by Weaver et al. (1977). They considered the case when the insulating contact discontinuity is breached and the mixing of wind and ambient material becomes possible. They argued that discarding the assumption of a contact discontinuity and assuming effective mass exchange and mixing between the shocked wind and the ambient material would lead to effective cooling in the bubble and a snowplow regime that is mostly momentum driven.

In the following sections, we present the expansion laws for SWBs resulting from these different assumptions.

3.1.1 Insulating Contact Surfaces

The Purely Adiabatic Phase The structure of SWBs presented in the groundbreaking works by Castor et al. (1975) and Weaver et al. (1977) describe the so-called *classical* evolution of wind-blown bubbles. They describe SWBs as a four-zone structure (see figure 3.1) consisting of:

Zone *w*: an innermost, hypersonic free flowing stellar wind with radius R_w

Zone *sw*: a hot, almost isobaric region of shocked stellar wind with radius R_{sw}

Zone *sn*: a dense, shocked shell at radius R_{sn}, expanding at velocity $\dot{R}_{sn}$ containing most of the swept-up interstellar gas

Zone *un*: an ambient interstellar gas of density ρ_{un}

The innermost free-flowing wind has the density profile $\rho_w(r) = \dot{M}/4\pi r^2 v_{\mathrm{WIND}}$; $\dot{M}$ being the stellar wind mass loss rate, v_{WIND} the wind's terminal velocity and r being the distance from the stellar source. The free-flowing wind hits a termination shock at R_w where most of its kinetic energy is converted into heat and the shocked wind material reaches temperatures of $\sim 10^6\,\mathrm{K}$ – $10^8\,\mathrm{K}$ in zone *sw*. The hot gas in this region is separated and insulated from the non-radiating but cooler shocked nebular gas, by a contact discontinuity at R_{sw} (Pikel'Ner, 1968; Dyson & de Vries, 1972).

During the adiabatic phase radiative cooling is not very important. The gas cools only due to the work done by the expansion driven by the overpressured bubble. Zone *sn* is initially filled with still hot swept-up ISM gas with an outer shock front at position R_{sn}. The attributes of region *sn* are given by the adiabatic Rankine-Hugoniot jump conditions

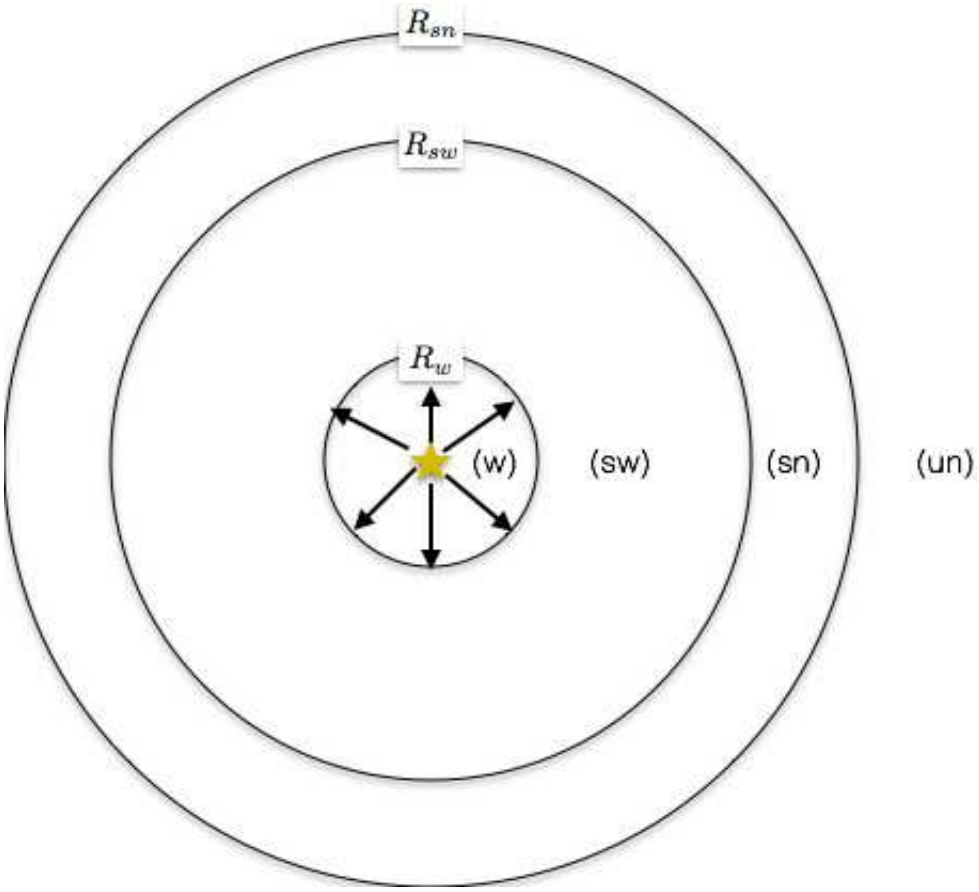

Figure 3.1: Sketch of the structure of a classical wind bubble based on Weaver et al. (1977).

at R_{sn} (assuming $T_{un} = 0\,\mathrm{K}$):

$$\rho_{sn} = 4\rho_{un}\,, \tag{3.1a}$$

$$v_{sn} = \frac{3}{4}\dot{R}_{sn}\,, \tag{3.1b}$$

$$c_{sn}^2 = \frac{3}{16}\dot{R}_{sn}^2\,, \tag{3.1c}$$

$$P_{sn} = \frac{3}{4}\rho_{un}\dot{R}_{sn}^2\,. \tag{3.1d}$$

Where P_{sn}, c_{sn}, v_{sn}, ρ_{sn} are respectively the pressure, the sound speed, the gas velocity and the density in region *sn*. $\dot{R}_{sn}$ is the velocity of the outer shock front at R_{sn}. The mass in zone *sn* is:

$$\begin{aligned} M_{sn} &= 4/3\pi\rho_{un}R_{sn}^3 \\ &= \frac{4}{3}\pi\rho_{sn}\left(R_{sn}^3 - R_{sw}^3\right). \end{aligned} \tag{3.2}$$

Conservation of energy equates the sum of the thermal energy of all the shocked gas and the kinetic energy of region *sn* to the total wind energy.

$$\frac{4}{3}\pi R_{sn}^3\left(\frac{3}{2}P_{sn}\right)+\frac{4}{3}\pi R_{sn}^3\rho_{un}\left(\frac{1}{2}v_{sn}^2\right)=\frac{1}{2}\dot{M}v_{\rm WIND}^2 t. \tag{3.3}$$

The kinetic energy of the hot shocked wind is neglected since $M_{sw} << M_{sn}$. Using equations 3.1b and 3.1d in equation 3.3 and assuming $R_{sn}(t)=f(\dot{M},v_{\rm WIND},\rho_{un})t^{\gamma}$, we find

$$R_{sn}(t)=0.75\dot{M}^{1/5}v_{\rm WIND}^{2/5}\rho_{un}^{-1/5}t^{3/5}. \tag{3.4}$$

Equation 3.2 yields:

$$R_{sw}(t)=0.91R_{sn}(t). \tag{3.5}$$

The radius of zone w is estimated by equating the ram pressure at R_w to the pressure in zone *sw*

$$R_w(t)=0.72\dot{M}^{3/10}v_{\rm WIND}^{1/10}\rho_{un}^{-3/10}t^{2/5}. \tag{3.6}$$

This fully adiabatic stage is only relatively short-lived and lasts only about a few $\sim 10^3$ yr (Castor et al., 1975; Lamers & Cassinelli, 1999).

Cooled Shell Phase When radiative cooling dominates over adiabatic cooling in zone *sn*, the swept up gas is expected to have cooled to a temperature of $\sim 10^4$ K. Assuming the same temperature for the outer undisturbed gas, the outer shock at R_{sn} is now isothermal.

$$\rho_{sn}c_{un}^2=\rho_{un}\dot{R}_{sn}^2, \tag{3.7a}$$

$$v_{sn}=\dot{R}_{sn}\left[1-\left(\frac{c_{un}}{\dot{R}_{sn}}\right)^2\right], \tag{3.7b}$$

v_{sn} being the velocity of the shocked nebular gas at R_{sn} and c_{un} being the sound speed of the undisturbed medum. The shock dissipates when $v_{sn}\approx c_{un}$, i.e. when $\dot{R}_{sn}\approx 1.6c_{un}$ and $\rho_{sn}\approx 2.6\rho_{un}$. The mass of the shocked nebular gas is still given by equation 3.2. Using equation 3.7a one obtains:

$$\left(\frac{R_{sw}}{R_{sn}}\right)^3=1-\left(\frac{c_{un}}{\dot{R}_{sn}}\right)^2. \tag{3.8}$$

This sets the minimum value for the ratio $R_{sw}/R_{sn}\approx 0.85$ and the shock thickness $\Delta R_{sn}\approx 0.17R_{sw}$. The gas shell can be considered thin compared to the hot bubble size. This prompts the assumptions $R_{sn}=R_{sw}$ and $v_{sn}=\dot{R}_{sn}=\dot{R}_{sw}$ for $\dot{R}_{sn}\geq 1.6c_{un}$.

Neglecting radiative cooling in the shocked wind region and assuming its pressure to be uniform, the conservation of energy and momentum can be expressed as:

$$\frac{d}{dt}\left[\frac{4}{3}\pi R_{sn}^3\left(\frac{3}{2}P_{sw}\right)\right]+P_{sw}\frac{d}{dt}\left(\frac{4}{3}\pi R_{sn}^3\right)=\frac{1}{2}\dot{M}v_{\rm WIND}^2, \tag{3.9}$$

and

$$\frac{d}{dt}\left[\left(\frac{4}{3}\pi R_{sn}^3\rho_{un}\right)\dot{R}_{sn}\right] = 4\pi R_{sn}^2 P_{sw} \quad \Rightarrow \quad P_{sw} = \rho_{un}\left(\dot{R}_{sn}^2 + \frac{1}{3}R_{sn}\ddot{R}_{sn}\right). \tag{3.10}$$

Equations 3.9 and 3.10 yield:

$$R_{sn}(t) = 0.66\dot{M}^{1/5}v_{\rm WIND}^{2/5}\rho_{un}^{-1/5}t^{3/5}. \tag{3.11}$$

The free-flowing wind shock front is estimated by equating the ram pressure at R_w to the pressure in the hot bubble

$$R_w(t) = 0.79\dot{M}^{3/10}v_{\rm WIND}^{1/10}\rho_{un}^{-3/10}t^{2/5}. \tag{3.12}$$

3.1.2 Thermally Conducting Contact Surfaces

As an extension to the insulating contact discontinuity model, Weaver et al. (1977) explored the effects of heat transfer from the hot shocked wind gas to the shocked nebular material. In this case an additional zone is added to the overall structure of a wind bubble. Figure 3.2 depicts the five different zones that arise in the fully conductive case. The first zone *w* is occupied by the free-flowing wind which stops at R_w. The second zone *sw* contains the hot shocked wind material and ends at R_{sw}. The third zone *swn* is not present in the previous model and is made of shocked nebula material in the temperature range between the temperature at the contact discontinuity and the temperature of the shocked nebula ($T_{sw} < T_{swn} < T_{sn}$). The fourth zone *sn* contains shocked nebula gas at $T_{sn} = 10^4\,\mathrm{K}$ and the outer zone *un* is occupied by undisturbed gas at $T_{un} = 10^4\,\mathrm{K}$.

Assuming the pressure to be equal in zone *sw* and *swn*, Weaver et al. (1977) modified their mass, momentum and energy equations to allow for radiative losses and to include the time evolution of the innermost boundary $R_w(t)$. Thermal conductivity causes gas from the shell to evaporate into the hot bubble. In the shell the mass loss is minor compared to the mass gained from sweeping up the ISM. For the hot bubble, the matter evaporating from the shell dominates over the stellar wind material. When the cooling in region *sw* becomes non-negligible, the luminosity of region *sw* L_{sw} must be taken into account. Weaver et al. (1977) approximated the functional form of the luminosity by:

$$L_{sw} \propto \frac{R_{sw}^3}{R_w^4}\left(\frac{M_{sw}}{E_{sw}}\right)\left(1 - \frac{R_w}{R_{sw}}\right). \tag{3.13}$$

The evolution of the bubble is then given by the equations:

$$\frac{d}{dt}\frac{4\pi\rho_{un}}{3}R_{sw}^3\dot{R}_{sw} = 4\pi R_{sw}^2(P_{sw} - P_{un}), \tag{3.14}$$

$$\frac{dM_{sw}}{dt} = C_1 T_{sw}^{5/2} R_{sw}^2 (R_{sw} - R_w)^{-1} - C_2\frac{\mu}{k_b T'}L_{sw}, \tag{3.15}$$

$$\frac{dE_{sw}}{dt} = \frac{1}{2}\dot{M}v_{\rm WIND}^2 - 4\pi R_{sw}^2 P_{sw}\frac{dR_{sw}}{dt} - L_{sw}, \tag{3.16}$$

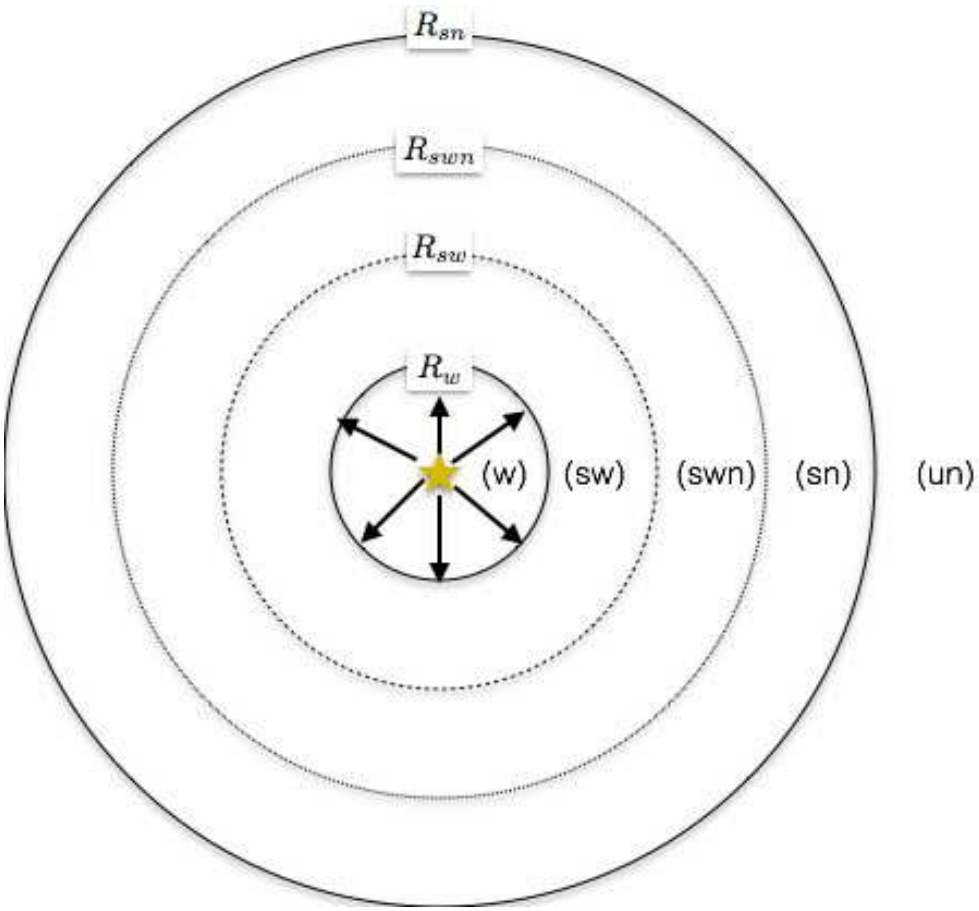

Figure 3.2: Sketch of the structure of a wind bubble in the fully conductive Model described in Weaver et al. (1977) and Capriotti & Kozminski (2001).

where P_{un} is the pressure in the undisturbed medium; $C_1 = 4.13 \times 10^{-14}$ (cgs); $C_2 = 2.00$, $T' = 2 \times 10^5$ K is the temperature at which the time-dependent cooling curve peaks. The evolution equations are solved using initial conditions taken from the similarity solution at a chosen time t_0. As a result Weaver et al. (1977) found the expansion laws $R_{sn}(t) \propto t^{2.9/5}$ and $R_w(t) \propto t^{2.2/5}$. Capriotti & Kozminski (2001), using the same method as Weaver et al. but with updated cooling curves, recovered expansion laws very similar to the insulating contact surface case. Both papers argue that the addition of radiation from the hot shocked gas does not have a noticeable effect on the expansion of R_{sn} compared to the thermally insulating case.

3.1.3 Mixing of Wind and Nebular Material

The previous models assume a segregation of shocked wind material and shocked nebular gas at the contact discontinuity R_{sw}. In the light, however, of simulation results by Garcia-Segura et al. (1996a) which show that hydrodynamical instabilities can feed cooler shocked

nebular gas into the interior of hot bubbles, Capriotti & Kozminski (2001) investigated the bubble evolution in case of efficient mixing between the cooler shocked nebular gas and the hot shocked wind gas. In this case, the previously hot shocked wind region and the shocked nebular region can reach thermal equilibrium. The hot wind gas can cool to a temperature of $T_{sw} = 10^4\,\mathrm{K}$, since the mass of the shocked nebular gas is far in excess of the mass of wind material. The region with the mixed wind and nebular gas is driven solely by the ram pressure of the free-flowing wind. Figure 3.3 depicts the bubble structure arising in this scenario.

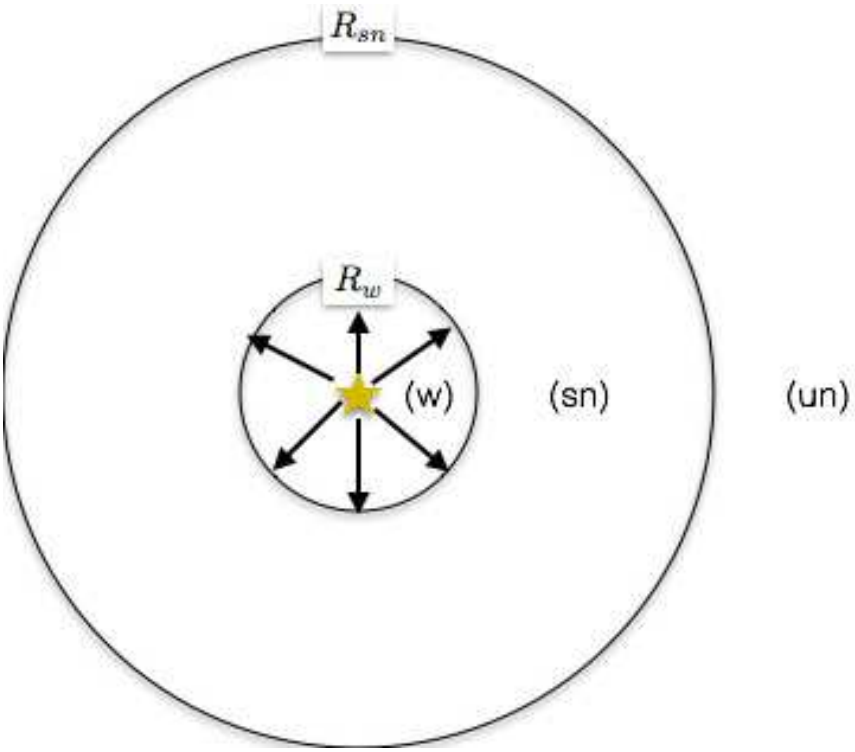

Figure 3.3: Sketch of the structure of a wind bubble in the efficient mixed gas model described in Capriotti & Kozminski (2001).

Momentum conservation gives:

$$\frac{\pi}{3}\rho_{un}\frac{d^2(R_{sn}^4)}{dt^2} = 4\pi\rho_w v_{\mathrm{WIND}}^2 R_{sn}^2 = \dot{M} v_{\mathrm{WIND}}. \tag{3.17}$$

The solution to equation 3.17 can be calculated as

$$R_{sn}(t) = 0.83\dot{M}^{1/4} v_{\mathrm{WIND}}^{1/4} \rho_{un}^{-1/4} t^{1/2}. \tag{3.18}$$

A similar relation has also been described by Steigman et al. (1975) in their treatment of circumstellar shells.

3.2 Dynamical Impact of the Ionizing Radiation

Massive stars produce a high flux of ionizing Lyman continuum photons with energies above 13.6 eV which ionize and heat neutral hydrogen gas in their surrounding (We neglect the ionization of He atoms). The photoionization process is counteracted by the recombination of protons and electrons. In equilibrium, the rate $\dot{N}_{\rm Lyc}$ at which the star emits ionizing photons equals the rate of proton-electron recombinations.

$$\dot{N}_{\rm Lyc} = \frac{4\pi R_S^3}{3}\alpha_r n_p n_e, \tag{3.19}$$

where the equilibrium radius R_S, known as the *Strömgren radius* characterizes the size of the H II region (Strömgren, 1939). n_p and n_e are the number densities of protons and electrons respectively, in a fully ionized region we approximate $n_p = n_e \equiv n$. α_r is the recombination coefficient for atomic hydrogen.

Recombinations directly to the ground state will produce photons able to ionize nearby H atoms. In an optically thick medium all these "secondary" diffuse photons are very likely to be absorbed close to to their emission location. This assumption is known as the *On-the-Spot* (OTS)-approximation. In the OTS-approximation the recombination coefficient becomes $\alpha_r = \alpha_B \approx 2 \times 10^{-13}\,{\rm cm^3\,s^{-1}}$ for a typical H II region temperature of 10^4 K, where α_B is the recombination coefficient summed over all atomic transition levels above the ground level (Osterbrock & Ferland, 2006).

From equation 3.19 we obtain the expression for the Strömgren radius:

$$R_S \approx \left(\frac{3\dot{N}_{\rm Lyc}}{4\pi\alpha_B}\right)^{1/3} n^{-2/3}. \tag{3.20}$$

3.2.1 The Expansion of H II Regions

The transition between the ionized region and the neutral region, the so-called *ionization front* (IF), is very sharp. In a first stage of evolution the IF moves away from the star and heats the circumstellar gas but leaves it otherwise undisturbed. The velocity of the IF is given by (Spitzer, 1978):

$$\dot{R}_i = \frac{1}{4\pi n R_i^2}\left(\dot{N}_{\rm Lyc} - \frac{4\pi}{3}n^2\alpha_B R_i^3\right), \tag{3.21}$$

where R_i is the radius of the ionization front. The velocity of the undisturbed gas relative to the ionization front is $u_{un} > 2c_i$ and the ionized gas has the relative velocity $u_i > c_i$, c_i being the isothermal sound speed in the ionized gas. The IF is called a *weak R-type* front.

As the IF advances into the neutral gas, the ionizing flux decreases, $u_{un} \approx 2c_i$ and $u_i \approx c_i$, the IF becomes *R-critical*. The ionized gas moves sonically with respect to the IF. A pressure wave overtakes the IF. Since $c_i \gg c_{un}$ a shock is formed which compresses the neutral gas. The IF is now called a *D-type* front. This marks the beginning of the

expansion phase for the heated nebular gas. The density inside the H II region is reduced and more gas can be ionized. The radius of the ionization front, then evolves following (Spitzer, 1978):

$$R_i = R_s \left[1 + \frac{7c_i(t - t_S)}{4R_S}\right]^{4/7}, \tag{3.22}$$

where t_S is the time at which the transition from R-type to D-type IF occurs.

3.2.2 Combining the Effects of Winds and Photoionization

Capriotti & Kozminski (2001) compared the effects of photoionization and winds. They introduced the parameter β which is a measure of the wind power to the stellar luminosity which does not vary strongly with the luminosity for O-type stars with similar wind velocities. They also defined R_{pc} a radius like variable and t_5 a time like variable as

$$\begin{aligned} R_{pc} &= R_{sn}\left[\frac{(n_{un}/L_4)^{1/2}}{3.08\times10^{20}}\right] \quad \mathrm{pc}\,(\mathrm{cm}^3\,10^4\,\mathrm{L}_\odot)^{-1/2}, \\ t_5 &= t\left[\frac{(n_{un}/L_4)^{1/2}}{3.14\times10^{9}}\right] \quad \mathrm{yr}\,(\mathrm{cm}^3\,10^4\,\mathrm{L}_\odot)^{-1/2}. \end{aligned} \tag{3.23}$$

In this variable space, wind-blown bubbles can be described by a single relation of the form $R_{pc} = f(\beta)t_5^\gamma$ with $\gamma = 1/2$ for the momentum driven case and $\gamma = 3/5$ for the pressure or energy driven case.

Figure 3.4 compares the evolution of ionized bubbles and wind bubbles in the $R_{pc} - t_5$-space. It shows a family of curves parametrized by values of $(L_4 n_{un})^{1/2}$ for $v_{\mathrm{WIND}} = 3 \times 10^3\,\mathrm{km\,s^{-1}}$ and stellar luminosity $L_4 = L/10^4 = 10\,\mathrm{L}_\odot$ for the evolution of the radius of the ionization sphere as a function of time. The endpoints marked by filled circles represent the end of the star's main-sequence lifetime, while those ending by a vertical line indicate the dissipation of the shock when $v_{sn} = c_{un}$ (at $T_{un} = 100\,\mathrm{K}$). The dotted line represents the radius of the wind-induced shock front in the nebular gas as a function of time for the case of an insulating contact surface with the endpoint marked by a vertical line corresponding to $v_{sn} = c_{un}$ (at $T_{un} = 10^4\,\mathrm{K}$). The dot-dashed extension corresponds to the expansion of the wind-induced shock front into a cold gas ($T_{un} = 100\,\mathrm{K}$). The filled square represents bubble collapse due to cooling of the wind gas. The short dashed line represents the dependence of the radius of the wind-induced shock front on time after bubble collapse. The dashed line represents the dependence of the radius of the wind-induced shock front on time for the case of complete mixing and cooling of shocked wind and shocked nebular gas. Its termination is marked by a vertical line at the time when $v_{sn} = c_{un}$ (at $T_{un} = 10^4\,\mathrm{K}$).

Capriotti & Kozminski (2001) show that the ionizing radiation is the dominant mechanism. Pressure driven winds can have an impact at very early times for very high ambient densities $n_{un} > 10^6\,\mathrm{cm}^{-3}$, but the effects of ionization will rapidly take over and last substantially longer than the winds effect. In the momentum-driven case, the wind never dominates but it can eventually play a role locally, in the case for example of bowshocks and proplyds like in the Orion Nebula (García-Arredondo et al., 2001).

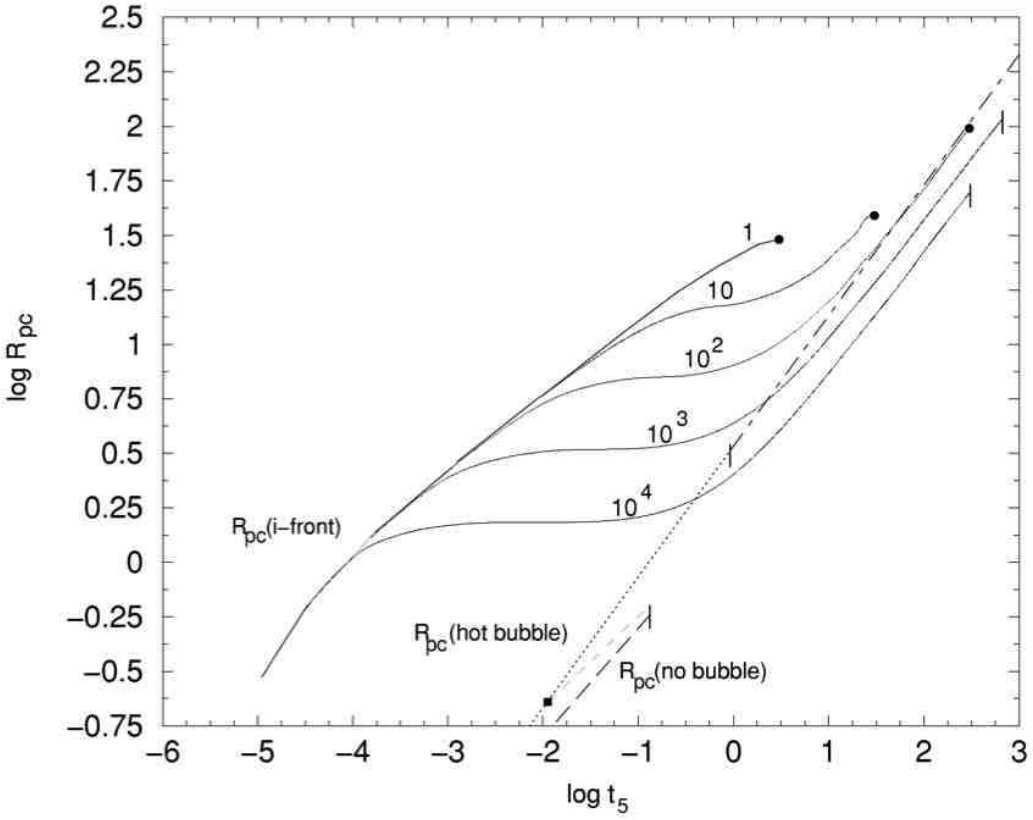

Figure 3.4: Evolution of the outer shock radius over time for the two wind cases and the ionization front for different uniform densities of the ambient medium (from Capriotti & Kozminski, 2001).

3.3 Instabilities

Expanding shells are likely to be affected by hydrodynamical instabilities (Garcia-Segura & Mac Low, 1995; Freyer et al., 2003; Freyer et al., 2006). The most important ones, in the context of expanding wind and H II shells are the Vishniac or thin-shell instability and the Rayleigh-Taylor instability (Mac Low & Norman, 1993; Garcia-Segura et al., 1996b; Bisbas et al., 2009).

The Vishniac instability is expected to occur during the expansion of a thin shell into a homogeneous outer medium (Vishniac, 1983). As discussed in Mac Low & Norman, 1993, this instability arises when the two confining forces acting on the shell are not perfectly aligned i.e. the thermal pressure is always perpendicular to the shell while the ram pressure is not. This results in a transversal force component leading to mass flows along the shell.

Regions with overdensities (valleys) appear where the moving gas accumulates in the shell, along with regions of decreased density (peaks). Figure 3.5 illustrates this phenomenon.

As the overdense regions are less decelerated than the underdense ones, they will move ahead and reverse the transversal flows in the shell leading to an oscillatory movement. The wavelength of the instability is comparable with the thickness of the shell.Vishniac (1983) showed that the amplitude of the oscillation grows with time. Wind-induced shock

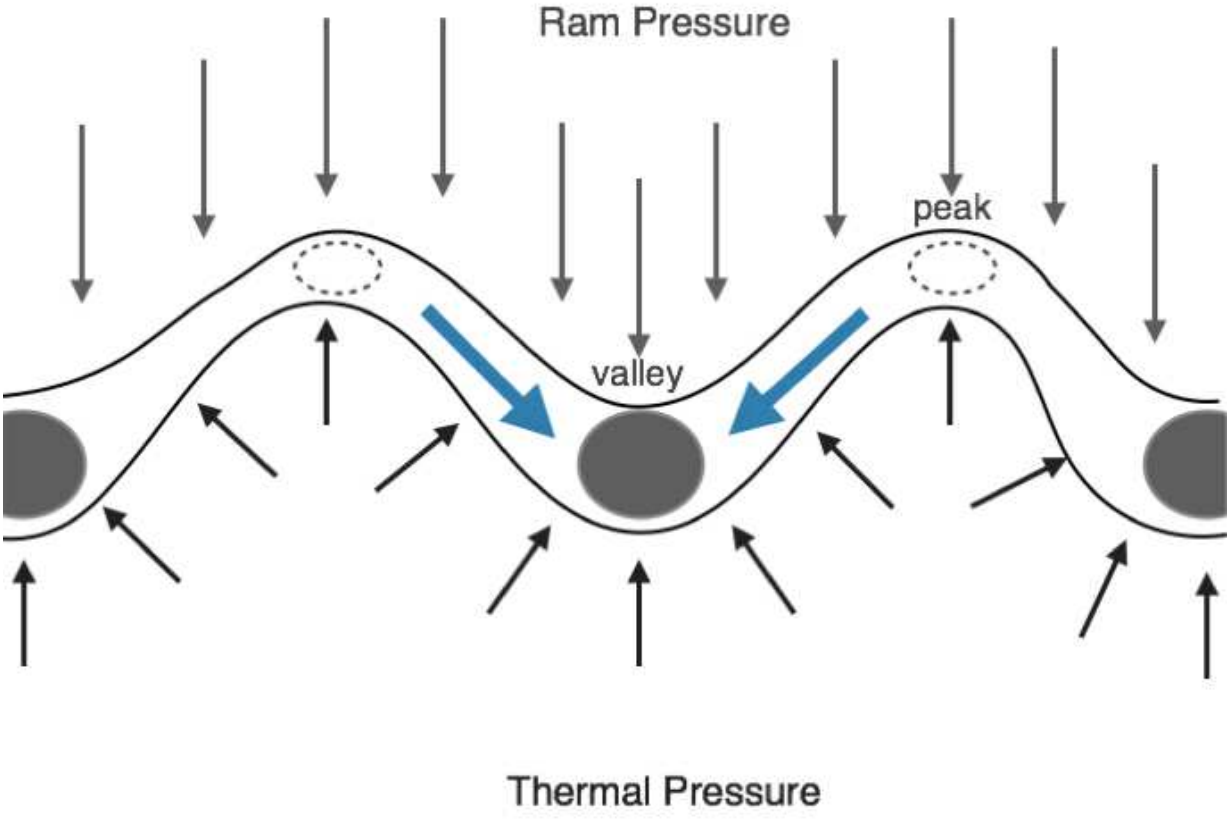

Figure 3.5: Sketch of the Vishniac instability process.

fronts are stable with regard to the thin-shell instability. For H II regions, however, the ionizing radiation will penetrate further through the lower density peaks while the optical depth is increased along the density enhancements in the valleys. This will elongate the peaks and increase the mass flow towards the valleys, eventually leading to a break up of the shell.

The Rayleigh-Taylor instability occurs when the a less dense fluid accelerates a denser one (Taylor, 1950). This is the case for a shell accelerated by the low density ionized gas. At the interface between the two fluids, the effective gravity has an opposite sign to that of the acceleration. Small perturbations at the interface grow exponentially. The resulting structures resemble spikes or plumes reaching into the low density medium. Figure 3.6 shows

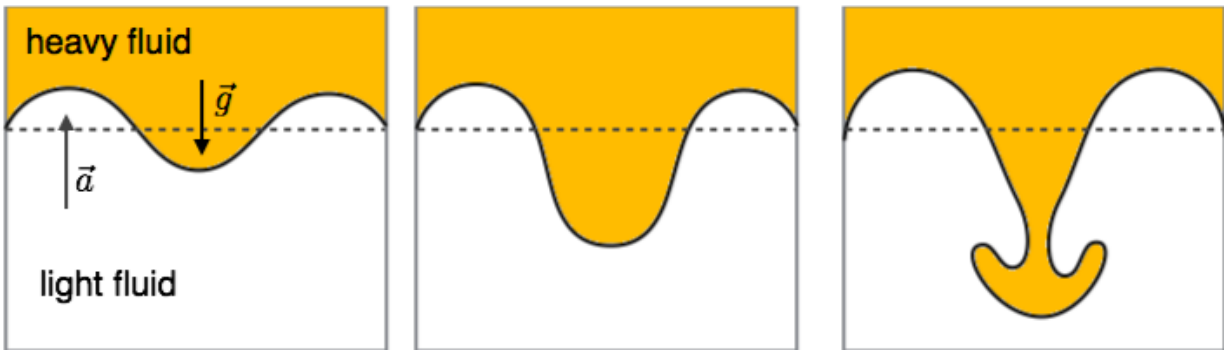

Figure 3.6: Sketch of the Rayleigh-Taylor instability process.

a sketch of the evolution of a Rayleigh-Taylor "finger". This instability is also expected in an ambient medium with a power-law density profile. Small perturbations develop at the interface between the two fluids and are amplified over time (Garcia-Segura & Mac Low, 1995).

Chapter 4

Smoothed Particle Hydrodynamics

The code SEREN (Hubber et al., 2011) uses the Smoothed Particle Hydrodynamics (SPH) method to evolve the fluid equations. SPH was developed by Gingold & Monaghan (1977) and Lucy (1977). It is a method widely use in the astrophysical domain. Several very good reviews have been written on the subject (see e.g. Monaghan, 1992; Monaghan, 2005; Rosswog, 2009; Springel, 2010b; Price, 2012). It is a mesh-free and Lagrangian method. The smallest discrete fluid entity is represented by a '*particle*'. The physical quantities are tracked along the path of each particle. In contrast to grid-based method where quantities are calculated at fixed positions on the grid, field quantities must be mapped onto an irregular distribution of moving particles in SPH. To solve this problem, SPH particles are represented not by a single point mass, but rather by a continuous density distribution inside an extended region. The way this '*particle density*' and other hydrodynamical quantities are computed is the main characteristic of the SPH method. It involves the introduction of a *kernel*-function and the discretized representation of physical quantities.

The following sections are based on the review by Price (2012) and on the description of the SPH implementation in SEREN by Hubber et al. (2011).

4.1 The Kernel Function

$W(|\vec{r} - \vec{r}'|, h)$, the kernel, is a symmetric weight function around the position $\vec{r}'$ of an SPH particle. h, the smoothing length, is a scale parameter which describes the size of the region of influence of the particle. W has the properties

$$\int_{\mathrm{V}} W(|\vec{r} - \vec{r}'|, h) \mathrm{dV} = 1, \tag{4.1}$$

$$\lim_{h \to 0} W(|\vec{r} - \vec{r}'|, h) = \delta(|\vec{r} - \vec{r}'|). \tag{4.2}$$

Equation 4.1 is the normalization condition and equation 4.2 describes the behavior of W in the limit of small h.

An example of a kernel-function in 3 dimensions, which is also the one used in subsequent simulations, is the cubic spline truncated at $2h$ (Monaghan & Lattanzio, 1985)

$$W(|\vec{r}-\vec{r}'|,h)=\frac{1}{\pi h^3}\begin{cases}\frac{1}{4}(2-\frac{|\vec{r}-\vec{r}'|}{h})^3-(1-\frac{|\vec{r}-\vec{r}'|}{h})^3, & 0\le|\vec{r}-\vec{r}'|<h,\\ \frac{1}{4}(2-\frac{|\vec{r}-\vec{r}'|}{h})^3, & h\le|\vec{r}-\vec{r}'|<2h,\\ 0, & |\vec{r}-\vec{r}'|\ge 2h.\end{cases} \tag{4.3}$$

If we consider a quantity A such that

$$A(\vec{r})=\int_{\mathrm{V}}A(\vec{r}')\delta(|\vec{r}-\vec{r}'|)dV', \tag{4.4}$$

using Equation 4.2

$$A(\vec{r})=\lim_{h\to 0}\int_{\mathrm{V}}A(\vec{r}')W(|\vec{r}-\vec{r}'|,h)dV', \tag{4.5}$$

we can define the convolution of $A(\vec{r}')$ with $W(|\vec{r}-\vec{r}'|,h)$ for a small h

$$\bar{A}(\vec{r})=\int_{\mathrm{V}}A(\vec{r}')W(|\vec{r}-\vec{r}'|,h)dV' \tag{4.6}$$

$$=\int_{\mathrm{V}}A(\vec{r}')\frac{W(|\vec{r}-\vec{r}'|,h)}{\rho(\vec{r}')}\rho(\vec{r}')dV'. \tag{4.7}$$

Considering the discretized nature of SPH, the integral in Equation 4.7 can be replaced by the sum over N neighboring particles

$$\bar{A}(\vec{r})=\sum_{i=1}^{N}\frac{m_i}{\rho_i}A(\vec{r_i})W(|\vec{r}-\vec{r_i}|,h), \tag{4.8}$$

where ρ_i is the density of gas corresponding to SPH particle i, m_i is the mass of particle i, $A(\vec{r_i})$ is the value of the function A for particle i.

4.2 The Density Estimate

With Equation 4.8 we can compute the density at a position $\vec{r_i}$:

$$\rho(\vec{r_i})=\sum_{j=1}^{N}m_jW(|\vec{r_i}-\vec{r_j}|,h_i). \tag{4.9}$$

Where $N=N_{neigh}$ is a defined number of neighbors. Equation 4.9 implies that, within a region of defined size smaller than the smoothing length, the density becomes higher, the more particles are located within it. If, however, the distance between particles is higher than h, the SPH kernels do not overlap. The gas density becomes incorrect as it only represents the kernel function. This problem is solved by adopting a variable smoothing length (see section 4.6 below). For simplicity, we present the SPH expressions and fluid equations assuming a constant smoothing length h. The simulation we perform, however, are always done assuming a constant number of neighbors N_{neigh} and a density dependent h.

4.3 Spatial Derivatives

The discretized derivative of quantity A can be expressed as

$$\nabla \bar{A}(\vec{r}) = \sum_{i=1}^{N} \frac{m_i}{\rho_i} A(\vec{r_i}) \nabla W(|\vec{r} - \vec{r_i}|, h), \tag{4.10}$$

with $\nabla \equiv \partial / \partial \vec{r}$. The gradient depends on the values of the scalar field and the gradient of the kernel.

Another form for the derivative can be obtained by stating

$$\nabla \bar{A}(\vec{r}) = \nabla \bar{A}(\vec{r}) - \bar{A}(\vec{r}) \nabla 1. \tag{4.11}$$

In principle $\nabla 1 = 0$, but due to a non zero smoothing length and to the discretization of the scalar field, the SPH estimation of 1 is only approximate:

$$1 \approx \sum_{i=1}^{N} \frac{m_i}{\rho_i} W(|\vec{r} - \vec{r_i}|, h), \tag{4.12}$$

$$0 \approx \nabla 1 \approx \sum_{i=1}^{N} \frac{m_i}{\rho_i} \nabla W(|\vec{r} - \vec{r_i}|, h). \tag{4.13}$$

Using equation 4.11 the derivative takes the form

$$\nabla \bar{A}(\vec{r}) \approx \sum_{i=1}^{N} \frac{m_i}{\rho_i} \left[A(\vec{r_i}) - A(\vec{r}) \right] \nabla W(|\vec{r} - \vec{r_i}|, h). \tag{4.14}$$

This expression has the advantage that it vanishes for constant functions.

More generalized expressions for the spatial derivatives can be constructed. Each gradient operator, can take a symmetric and an antisymmetric form

$$\begin{aligned} \nabla \bar{A}(\vec{r}) &= \frac{1}{\psi} \left[\nabla(\psi \bar{A}) - \bar{A} \nabla \psi \right] \\ &\approx \sum_{i=1}^{N} \frac{m_i}{\rho_i} \frac{\psi_i}{\psi(\vec{r})} \left(A(\vec{r_i}) - A(\vec{r}) \right) \nabla W(|\vec{r} - \vec{r_i}|, h), \end{aligned} \tag{4.15}$$

and

$$\begin{aligned} \nabla \bar{A}(\vec{r}) &= \psi \left[\frac{\bar{A}}{\psi^2} \nabla \psi + \nabla \left(\frac{\bar{A}}{\psi} \right) \right] \\ &\approx \sum_{i=1}^{N} \frac{m_i}{\rho_i} \left(\frac{\psi_i}{\psi(\vec{r})} A(\vec{r}) + \frac{\psi(\vec{r})}{\psi_i} A(\vec{r_i}) \right) \nabla W(|\vec{r} - \vec{r_i}|, h), \end{aligned} \tag{4.16}$$

where ψ is an arbitrary, differentiable scalar quantity, ψ_i being the value of ψ for particle i. Hereafter, we use either $\psi = 1$ or $\psi = \rho$. For a chosen ψ the operator pair defined by equations 4.15 and 4.16 form a conjugate pair. Chosing one for expressing the density gradient tends to lead to the other one in the equations of motion.

Similar expressions can be set up for the vector derivatives:

$$\nabla \cdot \bar{\mathbf{A}}(\vec{r}) \approx \sum_{i=1}^{N} \frac{m_i}{\rho_i} \frac{\psi_i}{\psi(\vec{r})} \left(\mathbf{A}(\vec{r_i}) - \mathbf{A}(\vec{r})\right) \cdot \nabla W(|\vec{r} - \vec{r_i}|, h) \tag{4.17}$$

$$\nabla \times \bar{\mathbf{A}}(\vec{r}) \approx -\sum_{i=1}^{N} \frac{m_i}{\rho_i} \frac{\psi_i}{\psi(\vec{r})} \left(\mathbf{A}(\vec{r_i}) - \mathbf{A}(\vec{r})\right) \times \nabla W(|\vec{r} - \vec{r_i}|, h) \tag{4.18}$$

and

$$\nabla \cdot \bar{\mathbf{A}}(\vec{r}) \approx \sum_{i=1}^{N} \frac{m_i}{\rho_i} \left(\frac{\psi_i}{\psi(\vec{r})} \mathbf{A}(\vec{r}) + \frac{\psi(\vec{r})}{\psi_i} \mathbf{A}(\vec{r_i}) \right) \cdot \nabla W(|\vec{r} - \vec{r_i}|, h) \tag{4.19}$$

$$\nabla \times \bar{\mathbf{A}}(\vec{r}) \approx -\sum_{i=1}^{N} \frac{m_i}{\rho_i} \left(\frac{\psi_i}{\psi(\vec{r})} \mathbf{A}(\vec{r}) + \frac{\psi(\vec{r})}{\psi_i} \mathbf{A}(\vec{r_i}) \right) \times \nabla W(|\vec{r} - \vec{r_i}|, h) \tag{4.20}$$

The latter formulation is used for approximating the pressure gradient $\nabla P/\rho$ as its symmetrical nature ensures that opposite forces between a pair of particles cancel out. This ensures conservation of momentum.

4.4 Errors

The approximation of the delta-function by a smoothing-function and the discretization introduces errors of order $\mathcal{O}(h^2)$ in the SPH estimation of a quantity and its derivative. This error can be reduced by decreasing the smoothing length, while the discretisation error is reduced by increasing the number of sampling points i.e. the number of particles within the smoothing kernel. Increased accuracy however comes at the cost of computational speed and efficiency.

The choice of the gradient estimate is of great importance to the behavior of the particle system. Less accurate estimates like Equation 4.16 (with $\psi = \rho$) ensure local conservation of momentum and lead to a more accurate depiction of the particle motion.

4.5 The SPH Fluid Equations

The Continuity Equation Taking the time derivative of Equation 4.9 for a particle i, we obtain

$$\frac{d\rho(\vec{r_i})}{dt} = \sum_{j=1}^{N} m_j \left[\frac{\partial W_{ij}}{\partial \vec{r_i}} \frac{d\vec{r_i}}{dt} + \frac{\partial W_{ij}}{\partial \vec{r_j}} \frac{d\vec{r_j}}{dt} + \frac{\partial W_{ij}}{\partial h_i} \frac{dh_i}{dt} \right], \tag{4.21}$$

where $W_{ij} = W(|\vec{r_i} - \vec{r_j}|, h_i)$. For simplicity we assume that $h_i = h$ is constant in time. We can reformulate Equation 4.21:

$$\frac{d\rho(\vec{r_i})}{dt} = \sum_{j=1}^{N} m_j \left[\vec{v_i} \cdot \nabla_i W_{ij} + \vec{v_j} \cdot \nabla_j W_{ij}\right]. \tag{4.22}$$

Since $\nabla_j W_{ij} = -\nabla_i W_{ij}$, we can write

$$\frac{d\rho(\vec{r_i})}{dt} = \sum_{j=1}^{N} m_j \left(\vec{v_i} - \vec{v_j}\right) \cdot \nabla_i W_{ij}. \tag{4.23}$$

Which, using Equation 4.14 leads to

$$\frac{d\rho(\vec{r_i})}{dt} = -\rho_i \nabla_i \cdot \vec{v_i}. \tag{4.24}$$

This is equivalent to Equation 2.15. We note, however, that the implementation of equation 4.24 is generally not necessary, since equation 4.9 is used directly.

The Momentum Equation We rewrite Equation 2.16 using Equation 4.16 and $\psi = \rho$

$$\frac{d\vec{v_i}}{dt} = -\sum_{j=1}^{N} m_j \left(\frac{P_i}{\rho_i^2} + \frac{P_j}{\rho_j^2}\right) \nabla_i W_{ij}, \tag{4.25}$$

with ρ_i and ρ_j being the densities and P_i and P_j being the pressure values for the particles i and j.

The Energy Equation We use equation 4.17 with $\psi = 1$ to express the energy equation 2.19:

$$\frac{d\epsilon_i}{dt} = \frac{P_i}{\rho_i^2} \sum_{j=1}^{N} m_j \left(\vec{v_i} - \vec{v_j}\right) \cdot \nabla_i W_{ij}. \tag{4.26}$$

4.6 Variable Smoothing Length

Keeping N_{neigh} constant (often $N_{neigh} = 50$), means that the smoothing length h must vary with the fluid density. A near constant ratio of h to the mean local particle separation is necessary to resolve clustered and sparse regions evenly and can be obtained with

$$h(\vec{r_i}) = \eta \left(\frac{m_i}{\rho_i}\right)^{1/3}. \tag{4.27}$$

where η is a parameter specifying the smoothing length in units of the local particle spacing. Equations 4.9 and 4.27 can be solved simultaneously using numerical root-finding algorithms.

Taking into account the gradient of the smoothing length introduces an additional factor

$$\Omega_i \equiv 1 - \frac{\partial h_i}{\partial \rho_i} \sum_{j=1}^{N} m_j \frac{\partial W_{ij}}{\partial h_i}. \tag{4.28}$$

This leads to a full system of equations for ρ, $\vec{v}$ and ϵ

$$\rho_i = \sum_{j=1}^{N} m_j W(|\vec{r}_i - \vec{r_j}|, h_i), \tag{4.29}$$

$$\frac{d\vec{v_i}}{dt} = -\sum_{j=1}^{N} m_j \left(\frac{P_i}{\Omega_i \rho_i^2} + \frac{P_j}{\Omega_j \rho_j^2} \right) \nabla_i W_{ij}, \tag{4.30}$$

$$\frac{d\epsilon_i}{dt} = \frac{P_i}{\Omega_i \rho_i^2} \sum_{j=1}^{N} m_j \left(\vec{v_i} - \vec{v_j} \right) \cdot \nabla_i W_{ij}. \tag{4.31}$$

These are the SPH equivalents to the continuum equations of hydrodynamics.

4.7 Shocks and Artificial Viscosity

Shock fronts are regions of converging flows ($\vec{v}_{ij} \cdot \hat{r}_{ij} < 0$) with very steep and rapid changes in the flow properties. These changes appear as discontinuities. To be able to capture these very steep changes and to avoid particle interpenetration in overdense regions, shocks are artificially broadened across a small number of smoothing lengths. This is done by introducing an artificial viscosity term in the momentum and energy equations.

$$\left(\frac{d\vec{v_i}}{dt} \right)_{\rm VISC} = -\sum_{j=1}^{N} \frac{m_j}{\bar{\rho}_{ij}} \left[\alpha v_{\rm SIG} \vec{v}_{ij} \cdot \hat{r}_{ij} \right] \overline{\nabla_i W}(\vec{r}_{ij}, h_i, h_j) \tag{4.32}$$

$$\left(\frac{d\epsilon_i}{dt} \right)_{\rm VISC} = -\sum_{j=1}^{N} \frac{m_j}{\bar{\rho}_{ij}} \left[\frac{\alpha v_{\rm SIG} (\vec{v}_{ij} \cdot \hat{r}_{ij})^2}{2} \right] \hat{r}_{ij} \cdot \overline{\nabla_i W}(\vec{r}_{ij}, h_i, h_j). \tag{4.33}$$

where $\bar{\rho}_{ij} = (\rho_i + \rho_j)/2$, the coefficient $\alpha \sim 1$, $v_{\rm SIG} = c_i + c_j - 2\vec{v}_{ij} \cdot \hat{r}_{ij}$ is the signal speed, $\hat{r}_{ij} = \vec{r}_{ij}/|\vec{r}_{ij}|$, and

$$\overline{\nabla_i W}(\vec{r}_{ij}, h_i, h_j) = \frac{\nabla_i W(\vec{r}_{ij}, h_i) + \nabla_i W(\vec{r}_{ij}, h_j)}{2}. \tag{4.34}$$

This expression is based on the formulation by Monaghan (1997) and is the default formulation in SEREN (see Hubber et al., 2011, for details).

4.8 Self-Gravity

The gravitational acceleration experienced by particle$i$ due to all other particles is given by

$$\left(\frac{d\vec{v}_i}{dt}\right)_{\text{GRAV}} = \sum_{j=1, j\neq i}^{N} \frac{G m_j (\vec{r}_j - \vec{r}_i)}{|\vec{r}_j - \vec{r}_i|^3}. \tag{4.35}$$

As the SPH density field is continuous, the gravitational force needs to be smoothed in order to be modeled over a continuum and to satisfy Poisson's equation $\nabla^2\Phi = 4\,\pi\,G\,\rho$. This is achieved by introducing the gravitational force kernel ϕ' and the gravitational potential softening kernel ϕ as described in Price & Monaghan (2007). They can be described in terms of the density kernel $W(\vec{r}, h)$.

$$\phi'(\vec{r}, h) = \frac{4\pi}{r^2} \int_0^r W(\vec{r}', h) r'^2 dr', \tag{4.36}$$

$$\phi(\vec{r}, h) = 4\pi \left(-\frac{1}{r} \int_0^r W(\vec{r}', h) r'^2 dr' + \int_0^r W(\vec{r}', h) r' dr' - \int_0^{2h} W(\vec{r}', h) r' dr' \right). \tag{4.37}$$

In the case of adaptive softening lengths, Price & Monaghan (2007) derived an expression for the gravitational acceleration of particle i

$$\left(\frac{d\vec{v}_i}{dt}\right)_{\text{GRAV}} = -G \sum_{j=1}^{N} m_j \overline{\phi'}(\vec{r}_{ij}, h_i, h_j) \hat{r}_{ij} - \frac{G}{2} \sum_{j=1}^{N} \left[\frac{\zeta_i}{\Omega_i} \nabla W_i(\vec{r}_{ij}, h_i) + \frac{\zeta_j}{\Omega_j} \nabla W_i(\vec{r}_{ij}, h_j) \right]. \tag{4.38}$$

where

$$\overline{\phi'}(\vec{r}_{ij}, h_i, h_j) = \frac{\phi'(\vec{r}_{ij}, h_i) + \phi'(\vec{r}_{ij}, h_j)}{2}, \tag{4.39}$$

ζ_i is a quantity defined as

$$\zeta_i = \frac{\partial h_i}{\partial \rho_i} \sum_{j=1}^{N} m_j \frac{\partial \phi}{\partial h}(\vec{r}_{ij}, h_i). \tag{4.40}$$

The gravitational potential at the position of particle i due to all other particles is given by

$$\Phi_i = G \sum_{j=1}^{N} m_j \overline{\phi}(\vec{r}_{ij}, h_i, h_j), \tag{4.41}$$

where

$$\overline{\phi}(\vec{r}_{ij}, h_i, h_j) = \frac{\phi(\vec{r}_{ij}, h_i) + \phi(\vec{r}_{ij}, h_j)}{2}. \tag{4.42}$$

Equation 4.38 contains the kernel softened gravitational acceleration and takes into account the gradient of the smoothing length. This formalism allows one to include self-gravity while insuring exact conservation of momentum and energy.

The time for computing the gravitational accelerations for N particles is of order $\mathcal{O}(N^2)$. The computational time can be reduced to $\mathcal{O}(N \log N)$ using a Barnes-Hut tree (Barnes & Hut, 1986) which allows us to rapidly obtain neighbor lists by decomposing the smallest cubical volume containing all the particles ("the root cell") into eight equal-volume cubic "child cells". The decomposition is repeated for each child cell until each cell only contains just a few particles. For a given particle i, this hierarchical tree structure allows to approximate the gravitational force by looping over a small part of the tree containing the nearest neighbors, while particles in more distant cells can effectively be treated as one point-mass thereby reducing computational expenses.

4.9 Time Integration Scheme

The fluid equations are evolved using a numerical integration scheme. A variety of methods exist to compute the time evolution. For our simulations we use the 2nd-order Leapfrog drift-kick-drift. The position and the velocity are advanced by half a time step but out of phase. Each quantity is updated using the value of the other quantity evaluated at the previous half time step.

$$\vec{r}_i^{\,n+1/2} = \vec{r}_i^{\,n} + \vec{v}_i^{\,n}\frac{\Delta t}{2}, \tag{4.43}$$

$$\vec{v}_i^{\,n+1/2} = \vec{v}_i^{\,n} + \vec{a}_i^{\,n-1/2}\frac{\Delta t}{2}, \tag{4.44}$$

$$u_i^{n+1/2} = u_i^n + \dot{u}_i^{n-1/2}\frac{\Delta t}{2}, \tag{4.45}$$

$$\vec{v}_i^{\,n+1} = \vec{v}_i^{\,n} + \vec{a}_i^{\,n+1/2}\Delta t, \tag{4.46}$$

$$\vec{r}_i^{\,n+1} = \vec{r}_i^{\,n} + \frac{1}{2}(\vec{v}_i^{\,n} + \vec{v}^{\,n+1})\Delta t, \tag{4.47}$$

$$u_i^{n+1} = u_i^n + \dot{u}_i^{n+1/2}\Delta t. \tag{4.48}$$

The optimal time step for a particle i, Δt_i is given by determining the minimum of the time step values given by the particle's acceleration, the Courant condition (Courant et al., 1967) and, if the energy equation is solved explicitly, the heating condition. The time step given by the particle's acceleration $\vec{a}_i$ is given by:

$$\Delta t_{\text{ACCEL}} = \gamma_{\text{ACCEL}}\sqrt{\frac{h_i}{|\vec{a}\,|_i + \eta_a}}, \tag{4.49}$$

where η_a is a small positive acceleration to avoid that the denominator falls to zero. $\gamma_{\rm ACCEL} < 1$ is a constant tolerance factor. The Courant time step is determined by a characteristic length and a characteristic speed. For SPH, these are the smoothing length h_i and the sound speed c_i respectively. SEREN uses a modified Courant condition

$$\Delta t_{\rm COUR} = \gamma_{\rm COUR} \frac{h_i}{(1+1.2\alpha)c_i + (1+1.2\beta)h_i|\nabla \cdot \vec{v}\,|_i}. \tag{4.50}$$

α and β are introduced to account for particles in the vicinity of shocks. The third time step condition is the heating condition, which limits the fractional change in the internal energy per time step

$$\Delta t_{\rm ENERGY} = \gamma_{\rm ENERGY} \frac{u_i}{|du/dt|_i + \eta_e}, \tag{4.51}$$

where η_e is a small positive heating rate to ensure the denominator does not become zero. This time step criterion is only used when the SPH energy equation (Eqn. 4.26) is solved explicitly.

4.10 Sink Particles

Particles in very dense regions have small smoothing lengths thereby reducing the time step dramatically and increasing the total simulation time. To avoid this, Bate et al. (1995) used so called *sink* particles to replace the densest regions. In this method, a region with density ρ above a threshold density $\rho_{\rm SINK}$ is considered to be dominated by gravitational forces. It will undergo collapse and eventually form a star. At the moment of formation, an SPH particle i with $\rho_i > \rho_{\rm SINK}$, along with the $N_{\rm NEIB}$ neighbors within its smoothing region, is replaced by a sink particle. The initial mass of the sink is given by $m_{\rm SINK} = N_{\rm NEIB} m_{\rm PART}$, where $m_{\rm PART}$ is the mass of an SPH particle. The material around the sink is gravitationally attracted by the sink particle. If this material is closer than a certain distance from the sink (called the sink radius) it is accreted by adding its mass and momentum to the sink particle. This however can result in a sharp pressure discontinuity around the sink particle and can lead to overestimated accretion rates. Hubber et al. (2013a) improved the sink algorithm by gradually accreting SPH particles onto a sink over several time steps and by redistributing the angular momentum of the accreted material to the surrounding particles.

Chapter 5

A HEALPix based Momentum Transfer Wind Scheme

In this chapter, we outline the numerical schemes used to model the feedback from a massive star. We introduce the HEALPix algorithm used for modeling both the ionizing radiation and the momentum wind. We briefly review the implemented ionizing radiation scheme and introduce our newly developed scheme for the momentum wind. We then model the impact of the implemented types of feedback on a uniform density distribution.

5.1 Numerical Scheme

The numerical treatment of the transfer of momentum from a source point onto the surrounding medium requires the identification of the impact surface or the momentum receiving area. In their implementation of the transfer of momentum winds, Dale & Bonnell (2008) computed a so-called *working face* which they define as the minimum number of SPH particles required to shield all the particles in the simulation from the wind source and then distribute the stellar wind momentum among these shielding particles. This method requires to loop over all the particles in the simulation. This can be avoided by performing an isotropic search around the wind source and finding the first particle layer directly receiving the momentum flux from the wind source. An algorithm like the Hierarchical Equal Area isoLatitude Pixelization scheme (HEALPix, Górski et al. 2005) presented in the next section, is ideal for the task as it allows us to cast rays in an isotropic manner around a given point source.

Chapter 5 and Chapter 6 are adapted from the article "First Investigation Of The Combined Impact Of Ionizing Radiation And Momentum Winds From A Massive Star On A Self-Gravitating Core" by Judith Ngoumou, David Hubber, James E. Dale and Andreas Burkert submitted to the Astrophysical Journal.

5.1.1 The HEALPix Algorithm

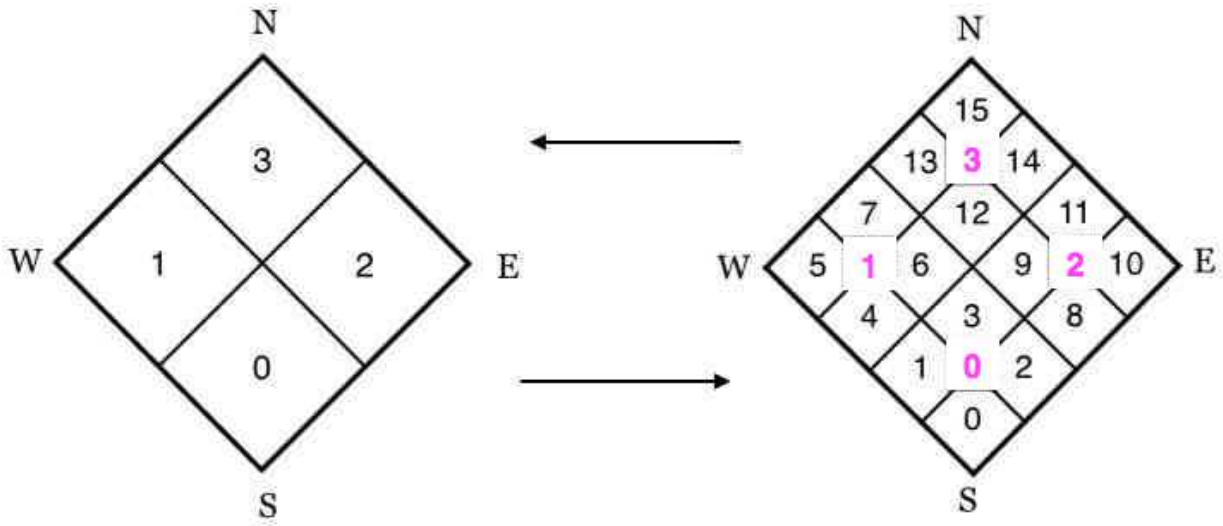

Figure 5.1: Illustration of the NESTED numbering scheme. Four initial rays are split into four child-rays each to increase the angular resolution.

HEALPix is a pixelation algorithm that subdivides a spherical surface into pixels each covering the same surface area . As a "framework for high resolution discretization" (Górski et al., 2005), HEALPix enables us to split the spherical surface surrounding a wind source into discrete elements. This allows us to discretize the wind emitted by the star. HEALPix generates a number $\mathcal{N}_{\text{RAYS}}$ of concentric rays depending on a given level of resolution or refinement l. The spatial distribution of the rays as seen from the central source point is isotropic. The first level of rays ($l = 0$) contains 12 discrete rays. For increased resolution each subsequent level is achieved by splitting the rays into 4 child rays. The number of rays on each level l is given by

$$\mathcal{N}_{\text{RAYS}} = 12 \times 4^l. \tag{5.1}$$

The rays at a given level are equally spaced. The solid angle is given by

$$\begin{aligned} \Delta\Omega_l &= \frac{4\pi}{\mathcal{N}_{\text{RAYS}}} \\ &= \frac{\pi}{3 \times 4^l} \text{ steradians.} \end{aligned} \tag{5.2}$$

Thus the angle between two neighouring rays is

$$\begin{aligned} \Delta\theta_l &\approx (\Delta\Omega_l)^{1/2} \\ &\approx 2^{-l} \text{ radians.} \end{aligned} \tag{5.3}$$

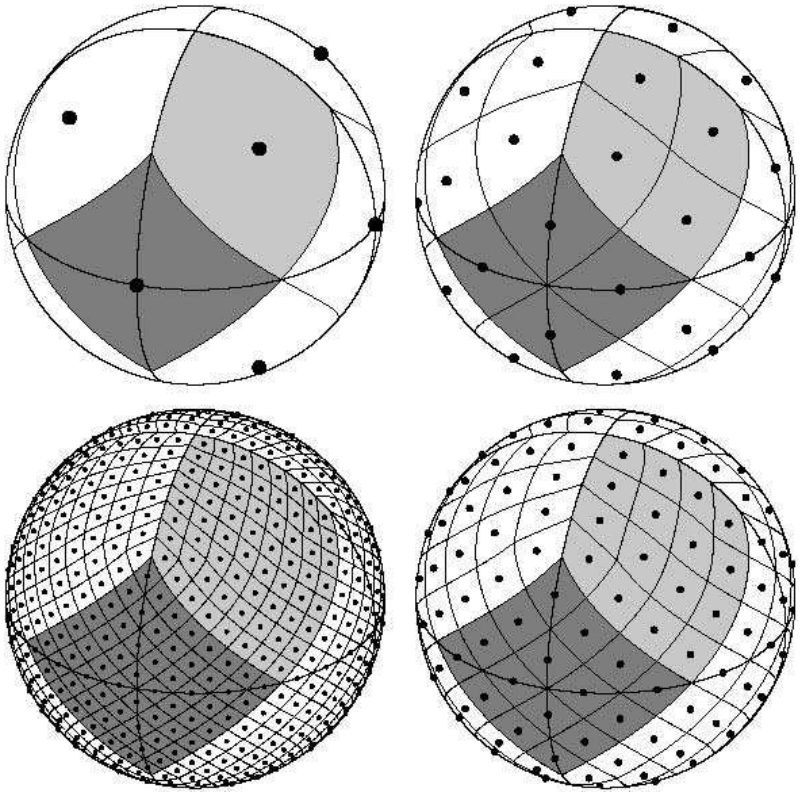

Figure 5.2: Projection of the spherical volume tessellation by the HEALPix algorithm for different resolution levels. The light and dark gray shaded areas indicate the location of two initial base-resolution pixels. Figure from Górski et al. (2005).

When increased angular resolution becomes necessary, the next level $l+1$ is introduced by splitting each ray from the previous level into four child rays. The child rays are identified according to a numbering scheme. We use HEALPix's NESTED scheme (Górski et al., 2005) which follows a quadrilateral hierarchical tree structure (figure 5.1). A parent-ray with an identifier m is split into four child-rays with the IDs m'_i given by

$$m'_i = 4m + i, \qquad \text{with} \quad i = 0, 1, 2, 3, \tag{5.4}$$

where i determines the relative position of the child-rays with respect to the parent-ray. $i = 0$ is the child-ray to the South, $i = 1$ is the child-ray to the West, $i = 2$ is the child-ray to the East, $i = 3$ is the child-ray to the North. Figure 5.2 illustrates the subdivision of a spherical volume by the HEALPix algorithm for the levels $l = 0$ (upper-left), $l = 1$ (upper-right), $l = 2$ (lower-right), $l = 3$ (lower-left). The parent-ray's identifier m can be recovered from the ID of the child-ray m'_i with

$$m = \mathrm{INT}\left(\frac{\mathrm{m'_i}}{4}\right). \tag{5.5}$$

This numbering scheme allows us to easily trace a ray back to the source knowing its ID and the tessellation level.

5.1.2 The Propagation of Ionizing Radiation

We summarize the technique presented by Bisbas et al. (2009) which is used to model the dynamical effects of the ionizing radiation from massive stars. For an arbitrary density distribution $\rho(\vec{r})$, under the assumption of ionization equilibrium and neglecting the diffuse radiation field, we have

$$I_{max} \equiv \int_0^{R_i} \rho(\vec{r})^2 r^2 dr = \frac{\mu^2 \dot{N}_{\rm Lyc}}{4\pi\alpha_B}, \tag{5.6}$$

where $r = 0$ is the position of the star, $r = R_i$ is the position of the ionization front, μ is the mean element mass (mostly H with a contribution of He), α_B is the recombination coefficient defined in section 3.2 and $\dot{N}_{\rm Lyc}$ is the rate at which the star emits ionizing photons [1].

The left-hand side of equation 5.6 is evaluated numerically for a defined set of evaluation points along each HEALPix ray. The positions of an evaluation point is defined with respect to the previous evaluation point (the first one being $j' = 0$ at $r_0 = 0$) using a dimensionless tolerance parameter f_1 of order unity

$$\vec{r}_{j'+1} = \vec{r}_{j'} + f_1 h_{j'} \hat{e}. \tag{5.7}$$

For each evaluation point j the density is estimated using

$$\rho(\vec{r}_j) = \sum_{j=1}^{N} \frac{m_j}{h_j^3} W\left(\frac{|\vec{r}_i - \vec{r}_j|}{h_i}\right). \tag{5.8}$$

The integral in equation 5.6 is then approximated by

$$I(r_j) \equiv \int_0^{r_j} \rho(\vec{r})^2 r^2 dr \tag{5.9}$$

$$\approx \sum_{j'=1}^{j'=j} \left(\frac{\rho_{j'-1} r_{j'-1}^2 + \rho_{j'} r_{j'}^2}{2}\right) f_1 h_{j'-1}. \tag{5.10}$$

We use $f_1 = 0.25$ for all the simulations reported here.

Acceptable resolution is ensured by a splitting criterion and controlled by a dimensionless parameter f_2 which sets the angular resolution of the rays. If $r_j \Delta\theta_l > f_2 h_j$, $\Delta\theta_l$ being the angle between neighboring rays at level l, the ray is split into 4 new child rays. This requires

$$l \geq log_2\left(\frac{r_j}{f_2 h_j}\right). \tag{5.11}$$

[1] Note that if the density field is uniform equation 5.6 we recover the Strömgren radius, equation 3.20

The splitting procedure is repeated for the child rays until the required resolution is reached. To avoid numerical artifacts, the HEALPix rays are rotated through three random angles each time the ray ensemble is cast.

The distance R_i of the ionization front is determined by using a binary chop algorithm between the two evaluation points at r_{j-1} and r_j for which $I(r_{j-1}) < I_{max} < I(r_j)$ up to an accuracy of $\sim 10^{-3} h_{j-1}$. At each evaluation point, the value of the sum in equation 5.10 is calculated if $I(r_j) < I_{max}$, then the evaluation points are within the H II region and their neighbours particles with distance from the star $r < r_j$ are given the temperature T_i. In a layer of thickness $2h_{if}$, h_{if} being the smoothing length of the evaluation point placed on the ionization front at a distance $\vec{r}_{if}$, the temperature is smoothed according to

$$T(r) = 0.5(T_n + T_i) + \frac{r - r_{if}}{2h_{if}}(T_n - T_i),\ |r - r_{if}| < h_{if}. \tag{5.12}$$

This avoids a discontinuous transition in the temperature at the ionization front.

5.1.3 The Transfer of the Wind's Momentum

Assuming that a star located at position $\vec{r}_{\rm STAR}$ is emitting an isotropic mechanical wind at a mass-loss rate $\dot{M}$ and a wind speed $v_{\rm WIND}$. The rate of total (scalar) radial momentum carried by the wind is

$$\dot{p}_{\rm WIND} = \dot{M}\, v_{\rm WIND}. \tag{5.13}$$

We use the HEALPix algorithm to split the spherical surface surrounding the source into discrete, elements which allows us to discretize the wind emitted by the star. At a given time, a ray on level l carries a momentum package given by the momentum rate

$$\dot{p}_l = \frac{\dot{M}\, v_{\rm WIND}}{12 \times 4^l}. \tag{5.14}$$

For each feedback source a linked list of particles sorted by increasing distance from the feedback source is constructed along each ray on the first level. As we walk the HEALPix rays, we find the first SPH particle on the ray with a smoothing length $h_{\rm FIRST}$ at a distance $d_{\rm FIRST} = |\vec{r}_{\rm FIRST} - \vec{r}_{\rm STAR}|$ from the star. We then check if the ray resolution is acceptable, i.e. if the separation between neighboring rays is less than the separation between particles. This is given by a splitting criterion similar to the one described in section 5.1.2 and controlled by the same dimensionless parameter f_2 which sets the angular resolution of the rays. If $d_{\rm FIRST}\Delta\theta_l > f_2 h_{\rm FIRST}$, $\Delta\theta_l$ being the angle between neighboring rays at level l, the ray is split into 4 new child rays. This procedure is repeated for the child rays until the required resolution is reached. We use $f_2 = 0.5$ for all the simulations reported here.

We then walk the list up the ray until we find all SPH particles contained within a distance $|\vec{r}_{\rm FIRST} - \vec{r}_{\rm STAR}| \rightarrow |\vec{r}_{\rm FIRST} - \vec{r}_{\rm STAR}| + 2h_{\rm FIRST}$ of the source. We calculate the acceleration of these particles by distributing the momentum flux belonging to that ray among them. In order to account for the geometric dilution of the wind as the radius

increases, we weight the accelerations given to each particle by r^{-2}. Therefore the rate of change of linear momentum due to the wind for particle i is given by

$$\dot{p}_i = \frac{\dot{M}\, v_{\rm WIND}}{12 \times 4^l} \frac{m_i |\vec{r}_i - \vec{r}_{\rm STAR}|^{-2}}{\sum_{j=1}^{N} m_j \, |\vec{r}_j - \vec{r}_{\rm STAR}|^{-2}}, \tag{5.15}$$

where the summation is over all particles between $|\vec{r}_{\rm FIRST} - \vec{r}_{\rm STAR}|$ and $|\vec{r}_{\rm FIRST} - \vec{r}_{\rm STAR}| + 2h_{\rm FIRST}$ in that ray. The sum is used to normalize the total wind momentum in the selected ray.

From Newton's second law, we get

$$\frac{d}{dt}(p_i) = \frac{dm_i}{dt} v_i + \frac{dv_i}{dt} m_i. \tag{5.16}$$

Therefore, if we assume that the mass of the wind is negligible over the simulation time (i.e. $\frac{dm_i}{dt} \times \Delta t \ll m_i$), then the first term on the right is negligible and the rate of change of momentum is given by

$$\vec{a}_i = \frac{\dot{p}_i}{m_i} \frac{\vec{r}_i - \vec{r}_{\rm STAR}}{|\vec{r}_i - \vec{r}_{\rm STAR}|}. \tag{5.17}$$

5.2 Expansion in a Cold Uniform Medium

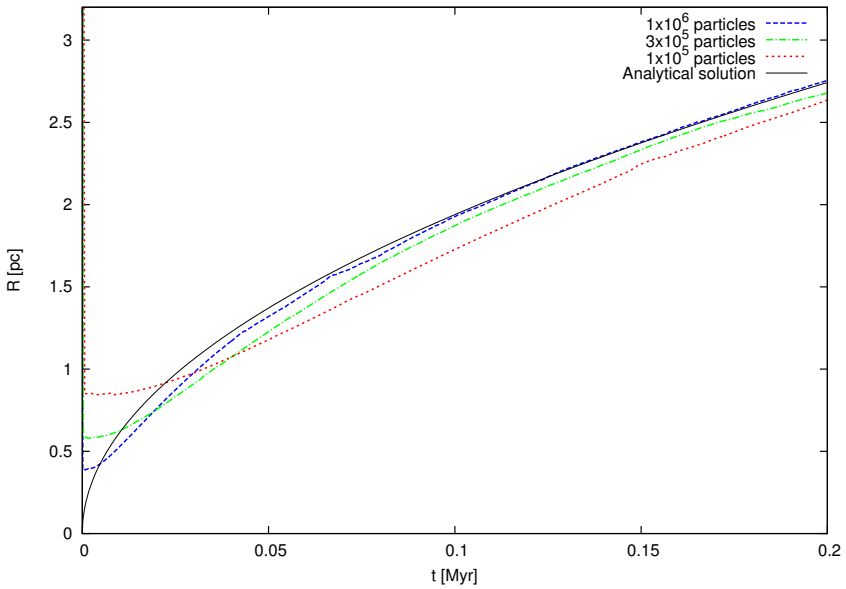

Figure 5.3: Evolution of the wind shell position with time. Comparison between simulations with 1×10^5 (red dotted), 3×10^5 (green dot-dashed) particles and 1×10^6 particles (blue dashed). The black line is the analytical prediction.

In section 3.1 we reviewed the expansion laws for stellar wind bubbles under different assumptions. The case we model here corresponds to the expansion of a bubble with negligible pressure during the momentum conserving snowplow phase. This phase starts when the shocked wind material in the bubble has cooled $\sim 10^4\,\mathrm{K}$. When mixing of wind and nebular material can occur, cooling in the hot interior becomes significant and the wind bubble stays in the momentum conserving phase, for most of the stars main-sequence life.

We performed a set of simulations with 1×10^5 (particle mass $m_{\mathrm{PART}} = 4.13\times10^{-2}\,\mathrm{M}_\odot$), 3×10^5 ($m_{\mathrm{PART}} = 1.4\times10^{-2}\,\mathrm{M}_\odot$), 1×10^6 particles ($m_{\mathrm{PART}} = 4.13\times10^{-3}\,\mathrm{M}_\odot$). Our cloud is modeled as a spherical uniform density cloud of density $n_{\mathrm{c}} = 30\,\mathrm{cm}^{-3}$ and temperature $T = 10$ K. The wind source is located at the center. We used fixed values for the wind mass loss $\dot{M} = 10^{-6}\,\mathrm{M}_\odot\,\mathrm{yr}^{-1}$ and the wind velocity $v_{\mathrm{WIND}} = 2000\,\mathrm{km\,s}^{-1}$. The transfer of momentum leads to the formation of a shock front which expands and sweeps over the material surrounding the source. We used the mean of the positions of the 100 densest particles to identify the position R_{SHELL} of the shock front in our simulations.

In Figure 5.3 we compare the theoretical expansion law with the shock front evolution obtained in our simulations. The inaccuracies seen at the beginning are related to the initial smoothing length h since we smooth the momentum over $2h$ as described in section 5.1.3. With increasing resolution the shock front expansion converges towards the analytical solution. Runs with more than 3×10^5 particles are in good agreement with the analytical expectation. Unlike the ionization scheme from Bisbas et al. (2009), the momentum wind implementation does not require additional temperature smoothing and thus is a robust representation of the physics involved.

5.3 Impact of the Wind Momentum Transfer on an Ionized Uniform Cloud

In order to assess the impact of the wind on the surroundings of the star, the momentum transfer scheme was applied to a uniform density cloud, $n_{\mathrm{c}} \approx 30\,\mathrm{cm}^{-3}$. We used fixed values for the wind mass loss $\dot{M} = 10^{-6}\,\mathrm{M}_\odot\,\mathrm{yr}^{-1}$, the wind velocity $v_{\mathrm{WIND}} = 2000\,\mathrm{km\,s}^{-1}$ and the ionizing photon rate $N_{\mathrm{Lyc}} = 10^{49}\,\mathrm{s}^{-1}$. These are values close to those for an O7.5 star as listed by Smith (2006). The effects of ionizing radiation are included using the HEALPix based ionizing radiation scheme developed in Bisbas et al., 2009. The results are compared for these three cases of stellar feedback in Fig. 5.4.

Figure 5.5 shows the radial density profile at $t = 0.35\,\mathrm{Myr}$ for the wind-only simulation (black), the ionization-only case (red) and the combined feedback case (green). In a cold uniform medium, the momentum transfer from a single stellar wind creates an expanding shock front (black dots). Compared to the cases including the ionizing radiation, the wind-only shock front is always behind and the maximum density in the shocked region is a factor ~ 3 lower than in the cases with ionization. In the combined feedback case (green dots), the wind's impact on warm ionized material is significantly reduced. The pressure

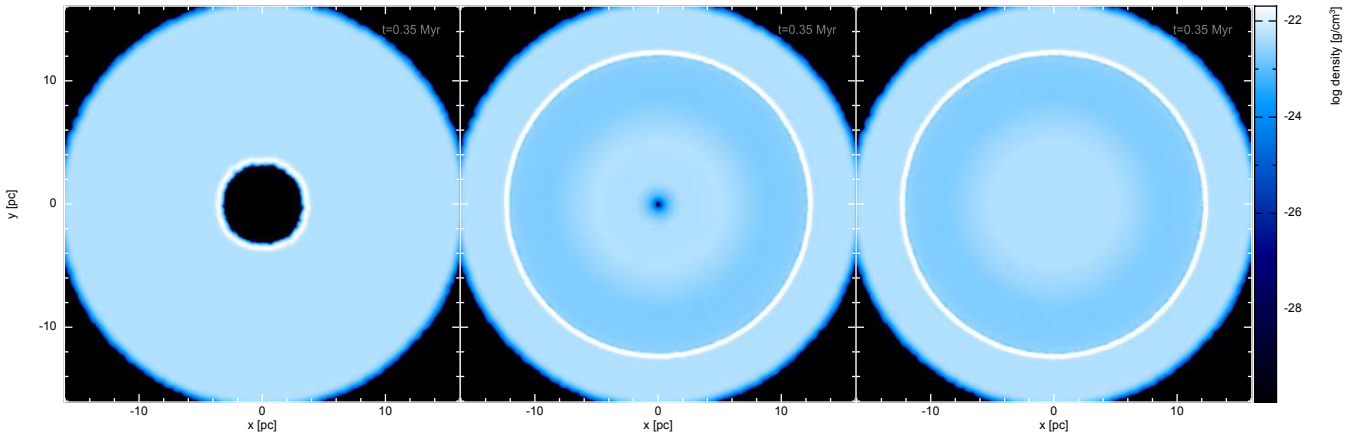

Figure 5.4: Density slice through a column density plot showing the shell expansion in a uniform density medium at the same time $t = 0.35$ Myr for three feedback mechanisms. left: momentum transfer only, middle: momentum transfer and ionizing radiation, right: ionizing feedback only.

in the 10^4 K environment is high enough to decelerate the front until it reaches the sound speed in the ionized gas and a quasi equilibrium is attained as the ram pressure equals the thermal pressure in the ionized gas. A nearly stable configuration is achieved with just the innermost ~ 1 pc affected by the momentum wind.

The position of the ionization front is quite similar in the ionization-only run and the dual feedback run, with the ionization-only run reaching slightly higher densities at the front position. The cold material, outside the dense shell, does not feel the impact of the momentum input. Figure 5.5 also shows the rarefaction wave behind the isothermal shock front which is remarkably similar in both runs with and without winds but including ionization. These first test simulations already demonstrate the limited effects of wind-blown bubbles on the surroundings compared with ionization.

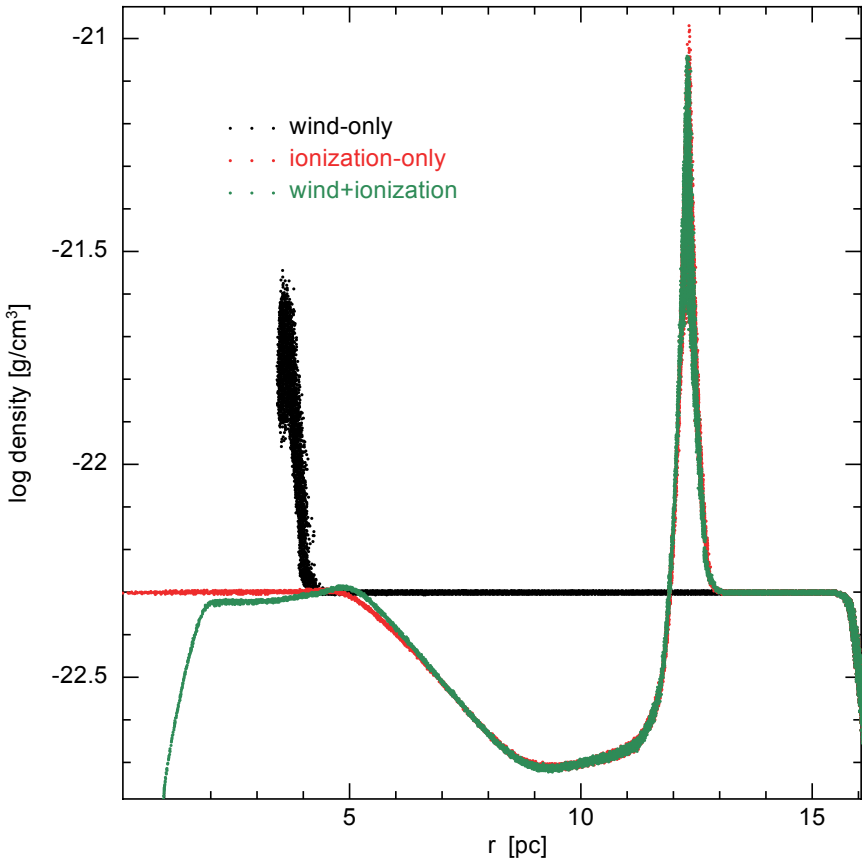

Figure 5.5: Density over radial distance r from the feedback source for the wind-only simulation (black dots), the ionization-only simulation (red dots) and the combined feedback case (green dots).

Chapter 6

Effect of Feedback on a Self-Gravitating Core

Here, we study the impact of the feedback from a massive star on a self gravitating sphere. We compare the combined effect of the momentum transfer and the ionizing radiation to the impact of each of these feedback mechanisms acting alone.

6.1 Initial Conditions

We apply our numerical scheme to a self-gravitating core. We assume a dense core excavated from its molecular environment which finds itself exposed to the feedback from a nearby massive star. The core is modeled as a subcritical isothermal Bonnor-Ebert sphere (BES) profile with a dimensionless boundary radius $\xi_B = 4.0$ (e.g. Burkert & Alves, 2009). The temperature of the core is $T = 10\,\mathrm{K}$ and the isothermal sound speed is $c_s = 0.2\,\mathrm{km\,s^{-1}}$. Its mass is set to $M_{\mathrm{CORE}} = 4\,\mathrm{M_\odot}$. The initial central number density is $n_0 = 6 \times 10^3\,\mathrm{cm^{-3}}$ and the core radius amounts to $R_{\mathrm{CORE}} = 0.25\,\mathrm{pc}$. The BES is embedded in a cold uniform density medium ($T = 10\,\mathrm{K}$ and $n_{\mathrm{MED}} = 0.05\,\mathrm{cm^{-3}}$).

We use a barotropic equation of state:

$$P = c_s^2 \rho \left\{ 1 + \left(\frac{\rho}{\rho_{\mathrm{CRIT}}} \right)^{\gamma - 1} \right\}, \tag{6.1}$$

where P is the thermal pressure of the gas, ρ is the gas density, $\rho_{\mathrm{CRIT}} = 10^{-13}\,\mathrm{g\,cm^{-3}}$ is the critical density above which the gas becomes approximately adiabatic, $c_s = 0.2\,\mathrm{km\,s^{-1}}$ for molecular hydrogen at $T = 10\,\mathrm{K}$ and $\gamma = 5/3$ is the ratio of specific heats. This value of γ is justified as we treat $T = 10\,K$ where the rotational degrees of freedom for H_2 are not highly excited. Local density peaks with $\rho_{\mathrm{PEAK}} > \rho_{\mathrm{SINK}} = 10^{-11}\,\mathrm{g\,cm^{-3}}$ are replaced by sink particles which then accrete mass using the newly developed algorithm of Hubber et al. (2013a) which regulates the accretion of matter onto a sink and redistributes the angular momentum of the accreted material to the surrounding gas. We use 5×10^5 particles to model the BES, resulting in a particle mass $m_{\mathrm{PART}} = 8 \times 10^{-6}\,\mathrm{M_\odot}$. The minimum

Jeans mass corresponding to a critical density $\rho_{\rm CRIT} = 10^{-13}\,{\rm g\,cm^{-3}}$ at a temperature $T = 10\,{\rm K}$ is $M_J = 3 \times 10^{-3}\,{\rm M_\odot}$ and is therefore always resolved (Bate & Burkert, 1997), as $2m_{\rm PART}N_{\rm NEIGH} = 8 \times 10^{-4}\,{\rm M_\odot}$ and $N_{\rm NEIGH} = 50$ being the number of SPH neighbors. The core is then exposed to three different types of feedback from a source placed at a distance of $d_s = 3\,{\rm pc}$ from the core center.

6.2 Momentum Winds only

To examine the impact of the momentum transfer on the core, we used our fiducial values for the stellar mass loss rate $\dot{M}_{\rm WIND} = 10^{-6}\,{\rm M_\odot\,yr^{-1}}$ and the wind terminal velocity $v_{\rm WIND} = 2000\,{\rm km\,s^{-1}}$. Fig. 6.1 shows a time sequence of the evolution of the core. The cold material is slowly ablated from the front side of the core and redirected to the sides. The material at the back, which is shielded from the wind, expands into the lower pressure environment. Over time the front material at intermediate densities is slowly compressed. However the wind has very little effect on the densest inner region of the core. The extra compression is not enough to induce gravitational collapse. After $\sim 1\,{\rm Myr}$, which also corresponds to the free fall time in the center, the densest material starts to be dispersed by the expansion of the core which then quickly dissolves.

Both the dispersive and the compressive effects are illustrated in Fig. 6.2, which shows a two dimensional histogram comparing the density in the fiducial wind simulation (y-axis) and the density in the no-feedback case (x-axis) at $t = 1.2\,{\rm Myr}$, when the highest density is reached in the center. The black dotted line shows equal densities. It represents gas whose density is not affected by feedback. Filled histogram bins above it represent material that has an increased density in the wind-only run, while those below represent material which has a lower density compared to the no-feedback run. Fig. 6.2 shows that the momentum transfer mostly affects the low and intermediate density material at the front edge of the core. The largest spread around the $x = y$ line is seen for densities between 10^{-24} and $10^{-21}\,{\rm g\,cm^{-3}}$. Most of the mass is above the line indicating the compressive effect of the wind. A slight density increase can also be seen for higher densities $\geq 10^{-21}\,{\rm g\,cm^{-3}}$ but the impact of the wind is rather modest.

6.3 Combining the Wind Momentum Transfer and the Ionizing Radiation

We now look at the combined effects of the ionizing radiation *and* the momentum wind from our fiducial feedback source on our BES. The values for the stellar mass loss and the terminal wind velocity are the same as above. The ionizing photon rate is set to $\dot{N}_{\rm LyC} = 10^{49}\,{\rm s^{-1}}$. The core is located well within the source's initial Strömgren-radius and finds itself embedded in a warm ($T = 10^4\,{\rm K}$) environment.

Figure 6.3 shows a time sequence of column density plots for the evolution of the core under the impact of the combined feedback mechanisms. The ionization front compresses

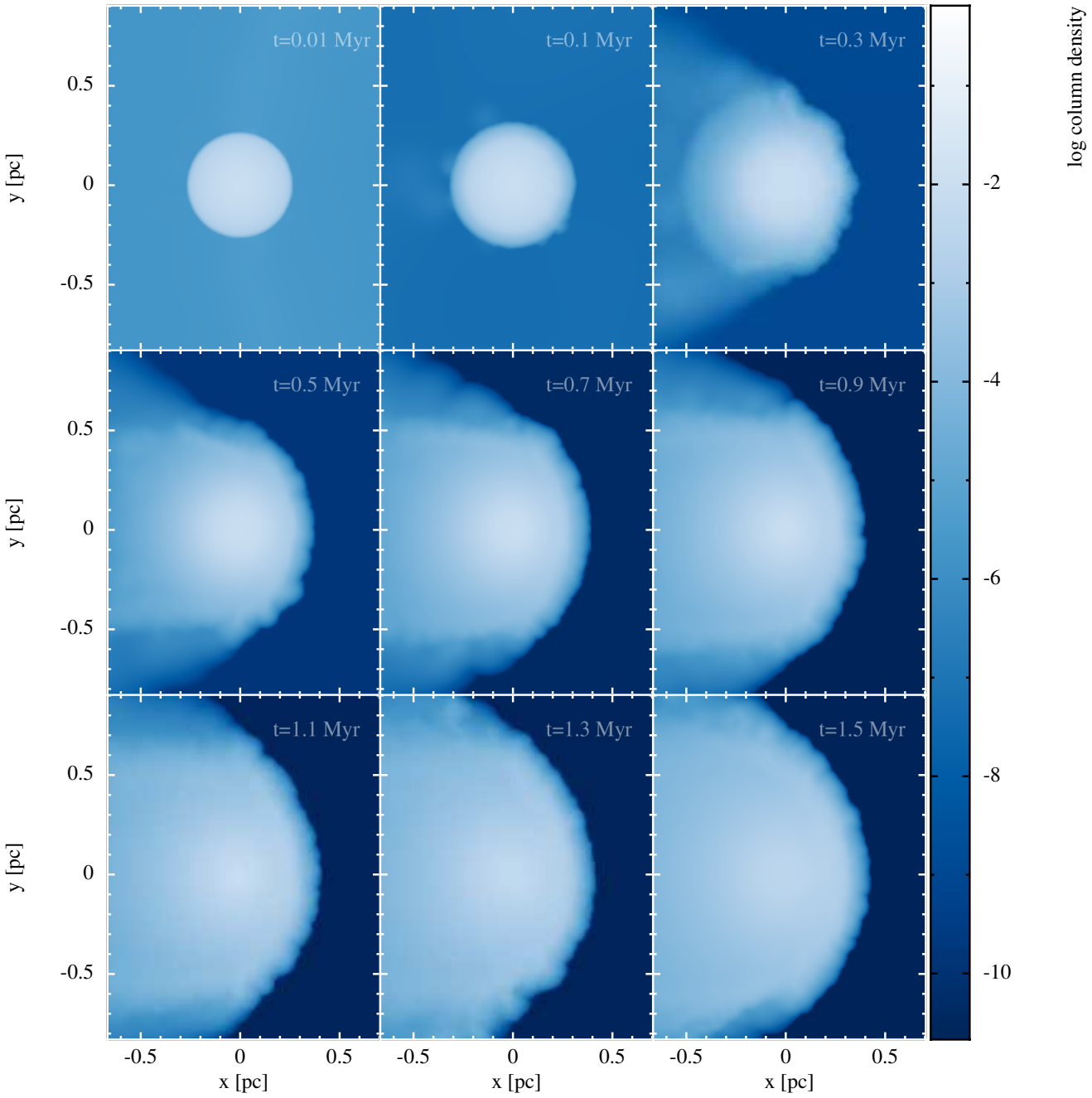

Figure 6.1: Time evolution of the impact of the momentum transfer on a cold core. The color bar represents the integrated density along the z-axis in g/cm^2.

the illuminated front of the core while the sides are compressed by the pressurized ambient medium. The material at the edge is photo-evaporated. The back of the core is initially shielded from the ionizing radiation by the denser core but is quickly filled by low density

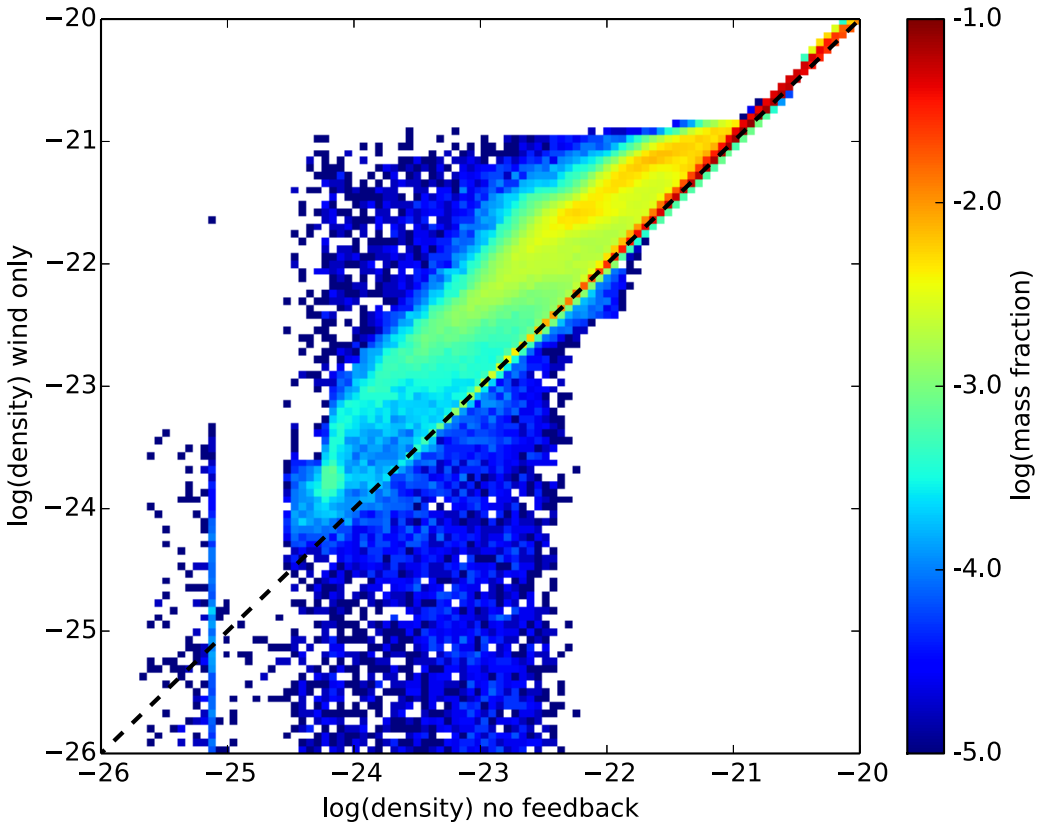

Figure 6.2: 2D-histogram for the density distribution in the winds-only (y-axis) case and for the case without feedback (x-axis) at $t = 1.2$ Myr. The color bar shows the mass contained in the bins. The black dotted line represents the points where the density in the two runs are the same.

ionized gas from the side. The momentum transfer through the evaporation of the illuminated front is strong enough to displace the whole core; the initial center of the core is pushed in the negative x-direction. After ~ 0.05Myrs, the swept-up shell becomes massive enough and contracts laterally due to its self-gravity. Through the combined effect of the movement in x-direction and the contraction towards the densest part on the axis of symmetry of the core, the initially spherical core is stretched in the x-direction, compressed in the y and z-directions and forms a dense elongated structure. The densest region of the filament collapses to form a sink particle. Similar to the low ionizing flux runs described in Bisbas et al. (2009), star formation first appears ahead of the ionizing front towards the center of the core.

In Figure 6.4 we compare the combined feedback run (left panel) with the ionization-only run (right panel) at a time just after sink formation. The left panel, corresponding to the dual-feedback run, is at a slightly later time than the right panel indicating that the

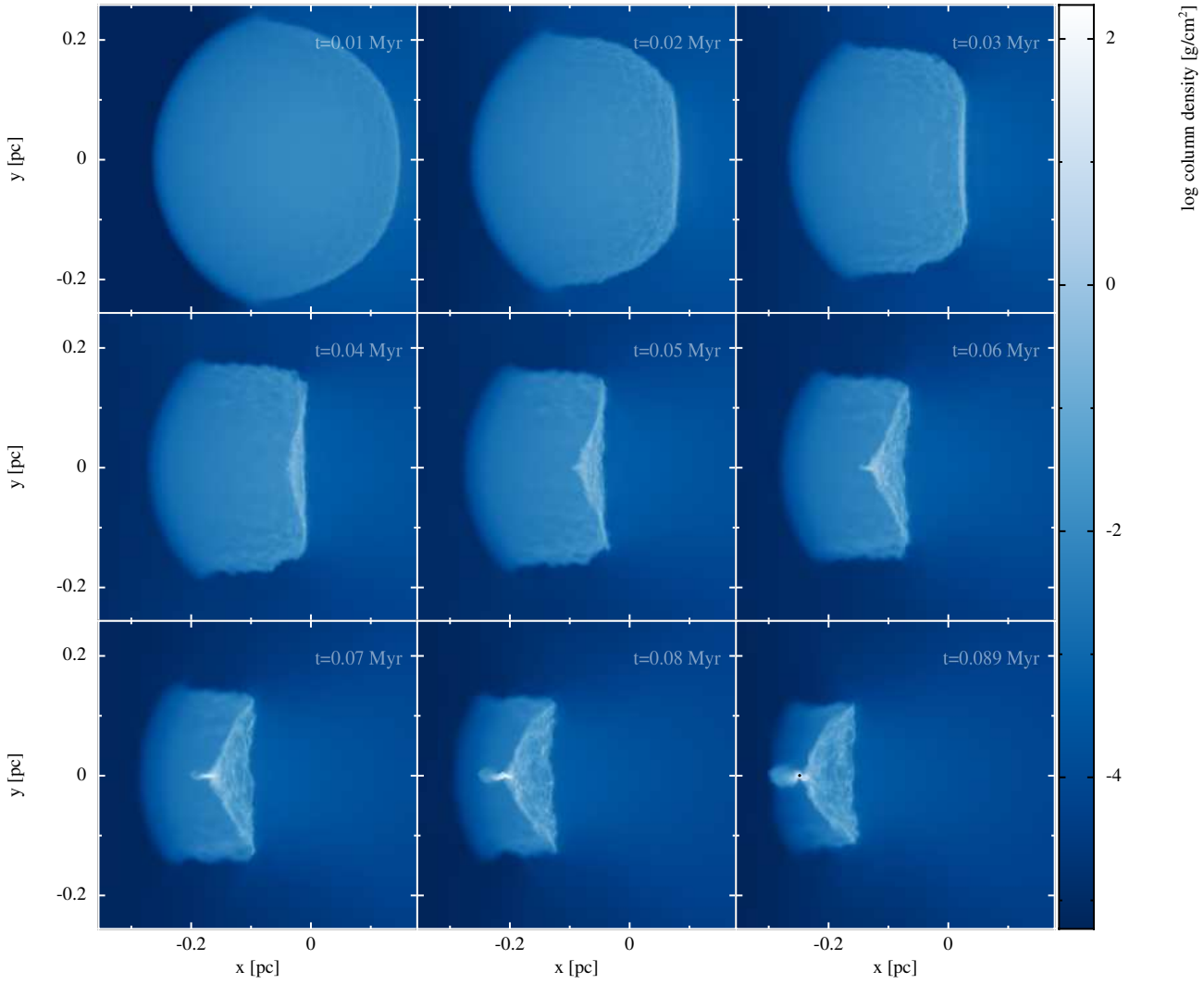

Figure 6.3: Time evolution of the combined impact of the momentum transfer and the ionizing radiation on a cold core. The color bar represents the integrated density along the z-axis in g/cm^2.

addition of the momentum wind leads to a small delay in sink particle formation. The first sink particle is formed after $\sim 0.086\,\mathrm{Myr}$ in the dual-feedback case, a bit later than in the ionization-only run where the first sink appears at $\sim 0.073\,\mathrm{Myr}$. The overall appearance of the core however is quite similar in both cases.

Figure 6.5 shows the 2D-histogram of particle densities ρ_{DUAL} (x-axis) and ρ_{ION} (y-axis) in the wind and ionization simulation and the ionization-only simulation respectively. It shows the distribution of particles in density space at $t = 0.07$ Myr, a time just before sink formation in the ionization-only case. Most of the particles have densities around $\sim 10^{-18}\,\mathrm{g\,cm^{-3}}$. They are part of the dense filament and the shell like structure at the

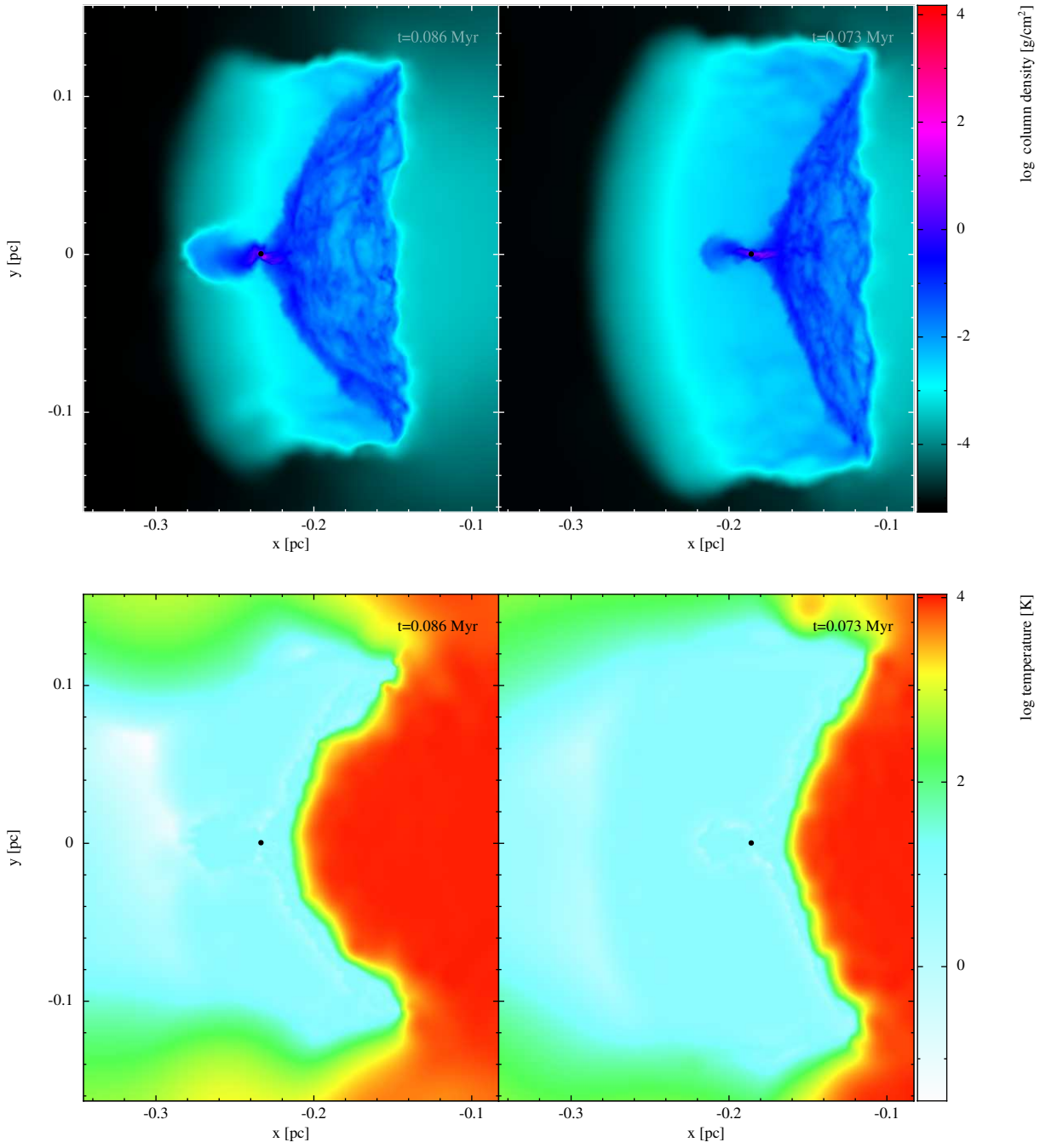

Figure 6.4: Snapshot of the column density (top row) and of the temperature in a slab through the center of cold gas core (bottom row) for the momentum wind and ionizing radiation case (left panel) and for the ionizing radiation only case (right panel). The sink particles are represented by black dots.

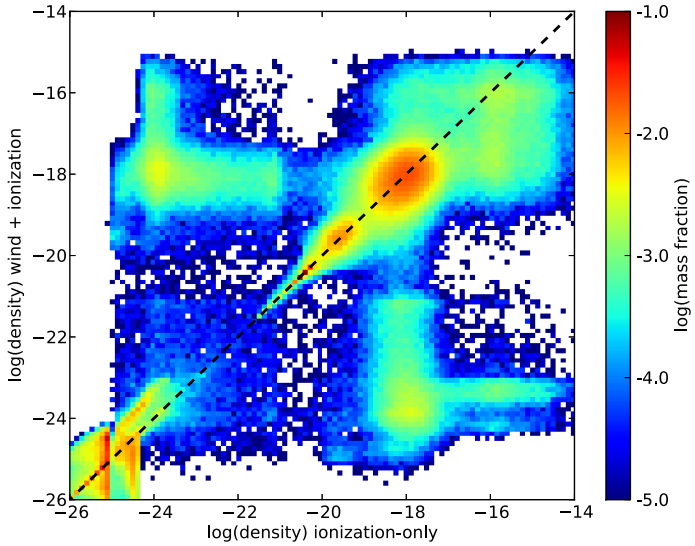

Figure 6.5: 2D-histogram for the density distribution in the wind and ionization case (y-axis) case and for the case with ionization only (x-axis) at $t = 0.07$ Myr. The color bar shows the mass contained in the bins. The black dotted line represents the points where the density in the two runs are the same.

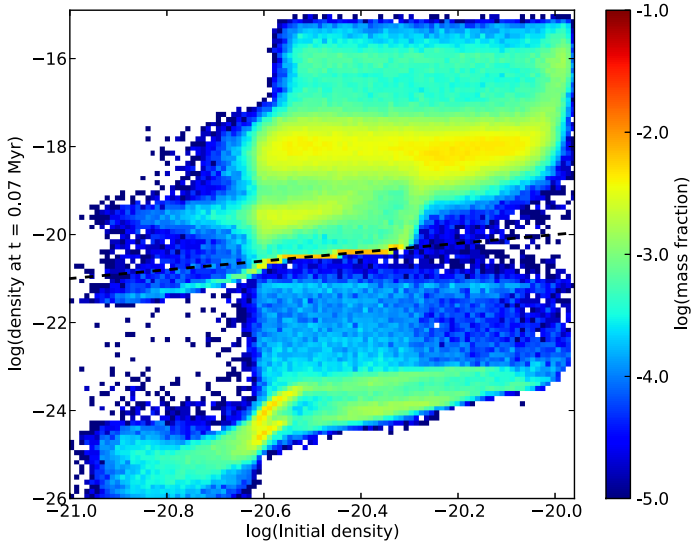

Figure 6.6: Two-dimensional histogram for the fiducial O7.5 star showing the densities at $t = 0.07$ Myr on the vertical axis as a function of the initial densities of the core. The colorbar shows the mass contained in the bins.

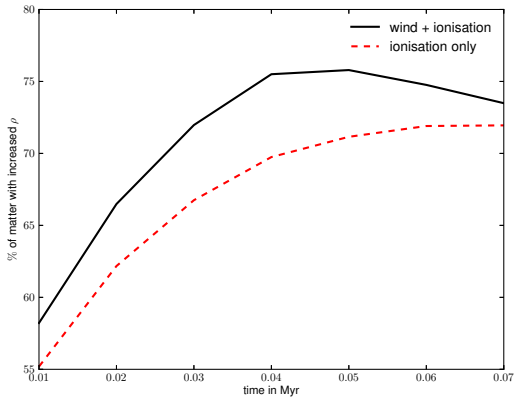

Figure 6.7: Percentage of particles with increased density since t_0 for the wind and ionization case (solid black line) and the ionization-only case (dashed red line) as a function of time.

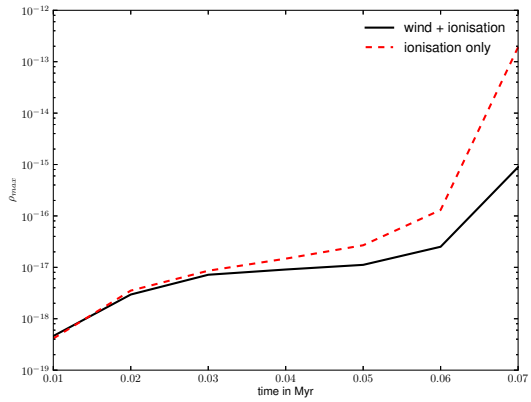

Figure 6.8: Time evolution of the maximum of the density of the ionized self gravitating core for the fiducial feedback values. Ionizing radiation only (dashed red); momentum wind and ionizing radiation (solid black).

front edge of the core. The distribution in the histogram appears almost symmetric around the black dotted line. This shows that the density distribution is very similar in both simulations but the particles contributing to the different density phases are partly different. The area above the black dotted line shows gas with $\rho_{\mathrm{DUAL}} > \rho_{\mathrm{ION}}$, for which the momentum wind lead to an increase in density while the area below indicates gas with $\rho_{\mathrm{DUAL}} < \rho_{\mathrm{ION}}$. This shows the dual impact of the momentum wind. It both compresses and disperses the gas. In the present case both effects almost cancel each other out, but not quite, leading to delayed star formation in the dual-feedback simulation.

In Figure 6.6 we compare the densities at $t = 0.07\,\mathrm{Myr}$ to the initial densities of the same material in the core. Approximately 73% of the particles have a higher density at $t = 0.07\,\mathrm{Myr}$ in the combined-feedback run for 71% in the ionization-only case. However, 49% of the particles have a higher density in the combined-feedback run than in the corresponding ionization run. Although in the dual-feedback run slightly more gas has increased its density since t_0 (Figure 6.7), the ionization run appears to have the highest densities (see Figure 6.8).

6.3.1 Impact of a B0 Star

To study the impact of a fainter massive star, we expose the core to the ionizing radiation and the wind momentum from a B0 star with much weaker winds. We adopt values from Smith (2006) in his census of the massive star in the Carina Nebula. We use $\dot{M}_{\mathrm{WIND}} = 3 \times 10^{-7}\,\mathrm{M}_{\odot}\,\mathrm{yr}^{-1}$ and $v_{\mathrm{WIND}} = 1180\,\mathrm{km\,s}^{-1}$ for the mass loss rate and the terminal wind velocity and an ionizing photon rate of $\dot{N}_{\mathrm{LyC}} = 1.9 \times 10^{48}\,\mathrm{s}^{-1}$.

The ionization front advances slower than in our fiducial case. The front appears more

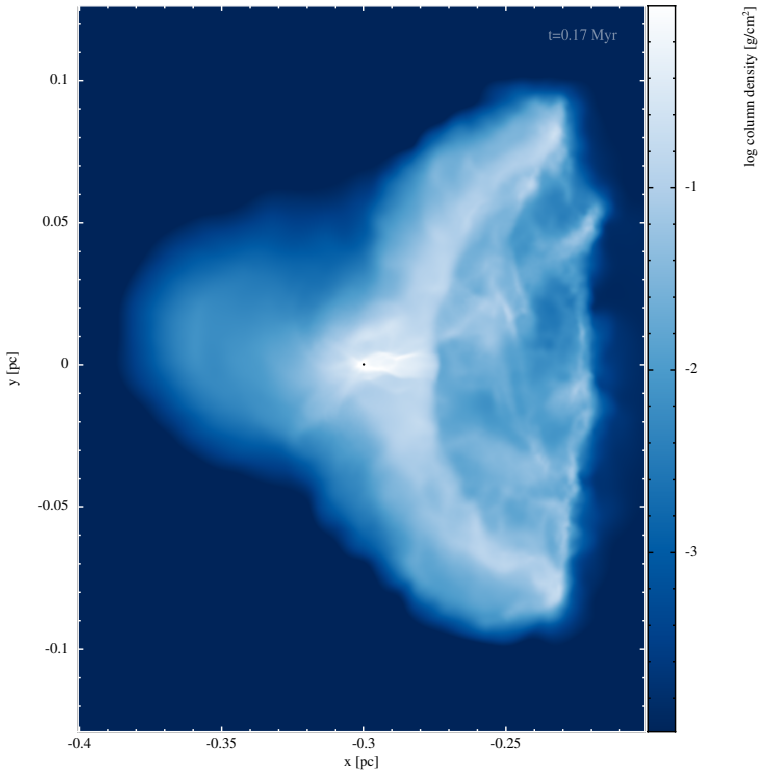

Figure 6.9: Snapshot of the column density showing the combined impact of the wind and ionizing radiation from a B0 like star at time just after sink formation.

extended and fuzzy (see Figure 6.9). A similar behavior to the fiducial case is observed. The material is swept up in a dense front that contracts and collapses towards the symmetry axis. The morphology of the core resembles the concave shape (with respect to the feedback source) described in the O7.5-star case. The first sink particle is formed significantly later than in our fiducial case, at $t_* \approx 0.17\,\mathrm{Myr}$ in the dual feedback run and at $t_* \approx 0.18\,\mathrm{Myr}$ in the ionization-only run. In this case the momentum wind leads to slightly earlier star formation.

6.3.2 Impact of an O3 Star

We also selected a more powerful source at the upper end of the massive star range. We use values from Smith (2006) for an O3 star with a mass loss rate, a terminal wind velocity and ionizing photon rate of $\dot{M}_{\mathrm{WIND}} = 1.3 \times 10^{-5}\,\mathrm{M}_\odot\,\mathrm{yr}^{-1}$, $v_{\mathrm{WIND}} = 3160\,\mathrm{km\,s}^{-1}$ and $\dot{N}_{\mathrm{LyC}} = 6 \times 10^{49}\,\mathrm{s}^{-1}$.

The evolution of the morphology of the core in this case differs from the ones we obtain with the less massive stars. Instead of the concave form described above, the core evolves into a convex shape (see Figure 6.10). The front is being accelerated inside the core and the less dense structures have a higher velocity than the denser ones along the symmetry

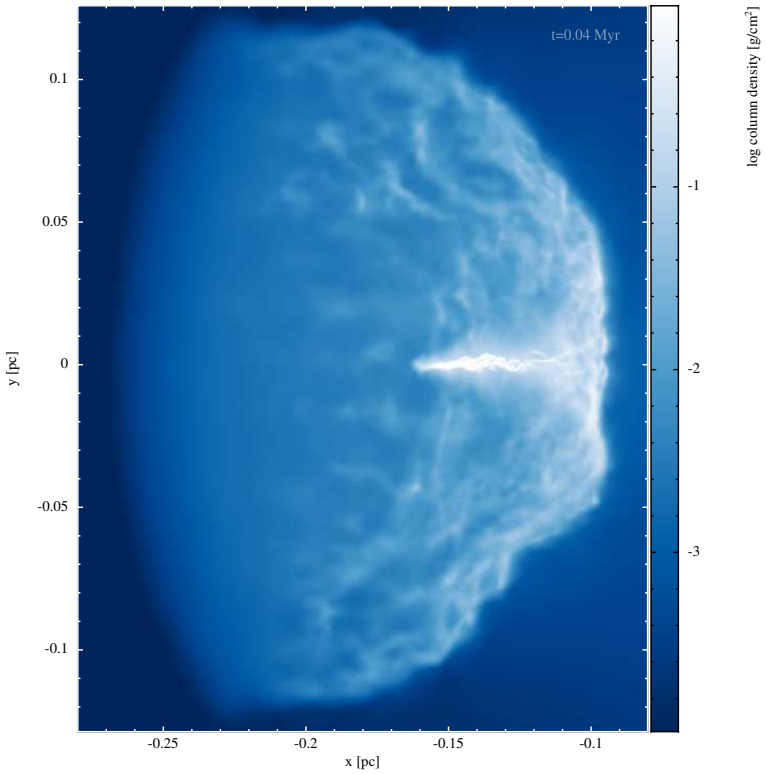

Figure 6.10: Snapshot of the column density showing the combined impact of the wind and ionizing radiation from a O3 like star at a time of greatest compression.

axis. The material converges towards the symmetry axis due to the combined influence of the front expansion and the self-gravity. A central filament forms but the material is evaporated, ionized and dispersed before it can fragment. No sink particle is formed.

Chapter 7

The Impact of Feedback on a Turbulent Cloud

In this section we take a look at the impact of an external stellar feedback source on a structured and turbulent cloud. Dale et al. (2007) and Gritschneder et al. (2009); Gritschneder et al. (2010) have studied the impact of the photoionization from a source located outside a molecular cloud. They found that ionization effectively heats cold low-density gas that it enhances overdensities seeded by the initial turbulence. The side of the cloud facing the source was compressed and molded into filamentary and pillar-like structures. In the following sections, we take a look at the combined impact of the ionizing radiation and the momentum wind from our fiducial O7.5 star as described in section 5.3 on a turbulent and structured cloud. We use a similar approach as the one described in Gritschneder et al. (2009).

7.1 Initial Conditions

We start with a cube of gas with 4 pc in side length at a temperature of $T = 10\,\mathrm{K}$ and a mean number density of $n = 200\,\mathrm{cm}^{-3}$. The gas mass in the box is $300\,\mathrm{M}_\odot$. To mimic initial Burgers turbulence (see section 1.2.3) we use the prescription for decaying turbulence described in Mac Low et al. (1999). We set up a supersonic turbulent velocity field (Mach 10) with a power-law $E(k) \propto k^{-2}$ in k-space, where only the largest modes $k = 1 \ldots 4$ are populated. This is just the Fourier transform of a step function which is used as a description for shocks. This setup is allowed to decay freely under the influence of isothermal hydrodynamics and artificial viscosity. We let the turbulence in our box decay until the root mean square (rms) velocity has reached $\sim 1\,\mathrm{km/s}$ which corresponds to a Mach number of 5. The cloud is initially bound, i.e. it is massive enough to be held together by its own gravity, as the virial ratio $E_{kin}/E_{pot} = 0.8$.

We use the Mach 5 box as our initial density field for our simulations. We include self-gravity and the feedback from our fiducial O7 star placed at a distance of 6 pc away from the cloud, in the negative x-direction. We use periodic boundary conditions in the y

and z-direction and open boundaries in the x-direction. This configuration mimics a larger sheet-like structure with flows of material in the y and z-directions.

This setup, which is very similar to the one presented in Gritschneder et al. (2009), is used as initial condition for the simulations described in this Chapter.

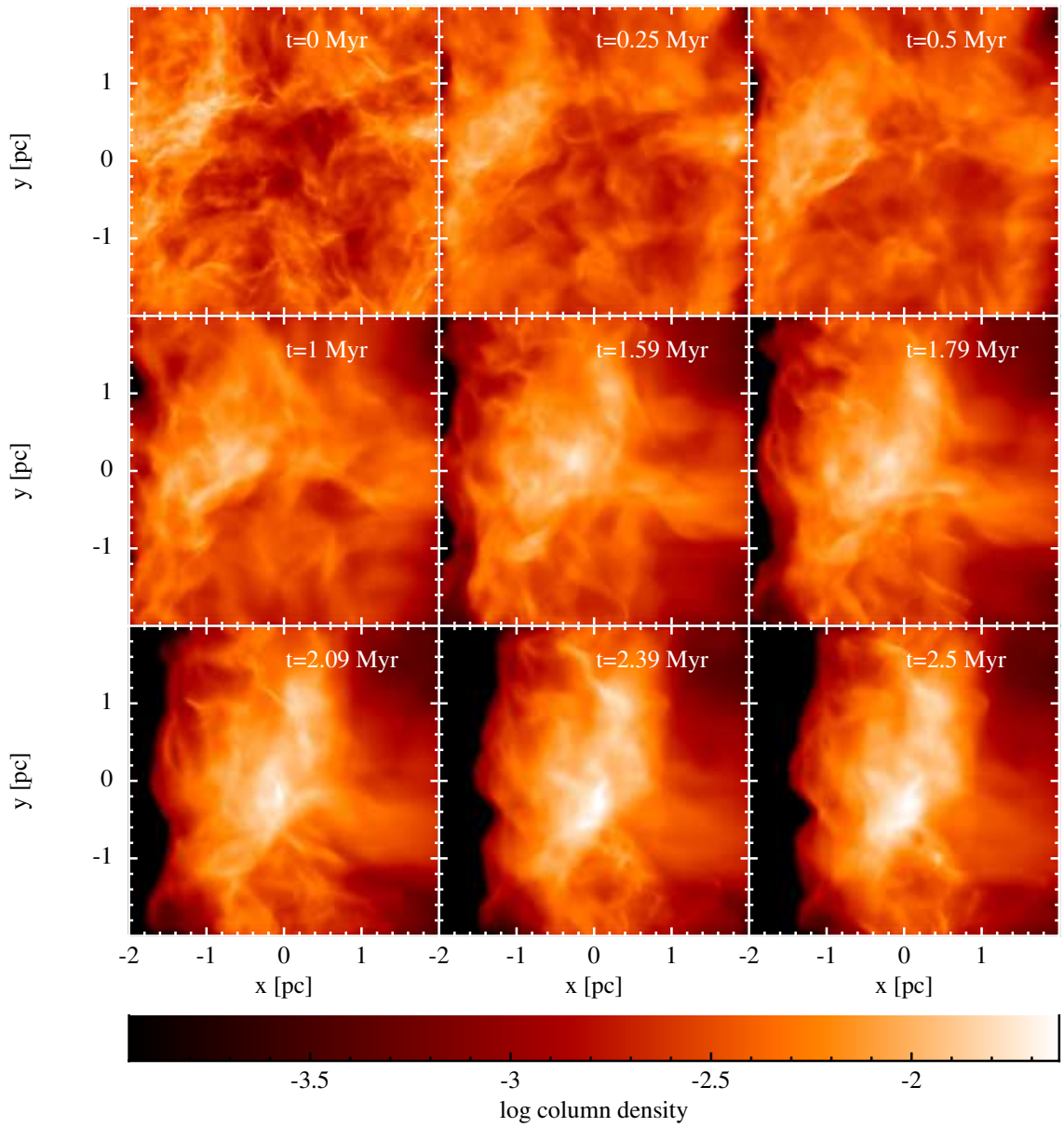

Figure 7.1: Evolution of a turbulent cloud affected by the wind from an external stellar source located left of the cloud, at 6 pc in the negative x-direction.

7.2 Momentum Winds only

We switch on the momentum wind and let the cloud evolve under the influence of its own gravity. Figure 7.1 shows the time evolution of the turbulent cloud. For a source with a mass loss rate of $\dot{M} = 10^{-6}\,\mathrm{M}_{\odot}\,\mathrm{yr}^{-1}$, a terminal wind velocity $v_{\mathrm{WIND}} = 2000\,\mathrm{km\,s}^{-1}$ placed at 6 pc, the transfer of momentum leads to an acceleration of $\sim 10^{-10}\,\mathrm{km\,s}^{-2}$ for an SPH particle at the edge of the cloud. This translates into a increase in velocity v_x of $\Delta v_x \approx 4\,\mathrm{kms}^{-1}$ after $\Delta t = 1000\,\mathrm{yr}$. Over time the side facing the source is slowly pushed in the positive x-direction. At the same time on the opposite site the gas is able to stream out of the cloud. The winds have a compressive effect on the low to mid density

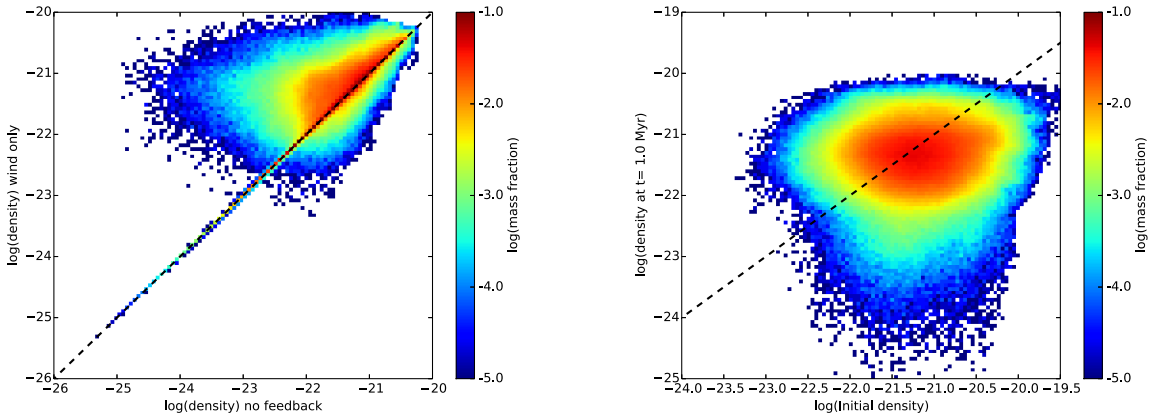

(a) (b)

Figure 7.2: Density histograms comparing: (a) the wind-only simulation (y-axis) to the control simulation (x-axis) $t = 1.0\,\mathrm{Myr}$ (b) and the density at $t = 1.0\,\mathrm{Myr}$ over densities of the initial conditions.

gas $\rho \leq 10^{-21}\,\mathrm{g\,cm}^{-3}$. In comparison to the control simulation without feedback, most particles have a higher density in the wind simulation. Overall, after 1 Myr most of the gas has a reduced density. The structures in the winds-only simulation appear very smoothed out and resemble those in the control case with no feedback.

7.3 Impact of Ionizing Radiation and Winds

In the following we look at the combined impact of the ionizing radiation and the momentum wind on our turbulent cloud.

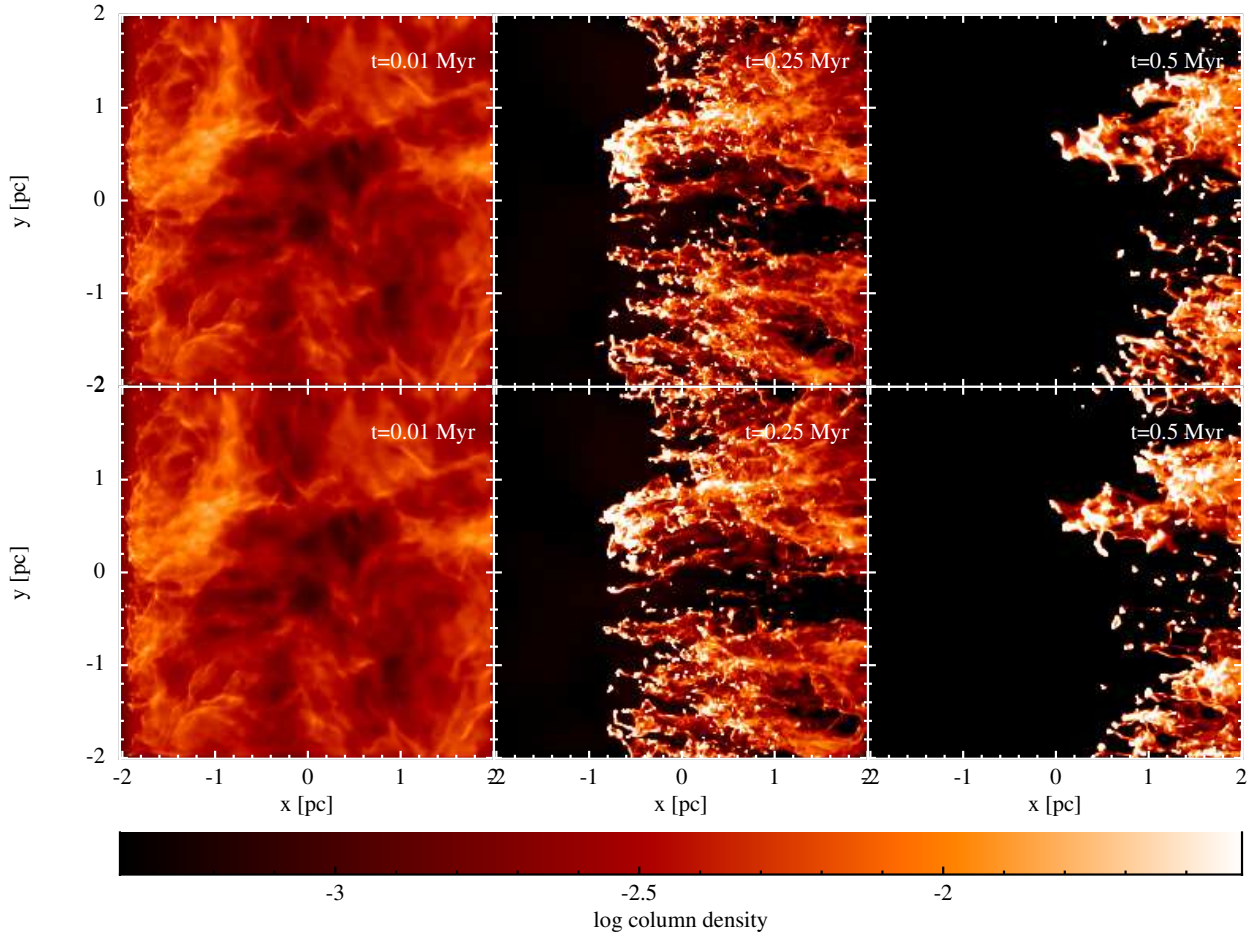

Figure 7.3: Evolution of turbulent cloud affected by the impinging feedback from the left. The top row shows the wind+ionization case. The second row is the ionization only case.

With our fiducial O7.5 star placed 6 pc away from the cloud, in the negative x-direction, the photon flux per time reaching the cloud's edge at -2 pc is $F_{Ly} \approx 5 \times 10^9$ photons cm^{-2} s^{-1}. This allows for an instantaneous ionization of about a third of our box. Due to the higher pressure in the ionized gas, the cold gas is effectively pushed away from the source in x-direction. Figure 7.3 compares the column densities in z-direction at $t = 0.1$ Myr, $t = 0.25$ Myr, $t = 0.5$ Myr for the case wind and ionization case (top row) and the ionization only case (bottom row). Figure 7.4 shows the snapshots at $t = 0.25$ Myr of the column density in y-direction (middle panel) and in x-direction. The evolution of the cloud is remarkably similar in both feedback cases.

The radiation penetrates further along the low density channels, heating the less dense

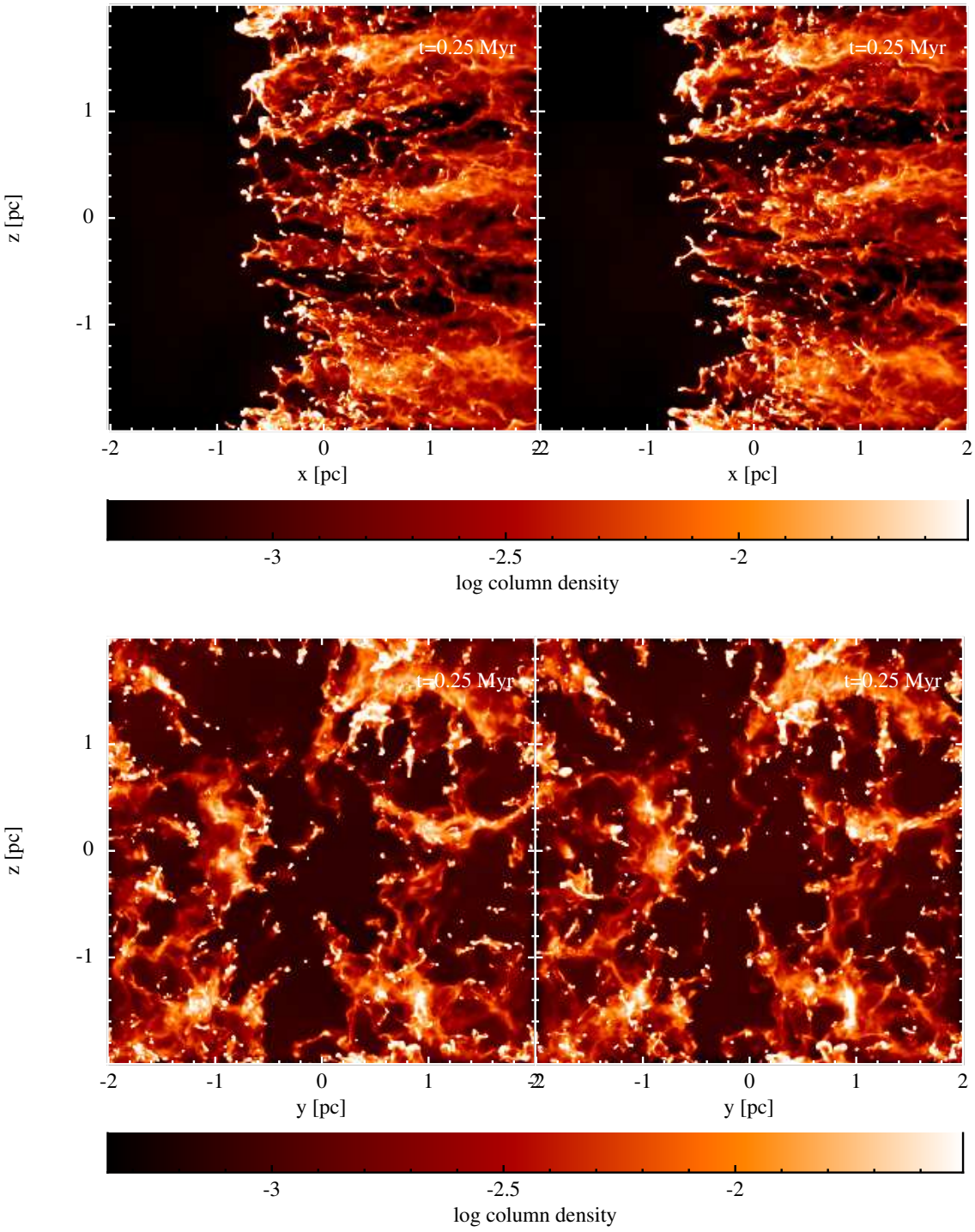

Figure 7.4: Column density plot of the turbulent cloud at $t = 0.25\,\mathrm{Myrs}$ in x - z (top); y - z (bottom). The wind + ionization case is shown in the left panels and the ionization only case is shown on the right.

gas which then exerts pressure on the cold unionized gas. In addition, the densest structures are able to shield the gas behind them. The combination of all these effects, the movement in the x-direction, the compression of the dense structure and the shielding of material behind the dense structures leads to elongated filaments with denser tips facing the feedback source.

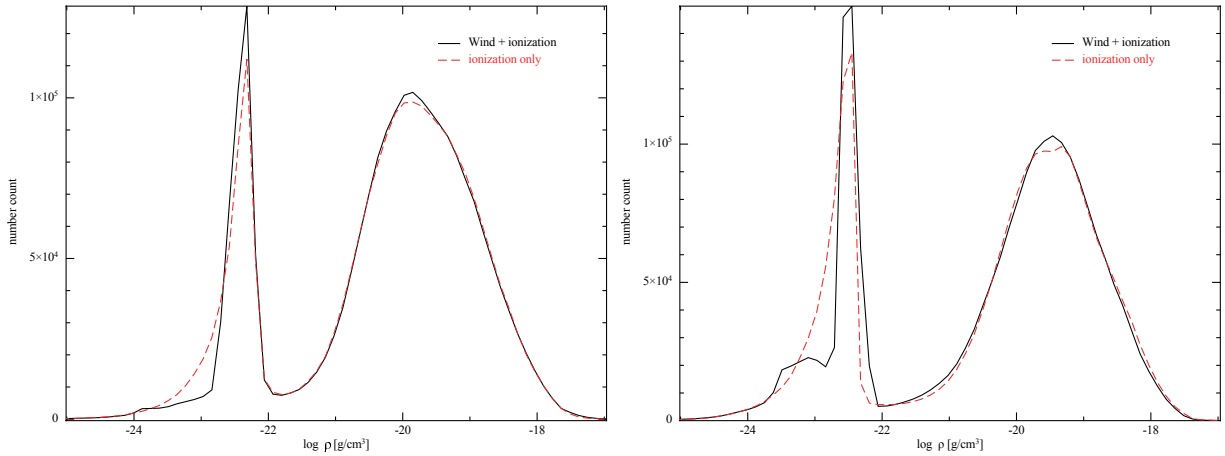

(a) $t = 0.25\,\mathrm{Myrs}$ (b) $t = 0.5\,\mathrm{Myrs}$

Figure 7.5: Density histograms comparing the wind+ionization (solid black line) case and the ionization only case (dashed red line) at two different times $t = 0.25\,\mathrm{Myrs}$ (a) and $t = 0.5\,\mathrm{Myrs}$ (b).

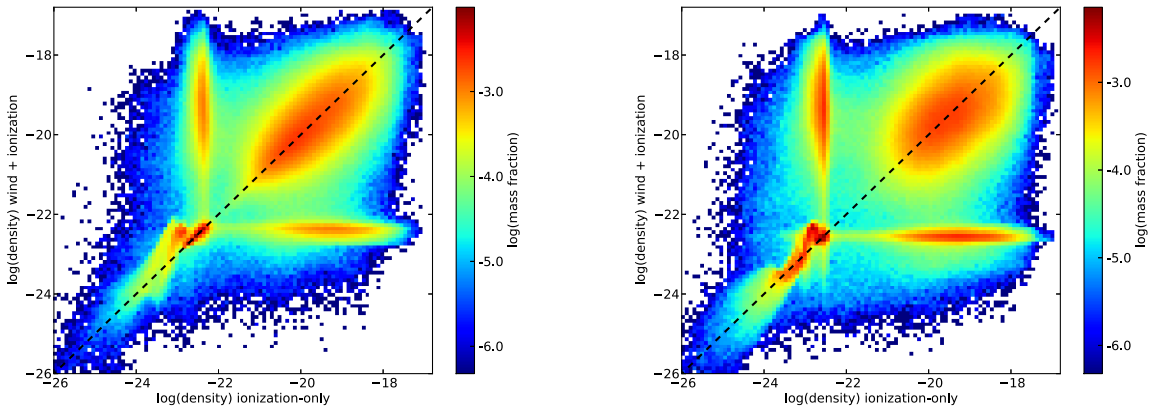

(a) $t = 0.25\,\mathrm{Myrs}$ (b) $t = 0.50\,\mathrm{Myrs}$

Figure 7.6: Density histograms comparing the wind+ionization (y-axis) case and the ionization only case (x-axis) at two different times $t = 0.25\,\mathrm{Myrs}$ (a) and $t = 0.5\,\mathrm{Myrs}$ (b).

When added, the momentum from the wind leads to a slight additional push in the x-direction. The filaments formed appear less thin than in the corresponding ionization-only.

These effects are however not very significant. Figure 7.5 shows the probability density function (PDF) for the density distribution of the gas. Both functions are very similar. They both exhibit two peaks which correspond to the ionized gas $\rho \approx 5 \times 10^{-23}\,\mathrm{g\,cm^{-3}}$ and the dense gas at $\rho \approx 5 \times 10^{-20}\,\mathrm{g\,cm^{-3}}$ which illustrates that the cold gas at 10 K and the ionized gas at 10^4 K are in pressure equilibrium. The combined feedback case produces slightly more gas at the most common densities and reduces the gas at very low densities ($< 10^{-23}\,\mathrm{g\,cm^{-3}}$).

The wind does not directly impact the cold gas. Its momentum is imparted to the ionized material in front of the cold structures. The ionized material is accelerated but not above the sound speed in the ionized gas $\sim 10\,\mathrm{km\,s^{-1}}$. No shocks are formed. The density of the dense gas is just slightly increased. This can be seen in figure 7.6. The 2D-histogram allow to compare the densities assigned to SPH-particles in the two feedback runs. As before, the dashed black line indicates equal density. Filled bins above the $x = y$-line account for particles which have a higher density in the dual feedback run, the reverse is true for those bins below the $x = y$-line. Again, the symmetric appearance of the 2D-histogram indicates that the density distributions are very similar, although the individual densities of SPH-particles can be different. The two red regions on the $x = y$-line represent the two phases seen also in figure 7.5. these particles are part of the same gas phase in both runs. The red "wings" are particles which belong to different phases in the different runs. The asymmetry for densities in the range 10^{-23} - $10^{-22}\,\mathrm{g\,cm^{-3}}$ highlights compressive effect of the winds on the ionized gas.

Chapter 8

The Mysterious Sickle Object in the Carina Nebula: A stellar wind induced bow shock grazing a clump?

In this chapter we report on multi-wavelength observations of a peculiar nebulosity around a star in the Carina Nebula and the identification of a denser molecular clump at the same location. We interpret the crescent-shaped nebulosity, which we call the "Sickle", as the tip of a bow shock associated with the B1.5 V star *Trumpler 14 MJ 218* (MJ 218 hereafter) listed in Massey & Johnson (1993). We discuss a possible link between the star, the Sickle and the clump and argue that the star is moving supersonically through the ambient density gradient on the front side of the observed compact clump. The following results and discussion are adapted from Ngoumou et al. (2013).

8.1 Observational Data

The object caught our attention because of its particular morphology in optical images of the Carina Nebula region. It is located about $1'$ south-east of the dense young cluster Tr 14, which corresponds to a projected physical distance of about 0.8 pc.

A literature search showed that the peculiar nebulosity had already been mentioned in the near-infrared (NIR) imaging study of the Tr 14 region by Ascenso et al. (2007), who suggested the idea of a compact HII region around the star. The highly asymmetric shape of the nebula could be the result of the irradiation from the very luminous early O-type stars in the center of Tr 14 (most notably the O2If star HD 93129A), since the apex of the crescent points toward this direction. Smith et al. (2010b), however, noted that the lack of detectable Hα emission is in conflict with the interpretation as an HII region; they rather argued that the crescent nebula is a dusty bow shock.

A close look at a multi-wavelength data set of the Carina Nebula shows that the crescent

nebula also appears to be related to a compact clump, which is invisible in the optical and NIR images, but quite prominent in the far-infrared and sub-mm data.

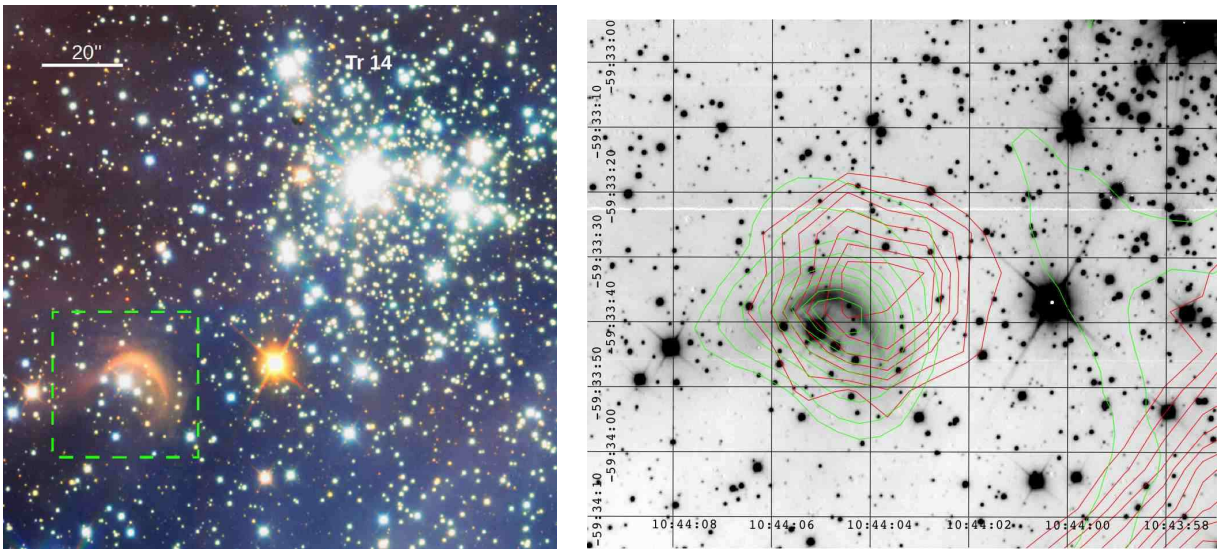

Figure 8.1: left: RGB composite image constructed from the J- (blue), H- (green), and K_s-band (red) HAWK-I images of the area around the Sickle object (marked by the green dashed box in the lower left part) and the cluster Tr 14 (see also ESO photo release 1208; http://www.eso.org/public/news/eso1208/).
right: Negative grayscale representation of the K_s-band HAWK-I image of the area around the Sickle object with superposed contours of our *Herschel* 70 μm map (green) and our APEX/LABOCA 870 μm map (red). The contours levels of *Herschel* 70 μm map are at 2.25, 2.5, 3.0, 3.5, 4.0, 4.5, 5.5, and 6.0 Jy/pixel (pixel size 3.2″); the rms noise level in the map is $\sim$ 2.3 Jy/pixel. The contour levels of the APEX/LABOCA 870 μm map go from 0.05 Jy/beam to 0.5 Jy/beam in steps of 0.05 Jy/beam; as the rms noise level in the map is $\sim$ 0.02 Jy/beam, the first contour corresponds to the $\sim 2.5\,\sigma$ level. Note that the horizontal bright streak in the background image is an artifact related to the dither pattern and the mosaicing process.

Stellar parameters The observed crescent is associated to the B1.5 V star MJ 218 as listed by Massey & Johnson (1993) in their spectroscopic and photometric analysis of the stars in and around the clusters Trumpler 14 and Trumpler 16. MJ 218 alias *2MASS J10440508-5933412*, alias *ALS 19740* in Reed (2003) is located at the J2000 coordinates $10^h\,44^m\,05.1^s$, $-59°\,33'\,41''$, at about $1'$ south-east from the center of Tr 14. With optical/NIR magnitudes of $V = 11.85$ and $K = 9.63$ the star is a bright and prominent object. The stellar spectral type was determined via optical spectroscopy by Massey & Johnson (1993). These properties are very well consistent with the assumption that this star is a member of the Carina Nebula at a distance of 2.3 kpc.

In the UCAC4 Catalogue (Zacharias et al., 2012; Zacharias et al., 2013) [1], the star is listed as UCAC4 153-055048. Its proper motion is given as pm(RA) = -7.0 ± 3.0 mas yr^{-1} and pm(Dec) = 5.2 ± 3.7 mas yr^{-1}. The total proper motion of 8.7 ± 4.8 mas yr^{-1} corresponds to 95 ± 52 km s^{-1}. This is a remarkably high velocity, but we have to note that the uncertainties are quite large. Using the radial velocity of $v_{\rm rad} = -10.9$ km s^{-1} (Huang & Gies, 2006) leads to a total space velocity of $v_* \approx 96$ km s^{-1}. This large velocity suggest that MJ 218 is a runaway star.

We note that the amplitude and direction of the motion would be consistent with the idea that the star MJ 218 could have been ejected some 66 000 years ago from the region of the open cluster Tr 16 which is at a distance of ~ 6.5 pc.

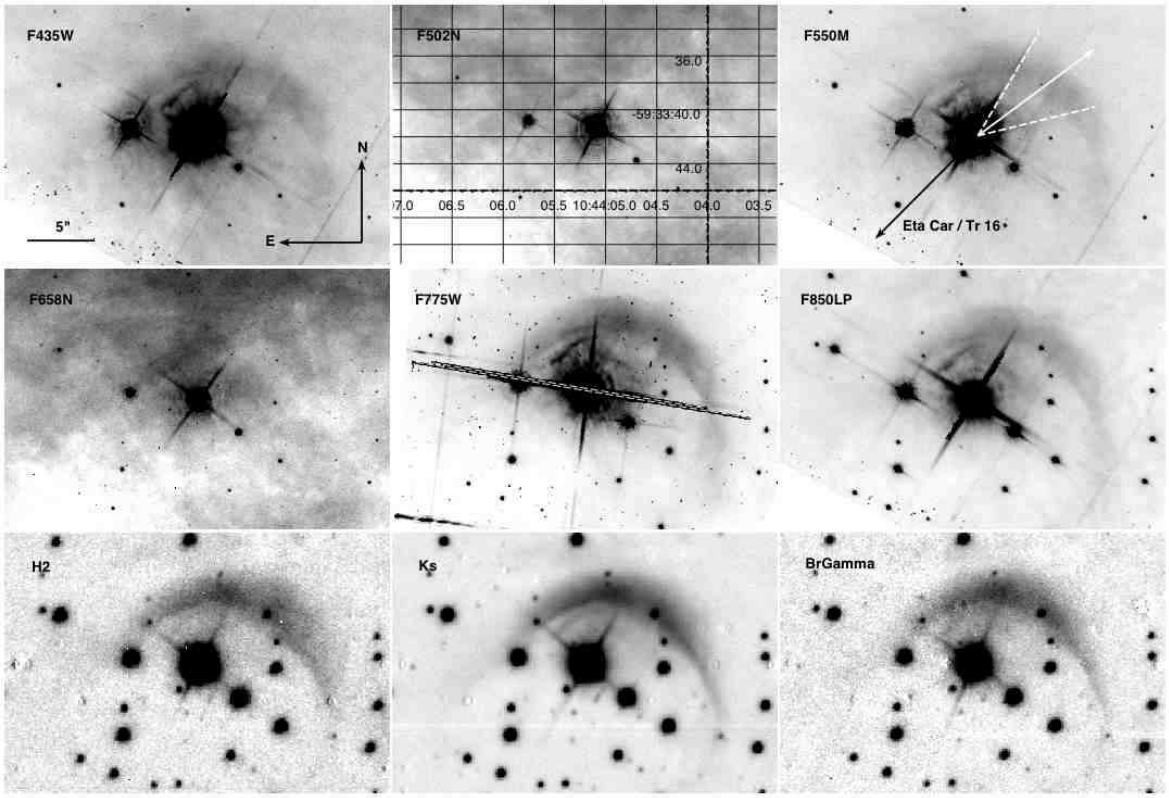

Figure 8.2: Images of the object taken with the HST (top and middle) and HAWK-I (bottom). A linear scale is used. The direction of the catalogued proper motion is indicated as a white arrow in the third panel (upper right). The uncertainty in the position angle of the velocity vector is indicated by the white dashed lines. The black arrow denotes the direction to η Carinae in Tr 16. In the fifth panel the prominent double diffraction spike is marked, indicating a bright compact source close to the B1.5V star.

[1] see http://www.usno.navy.mil/USNO/astrometry/ optical-IR-prod/ucac

Filter	Date	Exp. Time[s]	Proposal IDs
F435W	2006-07-29	698	10602 (PI: J.Maiz Appellaniz)
F502N	2010-02-01	7650	12050 (PI: Mario Livio)
F550M	2006-07-29	678	10602 (PI: J.Maiz Appellaniz)
F658N	2005-07-17	1000	10241 (PI: Nathan Smith)
F775W	2003-05-17	550	9575 (PI: William B. Sparks)
F850LP	2006-07-29	678	10602 (PI: J.Maiz Appellaniz)

Table 8.1: Journal of HST observations.

***Hubble Space Telescope* optical images** We searched the *Hubble* Legacy Archive for observations of the Sickle object. The images shown in Fig. 8.2 are taken with the Advanced Camera for Surveys (ACS). The dates of the observations, the exposure times, and the proposal identifiers are given in Table 8.1. Fig. 8.2 shows the compilation of HST in different filters, which reveal the small-scale structure of the nebulosity in detail. Two additional shells are visible closer to the star. Whereas the nebulosity is very well visible in the broad-band filters, neither the F502N band filter (tracing the [O III] line) nor the F658N filter (tracing the Hα line) reveal significant diffuse emission, clearly showing that the emission from the crescent nebula is not line-emission but continuum emission.

Near-infrared images To investigate the near-infrared morphology of the nebula, we inspected data obtained in January 2008 as part of the survey of the Carina Nebula presented in Preibisch et al. (2011b) with the instrument HAWK-I at the ESO 8m Very Large Telescope. Images were obtained in the standard J-, H-, and K_s-band filters, as well as in narrow-band filters centered on the 2.121 μm $\nu = 1{-}0$ S(1) ro-vibrational emission line of molecular hydrogen and the 2.166 μm Bracket γ line. The very good seeing conditions during these observations resulted in sub-arcsecond FWHM values of typically $0.37''$ (in the K_s-band) for the PSF size of point-like sources near the Sickle object.

Comparison of the narrow-band images with the K_s-band image shows: In the Bracket γ line, there is no increase of the brightness of the nebula relative to the star MJ 218. This excludes significant hydrogen line emission. Furthermore, there is also no indication of Bracket γ rim-brightening at the northern edge of the Sickle. Such a rim-brightening is clearly visible in narrow-band images in many of the irradiated globules in the Carina Nebula as well as in optical and near infrared images of photoevaporating globules and pillars (Smith et al., 2003; Smith et al., 2004). Rim-brightening highlights the strong surface irradiation by the surrounding hot stars. For the Sickle nebula, however, external irradiation seems not to be important.

In the molecular hydrogen line narrow-band image the relative brightness of the Sickle nebula is not much larger than in the broad-band image, but the nebulosity seems to be slightly more extended at the north-western edge. This suggests moderate amounts of molecular hydrogen line emission at the front of the nebula, similar as often observed in

the bow-shocks of protostellar jets that move through molecular clouds (Preibisch et al., 2011b; Tapia et al., 2011).

Mid-Infrared data: MSX and TIMMI2 The Sickle nebula coincides with the Mid-course Space Experiment (MSX) point source MSX6C G287.4288-00.5804. Mottram et al. (2007) performed mid-infrared imaging of this source with better angular resolution at the 3.6 m ESO Telescope and resolved the MSX source into four MIR sources. Their 10.4 μm image clearly shows the Sickle nebula (but no sign of the star MJ 218), and the peak of the emission corresponds very well to the brightest point of the Sickle as seen in our K_s-band image. Urquhart et al. (2007) and Mottram et al. (2007) reported a non-detection in radio continuum emission from this source. Urquhart et al. (2007) stated a detection limit of 0.4 mJy. Assuming an electron temperature of 10^4 K and the distance of 2.3 kpc, we derived an excitation parameter of $\sim 2\,\mathrm{pc\,cm^{-2}}$. By extrapolating Table 14.1 in Wilson et al. (2009), this value appears roughly consistent with a B1.5 star.

LABOCA sub-mm map Whereas the optical and NIR images show no indication for the presence of a dense clump in the surroundings of the Sickle nebula, the 870 μm map that was obtained in December 2007 with the bolometer array LABOCA at the APEX telescope by Preibisch et al. (2011a) clearly reveals a compact clump located close to the tip of the Sickle. The position of the peak of the sub-mm emission is $10^h\,44^m\,04.06^s$, $-59^\circ\,33'\,35.5''$, i.e. 10 arcseconds (or 0.1 pc) north-west of the star MJ 218 and about 3 arcseconds north-west of the apex point of the Sickle nebula. The sub-mm emission is almost point-like and only marginally extended; given the 18″ angular resolution of LABOCA, the width of the clump is ~ 0.2 pc. The peak of the clump emission has an intensity of 0.393 Jy/beam.

***Herschel* far-infrared maps** Maps of the Carina Nebula at the wavelengths of 70, 160, 250, 350, and 500 μm were obtained in December 2010 in the Open Time project OT1-tpreibis-1 using the parallel fast scan mode at 60″/s for simultaneous imaging with PACS (Poglitsch et al., 2010) and SPIRE (Griffin et al., 2010). A full description of these observations and the subsequent data processing can be found in Preibisch et al. (2012). The angular resolution of the *Herschel* maps is 5″, 12″, 18″, 25″, and 36″ for the 70, 160, 250, 350, and 500 μm band, respectively. At a distance of 2.3 kpc this corresponds to physical scales ranging from 0.06 to 0.4 pc.

The clump near the Sickle nebula detected by LABOCA is clearly visible in the *Herschel* maps. It is clearly extended in the PACS maps, where we determine FWHM values of $19'' \times 16''$. These maps also show that the shape of the clump is not central symmetric. It exhibits a kidney-shaped form (green contours in Fig. 8.1, right panel), with a slight caved-in side in south-east direction in accordance with the inner side of the Sickle nebula bow. This clearly suggests that the process creating the Sickle nebula bow interacts with the clump.

Using the methods described in Preibisch et al. (2012), we determined the column density, temperature, and mass of the clump. The peak value for the column density in

the center of the clump is $N_{\rm H} \approx 1.3 \times 10^{22}\,{\rm cm}^{-2}$, corresponding to a visual extinction of $A_V \approx 6.5$ mag assuming a normal extinction law (note that these numbers are beam-averaged values, i.e. the true values for a line-of-sight exactly through the center will be higher). The dust temperature in the clump is found to be about 32 K. The mass of the clump can be determined by integrating the column density over all pixels exceeding the limit $A_V > 3$ mag (in order to separate the clump from the surrounding diffuse gas); this yields $M_{\rm clump} \approx 40\,M_\odot$.

X-ray data The object is located in the area covered by the *Chandra* Carina Complex Project, that recently mapped a 1.3 square-degree region of the Carina Nebula. With an exposure time of ~ 60 ksec (~ 17 hours) for the individual mosaic positions, the on-axis completeness limit is $L_{\rm X} \approx 10^{29.9}$ erg/s in the $0.5-8$ keV band for lightly absorbed sources. A complete overview of the *Chandra* Carina Complex Project can be found in Townsley et al. (2011a), which is the introduction to a set of 16 papers resulting from this project.

In the *Chandra* images analyzed in the context of the CCCP, the star MJ 218 is clearly detected as an X-ray point-source with 59 source counts. The J2000 position of the X-ray source is $10^h\,44^m\,05.09^s$, $-59^\circ\,33'\,41.4''$ and has a total 1-σ error (individual source position error and systematic astrometrical uncertainty) circle radius of $\approx 0.4''$ (Broos et al., 2011). This position agrees perfectly (i.e. within less than $0.1''$) with the optical position of the star listed in the UCAC4 catalog ($10^h\,44^m\,05.091^s$, $-59^\circ\,33'\,41.37''$). The positional offset to the corresponding 2MASS counterpart is $0.2''$, i.e. well within the uncertainties. From our inspection of the optical HST image we found an (insignificant) offset of $0.1''$ between the star and the X-ray source position; the nearest other star visible in the HST image is $3.8''$ offset from MJ 218. In the near-infrared HAWK-I images, we found an (insignificant) offset of $0.2''$, and a distance of $1.9''$ to the nearest other point-source. We therefore conclude that we have a clear and unambiguous identification of the X-ray source with the star MJ 218.

The X-ray properties of this source can be summarized as follows (see Broos et al., 2011, for details): the median photon energy of the source is 1.48 keV. The analysis of the photon arrival times yields some, although rather weak evidence for variability: the Kolmogorow-Smirnow test gives a probability of $P_0 = 0.16$ for the null hypothesis of a constant count rate. The fit to the X-ray spectrum with XSPEC yielded as plasma temperature of $kT = 2.5(\pm 0.8)$ keV and gave an extinction-corrected intrinsic X-ray luminosity of $L_{\rm X} \approx 8.3 \times 10^{30}\,{\rm erg/sec}$.

According to the well established results for the origin of stellar X-ray emission (see, e.g. Güdel & Nazé, 2009), no X-ray emission is expected for MJ 218, since stars of spectral type B1.5 should neither show coronal magnetic activity as typical for late-type (spectral types F and later) stars, nor should they have sufficiently strong stellar winds, in which X-ray emission is produced in wind shocks, as observed in the (much more luminous) O-type stars. The general lack of intrinsic X-ray emission from stars in the spectral type range from $\sim$ B1 to late A has been well confirmed in numerous X-ray observations (e.g., Schmitt et al., 1985; Daniel et al., 2002; Preibisch et al., 2005; Stelzer et al., 2005).

The common explanation for the detections of X-ray emission from B stars is thus the

assumption that the emission actually originates from an unresolved late-type companion (e.g., Evans et al., 2011). The observed median photon energy and the plasma temperature of MJ 218 derived from the X-ray spectrum are fully consistent with this assumption, and considerably higher than one would expect from wind-shock related X-ray emission (e.g., Kudritzki & Puls, 2000). Considering the general correlation between X-ray luminosity and stellar mass for young stars (see Preibisch et al., 2005), the observed X-ray luminosity suggests the companion to have a stellar mass around $\sim 1 - 2\,M_{\odot}$. Given the above described upper limit for a possible angular offset of the X-ray source from the B-star position of $\leq 0.2''$, the putative low-mass companion must have a projected separation of less than ~ 460 AU from the B-star. This rather small value makes a chance projection highly unlikely.[2] Since many B-type stars are known to have lower-mass companions at separations of a few ten to a few hundred AUs (see, e.g., Preibisch et al., 1999; Kouwenhoven et al., 2007; Grellmann et al., 2013) the hypothesis of a binary system seems to be the best explanation of the observed parameters.
We searched in the HST images for such a companion, but even the narrow-band images are saturated at the required small distances from the position of MJ 218 due to the brightness of the star.[3]

8.2 Theoretical Considerations

8.2.1 Clump Carving Scenario

The evolution of the wind bubble around a star located at the edge of a clump can lead to a crescent-like shaped shock front. We performed a simulation using the SPH code SEREN (Hubber et al., 2011) including our newly implemented HEALPix-based momentum conserving stellar wind-scheme to simulate the expansion of a momentum driven wind bubble in a molecular clump. The choice of momentum driven (Steigman et al., 1975) as opposed to thermal pressure driven (Castor et al., 1975; Weaver et al., 1977) is justified, as the stellar winds of a spectral type B1.5 are assumed to be too weak to induce a hot shocked, X-ray emitting layer.

The clump was modeled as a self-gravitating isothermal sphere with a Bonnor-Ebert density profile (Bonnor, 1956; Ebert, 1957). The sphere has the dimensionless radius $\xi = 8$ and a finite radius $R_{\mathrm{BES}} \approx 0.31$ pc, corresponding to a FWHM size of ~ 0.2 pc and a central density of $\rho_{\mathrm{BES}} \approx 1.7 \times 10^{-19}\,\mathrm{g\,cm^{-3}}$ at a temperature of 36 K, for a total mass of $M_{\mathrm{clump}} = 40\,\mathrm{M}_{\odot}$. A static momentum source was placed at the edge of the nebula at a distance of 0.29 pc from the center of the clump. We used the mass loss rate and terminal

[2] In order to quantify this statement, we inspected the HST image and counted the number of detectable stars within $10''$ of MJ 218 to be 8. With this estimate of the local star density, the Poisson probability to find one or more unrelated stars as chance projection within $0.2''$ of MJ 218 is just 0.3%.

[3] The HST images (Fig. 8.2) show a double diffraction spike indicative of a companion separated by about 0.2 arcsec in north-south direction. The similar brightness of this potential companion, however, disqualifies it as X-ray source.

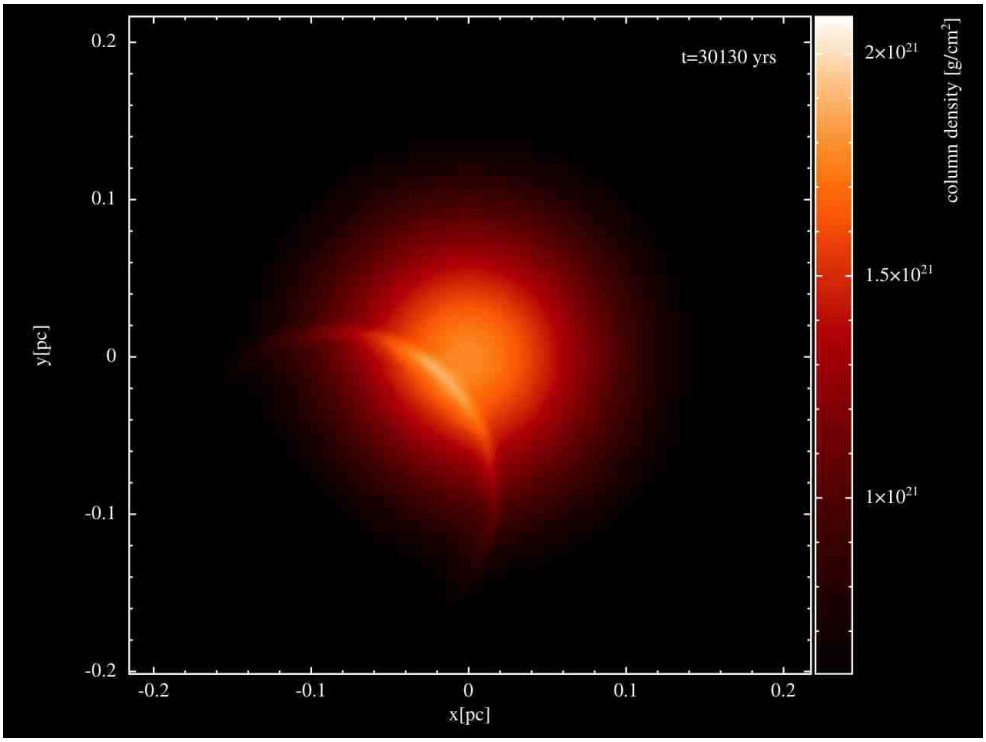

Figure 8.3: Integrated density plot for a projected star-clump distance $d_{obs} = 0.11$ pc at an inclination of $\alpha = 66°$. The image was produced using SPLASH (Price, 2007)

wind velocity for a B1.5 V star as stated by Smith (2006): $\dot{M}_{\rm w} = 6 \times 10^{-8}\,{\rm M}_{\odot}\,{\rm yr}^{-1}$ and $v_{\infty} = 960\,{\rm km\,s}^{-1}$.

After a few 10^4 yrs, the crescent has reached the size of the observed object. To match the observed projected distance $d_{obs} \approx 0.11$ pc between the star and the center of the clump (inferred from the sub-mm map), the simulation box is rotated by an angle $\alpha = 66°$ around the axis passing the center of the clump and perpendicular to the clump-star axis. Fig. 8.3 shows the density integrated along the line of site at $t = 3 \times 10^4$ yrs when the crescent has reached the size of the Sickle. The inclination angle between the plane containing the star and the center of the clump, and the projection plane is $\alpha = 66°$.

This scenario though, requires the star to be embedded inside the clump. It seems unlikely that MJ 218 was born inside or close to the clump as it would certainly have been dispersed by the stellar wind by now. The assumption that the star is coming from somewhere else and travelled through the ISM, finding itself embedded inside the clump would require wind shell radii smaller than the radius of the clump. Shells with larger radii would overrun the clump, and compress it (Bisbas et al., 2011; Gritschneder et al., 2010; Tremblin et al., 2012) leading to a cometary/pillar like structure with the tail pointing away from the star. This is not observed. The required compact shell could be produced naturally if the star would move supersonically through the ISM. In this case, a star produces a bow shock with smaller radii at the collision front of the wind with the ambient

medium, which we discuss in the next section.

8.2.2 Bow Shock Scenario

The reported velocity of MJ 218 is very high ($\sim 96\,\mathrm{km\,s^{-1}}$). The errors, however, are of the order of 55%, making the value rather uncertain. A star with such high velocity forms a bow shock while traveling through an ambient medium with temperatures $T \leq 10^6$ K. Indeed, the position of the tip of the arc approximately correlates with the direction of the velocity vector in the plane of the sky as inferred from proper motion measurements of the star (see Fig. 8.2). To test this scenario we compare the distance between the star and the cusp of the Sickle nebula with the stand-off radius R_0 inferred from the analytical solution for the shape of a stellar wind bow shock in the thin-shell limit as derived in Wilkin (1996). R_0 depends on the velocity of the star v_*, on the wind mass loss rate $\dot{M}_\mathrm{w}$, on the terminal wind velocity v_w and on the ambient density ρ_AMB.

$$R_0 = \sqrt{\frac{\dot{M}_\mathrm{w} v_\mathrm{w}}{4\pi \rho_\mathrm{AMB} v_*^2}} \tag{8.1}$$

The shape of the bow shock near the stand-off radius is given by:

$$R_\theta = R_0 \,\mathrm{cosec}\,\theta \sqrt{3\,(1 - \theta \cot\theta)} \tag{8.2}$$

with θ being the polar angle measured from axis given by the direction of motion of the star (see Fig. 8.4).

Fig. 8.5 shows the variation of the stand-off radius of the bow shock with ambient density (Eq. 8.1) for a range of stellar velocities and for two sets of wind parameters P1(red dot-dashed) and P2(blue dashed).

P1 $\dot{M}_\mathrm{w} = 1.1 \times 10^{-8}\,\mathrm{M_\odot\,yr^{-1}}$; $v_\infty = 1400\,\mathrm{km\,s^{-1}}$ (based on models computed by Pauldrach et al., 2001) [4]

P2 $\dot{M}_\mathrm{w} = 6 \times 10^{-8}\,\mathrm{M_\odot\,yr^{-1}}$; $v_\infty = 960\,\mathrm{km\,s^{-1}}$ (Smith, 2006)

The shaded area represent the spread due to the 55% error on v_*. The horizontal solid line indicates the stand-off radius inferred from the reported proper motion and radial velocity measurements which indicate an inclination angle of $\sim 6^\circ$ and a value of R_0 of ~ 0.075 pc. The star is almost moving in the plane of the sky.

The observed stand-off distance is obtained for number densities ranging between $\sim 0.1\,\mathrm{cm^{-3}}$ and $\sim 20\,\mathrm{cm^{-3}}$. The range of ambient densities is given by the large errors on the velocity estimate for MJ 218 (shaded area in Fig. 8.5). For the reported $\sim 96\,\mathrm{km\,s^{-1}}$, $n_{AMB} = 2\,\mathrm{cm^{-3}}$ for P1 and $n_{AMB} = 8\,\mathrm{cm^{-3}}$ for P2. These values are consistent with an order-of-magnitude estimate for the density of the rather diffuse gas in the inner parts of the Carina Nebula superbubble, through which the star is moving. This hints at the Sickle

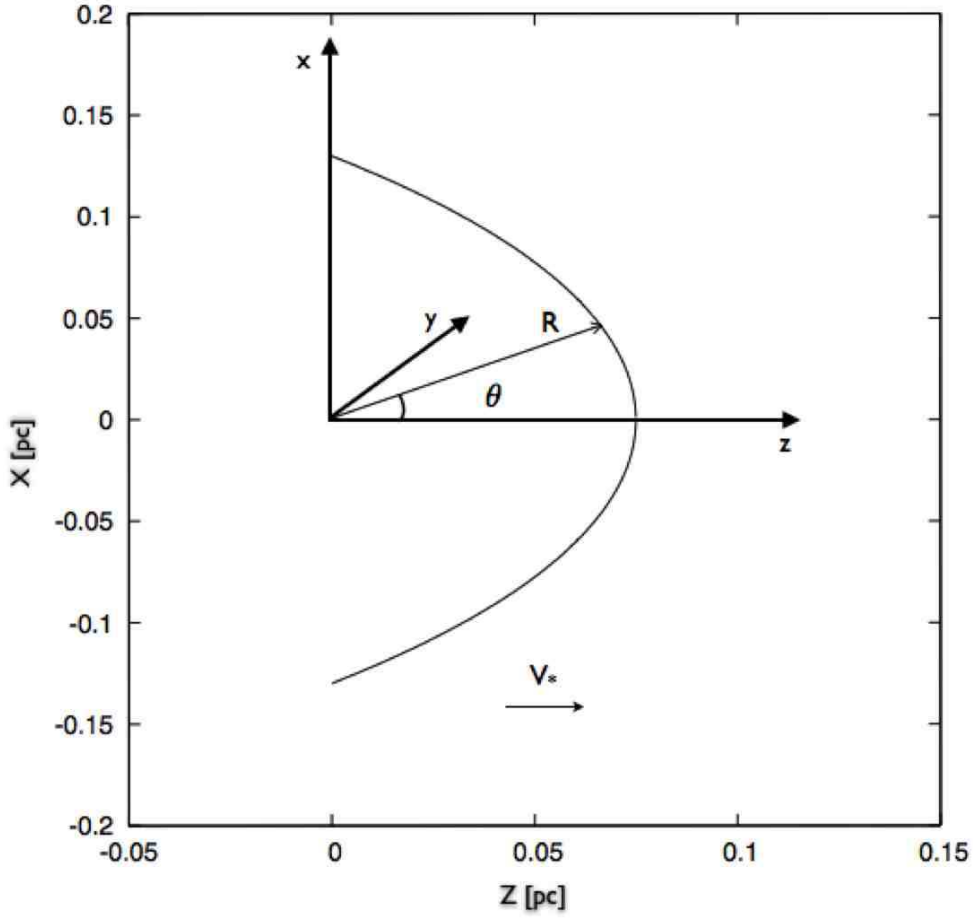

Figure 8.4: Schematic diagram of a stellar wind bow shock to illustrate the definition of the coordinate system.

being the bow shock induced by MJ 218 moving supersonically through the diffuse ISM and not directly interacting with the densest part of the clump.

The question now arises whether we just see a star with a bow shock projected in front of an unaffected clump. Interestingly, the bow shock does not appear to be symmetric around the axis given by the velocity vector of MJ 218 (see upper right panel in Fig. 8.2) as expected if the star would move in isolation. We therefore suggest that we indeed see a contribution from the clump. Wilkin (2000) investigated the modifications of bow shocks of stars running into an ambient density gradient in the direction perpendicular to the stellar motion and the effect of anisotropic winds. In both cases he found configurations in which the star does not lie on the symmetry axis dividing the bow shock into two parts. The observed asymmetry for the position of MJ 218 with respect to the tip of the Sickle might therefore be an indication of an interaction of the moving star with the clump. As an

[4]see http://www.usm.uni-muenchen.de/people/adi/Models/ Model.html

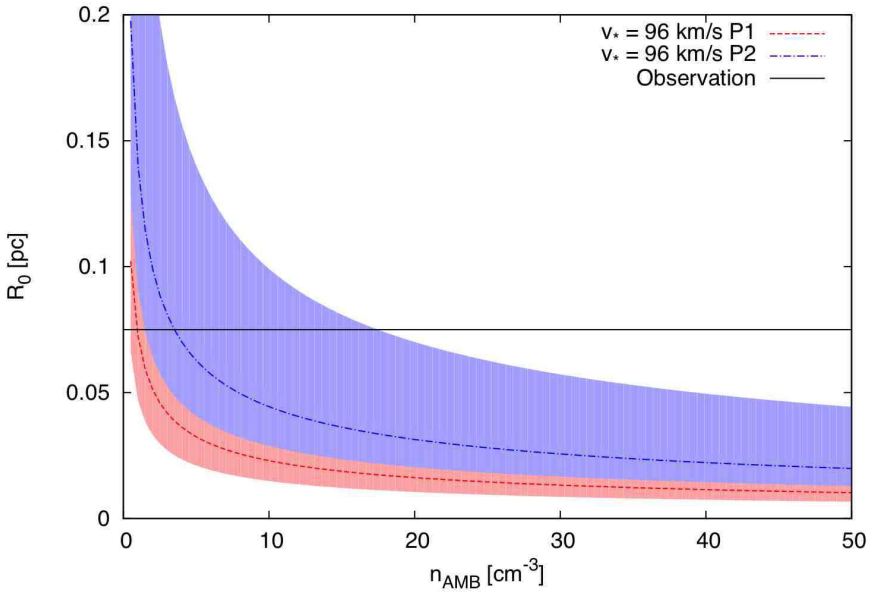

Figure 8.5: Stand-off radius of the bow shock (Eq. 8.1) against number density of the ambient medium for $v_* = 96\,\mathrm{km\,s^{-1}}$ and for two sets of stellar wind parameters; P1 (red dot-dashed): $\dot{M}_\mathrm{w} = 1.1 \times 10^{-8}\,\mathrm{M_\odot\,yr^{-1}}$ and $v_\infty = 1400\,\mathrm{km\,s^{-1}}$; P2 (blue dashed): $\dot{M}_\mathrm{w} = 6 \times 10^{-8}\,\mathrm{M_\odot\,yr^{-1}}$ and $v_\infty = 960\,\mathrm{km\,s^{-1}}$. The shaded area represent the spread due to the 55% error on v_*. The horizontal solid line indicates the stand-off radius inferred from observations.

illustration we consider the solution for a bow shock of a star moving in a linear stratified medium with a density gradient perpendicular to the stellar velocity vector as described in Wilkin (2000):

$$\rho_{AMB} = \rho_0\,(1 + ay) \tag{8.3}$$

The characteristics of the solution near the stand-off point for a bow shock seen from the side (i.e. v_* perpendicular to the line-of-sight) are given by (see Eq. (71) in Wilkin (2000)):

$$\frac{R_\theta}{R_0} = 1 - \frac{aR_0}{4}\theta + \left[\frac{1}{5} + \frac{5}{32}a^2R_0^2\right]\theta^2 \tag{8.4}$$

We approximate the gradient a by selecting two points on the observed bow and measure their respective angles θ_1 and θ_2 and the corresponding distances R_{θ_1} and R_{θ_2} from the star. From Eq. 8.4 we estimate to first order:

$$a = \frac{4}{R_0^2}\left(\frac{R_{\theta_1} - R_{\theta_2}}{\theta_2 - \theta_1}\right) \tag{8.5}$$

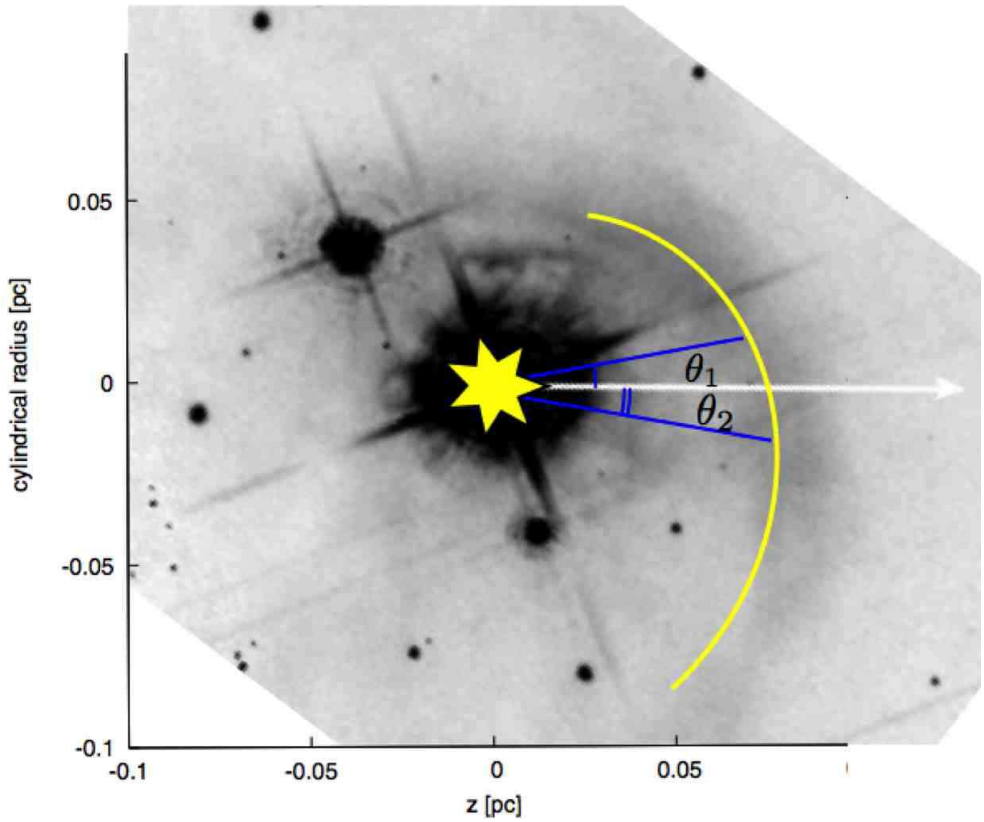

Figure 8.6: Illustration of a bow shock solution in a linear stratified medium with slope $a \approx 15\,\mathrm{pc}^{-1}$ for $R_0 = 0.075$ pc overlaid on an HST image (F550M band filter; image is rotated by 36°). The velocity vector points in z-direction.

Fig. 8.6 shows the result of this approximation (yellow arc) for $R_{\theta_1} \approx 0.95 R_0$ at $\theta_1 \approx 10°$ and for $R_{\theta_2} \approx 1.05 R_0$ at $\theta_2 \approx -10°$. The model illustrates the non axis-symmetric shape of the bow shock induced by the additional term in the linear term near the stand-off point.

The asymmetric shape of the Sickle could be the result of MJ 218 running in a medium stratified in the direction perpendicular to its motion which coincides with the line-of-sight and the position in the sky of the clump. The observed clump could therefore be part of the stratification and be located behind the Sickle.

8.3 Conclusion

The Sickle nebulosity in the Carina Nebula is by itself already a very remarkable and interesting feature. The discovery of a dense cloud clump at a projected location just in front of the Sickle prompted us to investigate a possible relation between these two features. We simulated the impact of the momentum transfer from the stellar wind on a clump with the star being located at the edge of the clump. The off-center expansion of the wind bubble could create a crescent-like front which resembles the observed Sickle nebula. This

scenario, however, requires a static source embedded in the clump. The star would have to be formed in the last 10 000 yrs at this position. This seems very unlikely. We therefore exclude this scenario.

Measurements of the proper motion of MJ 218 taken from the UCAC 4 catalogue (Zacharias et al., 2012) indicate a high velocity of nearly $v_* = 96\,\mathrm{km\,s^{-1}}$. At this velocity the wind of MJ 218 would form a bow shock while traveling through an ambient medium with temperatures $T \leq 10^6$ K. The Sickle could be part of the bow shock of MJ 218 seen from the side, as MJ 218 appears to be moving almost in the plane of the sky. Assuming the stand-off radius to be the distance between the star and the intersection of its velocity vector with the Sickle, we measure a stand-off radius $R_0 \approx 0.075$ pc. Such values for R_0 point at ambient densities in the range of $\sim 0.1\,\mathrm{cm^{-3}}$ and $\sim 20\,\mathrm{cm^{-3}}$ which are far lower than the $10^4\,\mathrm{cm^{-3}}$ inferred for the center of the observed clump. The star is thus not moving through the inner, central parts of the clump, but seems to be grazing along the surface of the clump.

The non-axisymmetric appearance of the Sickle is consistent with the presence of a density gradient perpendicular to the direction of motion of MJ 218, which coincides with the line-of-sight and the location of the clump. We therefore argue that the observed Sickle is part of the bow shock of the high velocity B-star MJ 218 grazing the front surface density gradient of the observed compact clump. The asymmetry of the Sickle with respect to MJ 218 can then be explained as a result of this interaction.

We expect the Sickle to be a rather transient feature which is likely to evolve on timescales of order 10^4 yrs. Surely more detailed observation of this peculiar object will help to better constrain its nature. Spectral information from the molecular material could probe the velocity structure inside the clump and help test our star-clump interaction scenario. An interesting question is also whether the passage of the star could trigger the gravitational collapse of the clump and lead to star formation. This issue will be addressed in a subsequent paper. In addition a closer look at the binary nature of MJ 218 and its implications could help shed a light on the complex history of the Carina Nebula. Especially the question of the origin MJ 218 in the framework of the formation of massive runaway binaries (McSwain et al., 2007; Gvaramadze et al., 2011; Gvaramadze et al., 2012) would be worth investigating. The direction of the velocity vector of MJ 218 suggests a possible origin in the open cluster Trumpler 16 in the center of the Carina Nebula. The observed proper motion would then imply a travel time of about 10^5 yrs. It is very interesting to note that the back-projected motion path puts MJ 218 in close vicinity of a recently detected neutron star candidate in the Carina Nebula, described in Hamaguchi et al. (2009). This raises the possibility that MJ 218 has perhaps been ejected in a relatively recent supernova explosion in the Carina Nebula. Further investigations of this relations could thus provide interesting information on the dynamical evolution, stellar clustering (Moeckel & Bate, 2010) and the still very unclear history of past supernovae in the Carina Nebula.

Chapter 9

Discussion and Outlook

9.1 Summary and Discussion

We have presented the implementation of a new momentum wind scheme for the SPH code SEREN. This new scheme allows us to study the impact of the momentum transfer from stellar wind ejecta on the surrounding molecular and ionized density distribution. In conjunction with the ionization scheme described in Bisbas et al. (2009) we were able to study the impact of main-sequence massive star feedback on a set of model molecular clouds for three different cases: the momentum wind only case, ionizing radiation-only case and the dual feedback case combining ionization and momentum winds.

As a first investigation, we looked at the impact of momentum winds and ionization from a massive star on a uniform density environment. We used values for the wind mass loss $\dot{M} = 10^{-6}\,\mathrm{M}_{\odot}\,\mathrm{yr}^{-1}$, the wind velocity $v_{\mathrm{WIND}} = 2000\,\mathrm{km\,s}^{-1}$ and the ionizing photon rate $N_{\mathrm{Lyc}} = 10^{49}\,\mathrm{s}^{-1}$, close to those for an O7.5-star as cataloged by Smith (2006) in his census of massive stars in the Carina Nebula.

We found that in a cold molecular environment, the pure transfer of momentum from the stellar wind is able to sweep up and compress the gas. It never reaches the gas densities which are obtained in the ionization runs with the same initial conditions. This makes momentum winds much less efficient than ionizing UV radiation in compressing cold gas and eventually triggering star formation. When combined with the ionizing radiation, the latter is the main agent in shaping and compressing the cold gas. The momentum wind then only affects the inner most part of the ionized region. This leads to a sort of "projected donut"-morphology of an H II-region with a small hole around the feedback source, similar in part to the description of the structure of the inner Orion nebula given by O'Dell et al. (2009).

Applying the wind and ionization feedback to a self-gravitating core with a Bonnor-Ebert density profile shows that the momentum wind has both a compressive and dispersive effect on the core. The compression does not lead to the high densities we obtain in runs including ionization and is not enough to induce gravitational collapse. In the combined feedback case, the ionizing radiation is mostly responsible for compressing the core and

inducing collapse. The dense filamentary structures forming are very similar in the dual feedback case and in the ionization-only case. When exposed to different feedback strength, the weak and intermediate-feedback runs (modeled as the effect of a B0 star and O7.5 star respectively) lead to the formation of a sink particle. For the B0 case, sink formation occurs a bit earlier in the dual feedback run, while in the O7.5 case sink formation is slightly delayed in the dual-feedback case. For the strong feedback case, no sink particle is formed. The cold material is evaporated before it can become dense enough to undergo gravitational collapse. Interestingly in those cases where sink particles are formed, these appear located further inside the central filament and not directly at the edge facing the feedback source. A similar configuration is observed in the globule LBN 777 in the Taurus molecular cloud where a protostar is observed away from the central core of the globule (Clark, 1991).

We looked at the evolution of a structured, turbulent molecular cloud under the influence of the feedback from the fiducial O7.5-type star. While in the wind-only case the side of the cloud facing the source, shows the marks of the momentum transfer, the structures do not at all resemble the pillars and filaments seen in the runs involving the ionizing radiation. This is explained by the different ways the two mechanisms operate. The momentum transfer from the winds leads to the localized acceleration of the impacted particles, which get pushed inside the clouds leading to additional compression, particularly for low to mid density gas ($\rho \leq 10^{-21}\,\mathrm{g\,cm^{-3}}$). The ionizing radiation, in turn, creates a high pressure environment where the hot $10^4\,\mathrm{K}$ gas can push through the low density channels and carve out and compress the dense structure seeded by the initial turbulence. Pillar like structures with dense tips and small globules are formed similar to the structures described in Gritschneder et al. (2010). The structures in the wind+ionization case and the ionization-only run are very similar. The additional momentum wind leads to slightly higher densities in some of the diffuse ionized gas. The cold gas is not directly affected by the momentum winds.

Dale et al. (2014) modeled the combined effects of ionizing radiation and momentum winds from O-stars on a range of GMC-type clouds. Their results are in accordance with those presented in this work. They note only a very modest impact of the momentum-driven winds on the cold molecular structures. The dynamical effects are dominated by the ionizing radiation. They find that the inhomogeneous structure of the clouds allows for the ionized gas to leak, thereby reducing the ability of pre-supernova feedback to compress molecular material. The feedback's ability to unbind material is however dependent on the escape velocity of their model clouds. While the clouds with low density are destroyed, the stellar feedback had little effect on the denser objects.

Our simulations of the combined impact of the momentum wind and the ionizing radiation from a massive star on molecular clouds confirm the results of the 1D analytical calculations for the case of mixed nebular and wind material presented by Capriotti & Kozminski (2001). The ionizing UV radiation is the main driver of the dynamical evolution of the gas. In the case of triggered star formation, the additional momentum wind does not substantially change the outcome. It might lead to slightly earlier or delayed star formation, but it is unlikely to trigger any extra star-forming events that wouldn't

happen in the ionization-only case. Overall the contribution from the additional momentum from winds to the dynamics of molecular gas and its impact on star formation is very modest. Simulations by Dale et al. (2014) of the combined effects of photoionization and momentum driven winds on giant molecular clouds have lead to similar conclusions. Their finding, that the momentum wind has little effect on the densest and most massive regions, is confirmed by our comparison of the effects of the different types of feedback on a self gravitating core and on an external molecular cloud. The global appearance and evolution of the dense gas is almost indistinguishable in the ionization-only and in the corresponding wind+ionization cases. We argue that observations of the dynamics of cold molecular gas in cores and clumps is not likely to provide much information on the role of winds in their evolution. But as our simulations show, the material accumulated in the denser structures and eventually involved in sink formation is partially different. This indicates that winds might contribute to the localized redistribution and mixing of gas and could thus impact the metallicity distribution in the vicinity of massive stars.

The simulations presented here and the results presented by Dale et al. (2014), convey the impression that the winds from massive stars play a secondary role in shaping the structure in the Carina Nebula. This paints a similar picture to the one resulting from the semi analytical models of the Carina Nebula X-ray bubble presented by Harper-Clark & Murray (2009). They argued that the dynamics of the bubble where not strongly affected by the stellar winds as a result of the leakage of the hot gas. All this, together with the presence of the high-velocity star MJ 218 and the associated peculiar Sickel object could perhaps back up indications that the highly complex structure of the Carina Nebula has experienced a supernova event in its recent past.

9.2 Outlook and Next Steps

The SPH method used here allowed us only to model the impact of the momentum winds. However, as outlined in the 1D analytical models presented in chapter 3, winds would have the most impact during the pressure driven phase of the bubble expansion. For the correct treatment of wind-ISM interactions, the low density hot ($T \geq 10^6\,\mathrm{K}$) shocked wind phase needs to be considered together with the cold dense molecular regime. This can lead to under-resolved hot regions unless a high number of SPH particles with very low mass is used. Also, to properly follow the evolution of the hot gas, would require very small time steps for solving the momentum and energy equations. The high number of particles and the small time steps significantly increase the computational costs for SPH calculations.

Another issue that needs to be considered when modeling the impact of stellar feedback on the ISM, is the treatment of fluid instabilities, in particular for large density, temperature and velocity contrasts. In standard SPH, when a particle from a hot low-density region finds itself next to a colder high-density region, its density will be overestimated, as most of its neighbors within the smoothing radius will be inside the dense region. Because of momentum conservation, a repulsive force is exerted on the hot particle. This leads to the formation of a gap between the two gas phases (Agertz et al., 2007). The mixing of the

two phases is thereby inhibited. Hubber et al. (2013b) show that increasing the number of neighbors and the resolution can reduce this effect. Including artificial conductivity effects also helps to "bridge the gap" but leads to additional noise which can in turn influence the development of instabilities.

For the reasons mentioned above modeling the impact of the hot wind phase on the cold ISM in SPH becomes a numerically complex and costly task. A possible way to go would be to use finite-volume methods, where the physical values are evaluated at discrete points on a mesh geometry. They are of Eulerian nature and don't require a density kernel-function. But most importantly, the fluxes at the cell interfaces are computed using Riemann solvers, which calculate the exact interaction between the hot and the cold gas and thus capture shocks very accurately. Mesh-methods with adaptive resolution schemes appear better suited to model the dynamics of a multiphase ISM with very large density and temperature contrasts.

Modeling the action of winds and supernovae, including the very hot shocked gas, and investigating the interaction and mixing of the different gas phases, necessitates an appropriate treatment of different types of fluid instabilities. These include the Vishniac instability, the Rayleigh-Taylor instability and the Kelvin-Hemholtz instability. The latter occurs at the interface between two fluids with different velocities and leads to turbulent behavior and mixing of gas phases at the contact surface. This instability is expected, for example, in regions where the warm or hot gas streams around a colder structure.

Indeed Westmoquette et al. (2010) report on the presence of both a broad velocity component, with $50 - 150\,\mathrm{kms}^{-1}$ and a more narrow component, with $\sim 20\,\mathrm{kms}^{-1}$ in their Hα line profiles observations of pillars in the Galactic H II-region NGC 6357. They interpret the broadest component as emission originating in the turbulent mixing layer on the surface of the pillars, which is generated by the shear flow from the O-stars in the cluster. Simulations of such pillars would help us to better assess the role of feedback from massive stars. But in order to be compared to observations, they would have to include a number of physical processes: the impact of the hot stellar winds, the ionizing radiation, possibly the action of supernova explosions, the interaction of the multiple gas phases, an adequate treatment of turbulent motions, self-gravity and gravitational collapse. Although simulating such a complex system in detail is a very challenging task, new numerical tools, like adaptive moving mesh methods are being developed, which might be well suited to tackle the complex physics of star forming regions.

Moving mesh methods combine some of the advantages of grid based and SPH methods. They make use of exact Riemann solvers, so that shocks and strong gradients are captured accurately and they can adjust the spatial resolution automatically, similarly to SPH formulations (Springel, 2010a). Such techniques will allow us to model the shocks produced by turbulent supersonic motions, to resolve structures in different density and temperature regimes and to study the different instabilities at the interfaces. This will lead to much more accurate and realistic models, suitable to be compared to detailed observations of the ISM and of star forming regions like the Carina Nebula.

Bibliography

Ackermann, M. et al. (2013). "Detection of the Characteristic Pion-Decay Signature in Supernova Remnants". In: *Science* 339, pp. 807–811.

Agertz, O. et al. (2007). "Fundamental differences between SPH and grid methods". In: *Mon. Not. R. Astron. Soc.* 380, pp. 963–978.

André, P. et al. (2010). "From filamentary clouds to prestellar cores to the stellar IMF: Initial highlights from the Herschel Gould Belt Survey". In: *A&A* 518, L102, p. L102.

Ascenso, J., J. Alves, S. Vicente, & M. T. V. T. Lago (2007). "NTT and VLT diffraction limited imaging of Trumpler 14: revealing a massive core-halo cluster". In: *A&A* 476, pp. 199–215.

Audit, E. & P. Hennebelle (2005). "Thermal condensation in a turbulent atomic hydrogen flow". In: *A&A* 433, pp. 1–13.

Barnes, J. & P. Hut (1986). "A hierarchical O(N log N) force-calculation algorithm". In: *Nature* 324, pp. 446–449.

Bate, M. R. & A. Burkert (1997). "Resolution requirements for smoothed particle hydrodynamics calculations with self-gravity". In: *Mon. Not. R. Astron. Soc.* 288, pp. 1060–1072.

Bate, M. R., I. A. Bonnell, & N. M. Price (1995). "Modelling accretion in protobinary systems". In: *Mon. Not. R. Astron. Soc.* 277, pp. 362–376.

Bate, M. R., I. A. Bonnell, & V. Bromm (2003). "The formation of a star cluster: predicting the properties of stars and brown dwarfs". In: *Mon. Not. R. Astron. Soc.* 339, pp. 577–599.

Bergin, E. A. & M. Tafalla (2007). "Cold Dark Clouds: The Initial Conditions for Star Formation". In: *Annual Review of Astronomy and Astrophysics* 45, pp. 339–396.

Bisbas, T. G., R. Wünsch, A. P. Whitworth, & D. A. Hubber (2009). "Smoothed particle hydrodynamics simulations of expanding H II regions. I. Numerical method and applications". In: *A&A* 497, pp. 649–659.

Bisbas, T. G., R. Wünsch, A. P. Whitworth, D. A. Hubber, & S. Walch (2011). "Radiation-driven Implosion and Triggered Star Formation". In: *ApJ* 736, 142, p. 142.

Blasi, P. (2013). "The origin of galactic cosmic rays". In: *Astronomy and Astrophysics Reviews* 21, 70, p. 70.

Bonnell, I. A., M. R. Bate, C. J. Clarke, & J. E. Pringle (2001). "Competitive accretion in embedded stellar clusters". In: *Mon. Not. R. Astron. Soc.* 323, pp. 785–794.

Bonnor, W. B. (1956). "Boyle's Law and gravitational instability". In: *Mon. Not. R. Astron. Soc.* 116, p. 351.

Bourke, T. L., P. C. Myers, G. Robinson, & A. R. Hyland (2001). "New OH Zeeman Measurements of Magnetic Field Strengths in Molecular Clouds". In: *ApJ* 554, pp. 916–932.

Brinks, E. (1990). "The cool phase of the interstellar medium - Atomic gas". In: *The Interstellar Medium in Galaxies*. Ed. by H. A. Thronson Jr. & J. M. Shull. Vol. 161. Astrophysics and Space Science Library, pp. 39–65.

Broos, P. S. et al. (2011). "A Catalog of Chandra X-ray sources in the Carina Nebula". In: *Astrophys. J. Supp.* 194, 2, p. 2.

Burgers, J. M. (1974). "Statistical problems connected with the one-dimensional nonlinear diffusion equation". In: *Acoustical Society of America Journal* 55, p. 50.

Burkert, A. & J. Alves (2009). "The Inevitable Future of the Starless Core Barnard 68". In: *ApJ* 695, pp. 1308–1314.

Butt, Y. (2009). "Beyond the myth of the supernova-remnant origin of cosmic rays". In: *Nature* 460, pp. 701–704.

Capriotti, E. R. & J. F. Kozminski (2001). "Relative Effects of Ionizing Radiation and Winds from O-Type Stars on the Structure and Dynamics of H II Regions". In: *PASP* 113, pp. 677–691.

Castor, J., R. McCray, & R. Weaver (1975). "Interstellar bubbles". In: *ApJ* 200, pp. L107–L110.

Cazaux, S. & A. G. G. M. Tielens (2004). "H_2 Formation on Grain Surfaces". In: *ApJ* 604, pp. 222–237.

Cernicharo, J. (1991). "The Physical Conditions of Low Mass Star Forming Regions". In: *NATO ASIC Proc. 342: The Physics of Star Formation and Early Stellar Evolution*. Ed. by C. J. Lada & N. D. Kylafis, p. 287.

Chabrier, G. (2003). "Galactic Stellar and Substellar Initial Mass Function". In: *PASP* 115, pp. 763–795.

Chabrier, G. (2005). "The Initial Mass Function: from Salpeter 1955 to 2005". In: *The Initial Mass Function 50 Years Later*. Ed. by E. Corbelli, F. Palla, & H. Zinnecker. Vol. 327. Astrophysics and Space Science Library, p. 41.

Clark, F. O. (1991). "Young stellar objects detected by IRAS". In: *Astrophys. J. Supp.* 75, pp. 611–628.

Clark, P. C., R. S. Klessen, & I. A. Bonnell (2007). "Clump lifetimes and the initial mass function". In: *Mon. Not. R. Astron. Soc.* 379, pp. 57–62.

Courant, R., K. Friedrichs, & H. Lewy (1967). "On the Partial Difference Equations of Mathematical Physics". In: *IBM Journal of Research and Development* 11, pp. 215–234.

Crutcher, R. M., N. Hakobian, & T. H. Troland (2009). "Testing Magnetic Star Formation Theory". In: *ApJ* 692, pp. 844–855.

Crutcher, R. M., N. Hakobian, & T. H. Troland (2010). "Self-consistent analysis of OH Zeeman observations". In: *Mon. Not. R. Astron. Soc.* 402, pp. L64–L66.

Dale, J. E. & I. A. Bonnell (2008). "The effect of stellar winds on the formation of a protocluster". In: *Mon. Not. R. Astron. Soc.* 391, pp. 2–13.

Dale, J. E., P. C. Clark, & I. A. Bonnell (2007). "Ionization-induced star formation - II. External irradiation of a turbulent molecular cloud". In: *Mon. Not. R. Astron. Soc.* 377, pp. 535–544.

Dale, J. E., J. Ngoumou, B. Ercolano, & I. A. Bonnell (2014). "Before the first supernova: combined effects of HII regions and winds on molecular clouds". In: *ArXiv e-prints*.

Dalgarno, A. & R. A. McCray (1972). "Heating and Ionization of HI Regions". In: *Annual Review of Astronomy and Astrophysics* 10, p. 375.

Daniel, K. J., J. L. Linsky, & M. Gagné (2002). "Chandra Observations of the Pleiades Open Cluster: X-Ray Emission from Late B- to Early F-Type Binaries". In: *ApJ* 578, pp. 486–502.

Deharveng, L., F. Schuller, L. D. Anderson, A. Zavagno, F. Wyrowski, K. M. Menten, L. Bronfman, L. Testi, C. M. Walmsley, & M. Wienen (2010). "A gallery of bubbles. The nature of the bubbles observed by Spitzer and what ATLASGAL tells us about the surrounding neutral material". In: *A&A* 523, A6, A6.

Dobbs, C. L., M. R. Krumholz, J. Ballesteros-Paredes, A. D. Bolatto, Y. Fukui, M. Heyer, M.-M. Mac Low, E. C. Ostriker, & E. Vázquez-Semadeni (2013). "Formation of Molecular Clouds and Global Conditions for Star Formation". In: *ArXiv e-prints*.

Draine, B. T. (2009). "Interstellar Dust Models and Evolutionary Implications". In: *Cosmic Dust - Near and Far*. Ed. by T. Henning, E. Grün, & J. Steinacker. Vol. 414. Astronomical Society of the Pacific Conference Series, p. 453.

Draine, B. T. & E. E. Salpeter (1979). "Destruction mechanisms for interstellar dust". In: *ApJ* 231, pp. 438–455.

Dwek, E. & J. M. Scalo (1980). "The evolution of refractory interstellar grains in the solar neighborhood". In: *ApJ* 239, pp. 193–211.

Dyson, J. E. & J. de Vries (1972). "The Dynamical Effects of Stellar Mass Loss on Diffuse Nebulae". In: *A&A* 20, p. 223.

Ebert, R. (1957). "Zur Instabilität kugelsymmetrischer Gasverteilungen. Mit 2 Textabbildungen". In: *Zeitschrift für Astrophysik* 42, p. 263.

Elmegreen, B. G. (1981). "The role of magnetic fields in constraining the translational motion of giant cloud complexes". In: *ApJ* 243, pp. 512–525.

Evans, N. R. et al. (2011). "The Search for Low-mass Companions of B Stars in the Carina Nebula Cluster Trumpler 16". In: *Astrophys. J. Supp.* 194, 13, p. 13.

Ferrarotti, A. S. & H.-P. Gail (2002). "Mineral formation in stellar winds. III. Dust formation in S stars". In: *A&A* 382, pp. 256–281.

Ferrière, K. (1998). "The Hot Gas Filling Factor in Our Galaxy". In: *ApJ* 503, pp. 700–716.

Ferrière, K. M. (2001). "The interstellar environment of our galaxy". In: *Reviews of Modern Physics* 73, pp. 1031–1066.

Field, G. B., D. W. Goldsmith, & H. J. Habing (1969). "Cosmic-Ray Heating of the Interstellar Gas". In: *ApJ* 155, p. L149.

Fierlinger, K. M., A. Burkert, R. Diehl, C. Dobbs, D. H. Hartmann, M. Krause, E. Ntormousi, & R. Voss (2012). "Molecular Cloud Disruption and Chemical Enrichment of

the ISM Caused by Massive Star Feedback". In: *Advances in Computational Astrophysics: Methods, Tools, and Outcome*. Ed. by R. Capuzzo-Dolcetta, M. Limongi, & A. Tornambè. Vol. 453. Astronomical Society of the Pacific Conference Series, p. 25.

Freyer, T., G. Hensler, & H. W. Yorke (2003). "Massive Stars and the Energy Balance of the Interstellar Medium. I. The Impact of an Isolated 60 M_{solar} Star". In: *ApJ* 594, pp. 888–910.

Freyer, T., G. Hensler, & H. W. Yorke (2006). "Massive Stars and the Energy Balance of the Interstellar Medium. II. The 35 M_{solar} Star and a Solution to the "Missing Wind Problem"". In: *ApJ* 638, pp. 262–280.

Frisch, U. & J. Bec (2000). "Burgulence". In: *eprint arXiv:nlin/0012033*.

Gaczkowski, B., T. Preibisch, T. Ratzka, V. Roccatagliata, H. Ohlendorf, & H. Zinnecker (2013). "Herschel far-infrared observations of the Carina Nebula complex. II. The embedded young stellar and protostellar population". In: *A&A* 549, A67, A67.

García-Arredondo, F., W. J. Henney, & S. J. Arthur (2001). "Hydrodynamic Simulations of Proplyd Bow Shocks". In: *ApJ* 561, pp. 830–842.

Garcia-Segura, G. & M.-M. Mac Low (1995). "Wolf-Rayet Bubbles. I. Analytic Solutions". In: *ApJ* 455, p. 145.

Garcia-Segura, G., M.-M. Mac Low, & N. Langer (1996a). "The dynamical evolution of circumstellar gas around massive stars. I. The impact of the time sequence Ostar -> LBV -> WR star." In: *A&A* 305, p. 229.

Garcia-Segura, G., N. Langer, & M.-M. Mac Low (1996b). "The hydrodynamic evolution of circumstellar gas around massive stars. II. The impact of the time sequence O star -> RSG -> WR star." In: *A&A* 316, pp. 133–146.

Gingold, R. A. & J. J. Monaghan (1977). "Smoothed particle hydrodynamics - Theory and application to non-spherical stars". In: *Mon. Not. R. Astron. Soc.* 181, pp. 375–389.

Górski, K. M., E. Hivon, A. J. Banday, B. D. Wandelt, F. K. Hansen, M. Reinecke, & M. Bartelmann (2005). "HEALPix: A Framework for High-Resolution Discretization and Fast Analysis of Data Distributed on the Sphere". In: *ApJ* 622, pp. 759–771.

Grellmann, R., T. Preibisch, T. Ratzka, S. Kraus, K. G. Helminiak, & H. Zinnecker (2013). "The multiplicity of massive stars in the Orion Nebula Cluster as seen with long-baseline interferometry". In: *A&A* 550, A82, A82.

Griffin, M. J. et al. (2010). "The Herschel-SPIRE instrument and its in-flight performance". In: *A&A* 518, L3, p. L3.

Gritschneder, M., T. Naab, S. Walch, A. Burkert, & F. Heitsch (2009). "Driving Turbulence and Triggering Star Formation by Ionizing Radiation". In: *ApJ* 694, pp. L26–L30.

Gritschneder, M., A. Burkert, T. Naab, & S. Walch (2010). "Detailed Numerical Simulations on the Formation of Pillars Around H II Regions". In: *ApJ* 723, pp. 971–984.

Güdel, M. & Y. Nazé (2009). "X-ray spectroscopy of stars". In: *Astronomy and Astrophysics Reviews* 17, pp. 309–408.

Gvaramadze, V. V., S. Röser, R.-D. Scholz, & E. Schilbach (2011). "4U 1907+09: an HMXB running away from the Galactic plane". In: *A&A* 529, A14, A14.

Gvaramadze, V. V., C. Weidner, P. Kroupa, & J. Pflamm-Altenburg (2012). "Field O stars: formed in situ or as runaways?" In: *Mon. Not. R. Astron. Soc.* 424, pp. 3037–3049.

Hamaguchi, K. et al. (2009). "A Smoking Gun in the Carina Nebula". In: *ApJ* 695, pp. L4–L9.

Harper-Clark, E. & N. Murray (2009). "One-Dimensional Dynamical Models of the Carina Nebula Bubble". In: *ApJ* 693, pp. 1696–1712.

Heiles, C. (1990). "Clustered supernovae versus the gaseous disk and halo". In: *ApJ* 354, pp. 483–491.

Heiles, C. & T. H. Troland (2003). "The Millennium Arecibo 21 Centimeter Absorption-Line Survey. II. Properties of the Warm and Cold Neutral Media". In: *ApJ* 586, pp. 1067–1093.

Hennebelle, P. & G. Chabrier (2008). "Analytical Theory for the Initial Mass Function: CO Clumps and Prestellar Cores". In: *ApJ* 684, pp. 395–410.

Hennebelle, P. & G. Chabrier (2009). "Analytical Theory for the Initial Mass Function. II. Properties of the Flow". In: *ApJ* 702, pp. 1428–1442.

Hennebelle, P. & R. Teyssier (2008). "Magnetic processes in a collapsing dense core. II. Fragmentation. Is there a fragmentation crisis?" In: *A&A* 477, pp. 25–34.

Hennebelle, P., B. Commerçon, M. Joos, R. S. Klessen, M. Krumholz, J. C. Tan, & R. Teyssier (2011). "Collapse, outflows and fragmentation of massive, turbulent and magnetized prestellar barotropic cores". In: *A&A* 528, A72, A72.

Heyer, M. H. & C. M. Brunt (2004). "The Universality of Turbulence in Galactic Molecular Clouds". In: *ApJ* 615, pp. L45–L48.

Huang, W. & D. R. Gies (2006). "Stellar Rotation in Young Clusters. I. Evolution of Projected Rotational Velocity Distributions". In: *ApJ* 648, pp. 580–590.

Hubber, D. A., C. P. Batty, A. McLeod, & A. P. Whitworth (2011). "SEREN - a new SPH code for star and planet formation simulations. Algorithms and tests". In: *A&A* 529, A27, A27.

Hubber, D. A., S. Walch, & A. P. Whitworth (2013a). "An improved sink particle algorithm for SPH simulations". In: *Mon. Not. R. Astron. Soc.* 430, pp. 3261–3275.

Hubber, D. A., S. A. E. G. Falle, & S. P. Goodwin (2013b). "Convergence of AMR and SPH simulations - I. Hydrodynamical resolution and convergence tests". In: *Mon. Not. R. Astron. Soc.* 432, pp. 711–727.

Jones, A. P., A. G. G. M. Tielens, D. J. Hollenbach, & C. F. McKee (1994). "Grain destruction in shocks in the interstellar medium". In: *ApJ* 433, pp. 797–810.

Jones, A. P., A. G. G. M. Tielens, D. J. Hollenbach, & C. F. McKee (1997). "The propagation and survival of interstellar grains". In: *American Institute of Physics Conference Series*. Ed. by T. J. Bernatowicz & E. Zinner. Vol. 402. American Institute of Physics Conference Series, pp. 595–613.

Klessen, R. S. (2011). "Star Formation in Molecular Clouds". In: *EAS Publications Series*. Ed. by C. Charbonnel & T. Montmerle. Vol. 51. EAS Publications Series, pp. 133–167.

Kobulnicky, H. A., M. J. Lundquist, A. Bhattacharjee, & C. R. Kerton (2012). "IRAS 03063+5735: A Bowshock Nebula Powered by an Early B Star". In: *AJ* 143, 71, p. 71.

Kolmogorov, A. (1941). "The Local Structure of Turbulence in Incompressible Viscous Fluid for Very Large Reynolds' Numbers". In: *Akademiia Nauk SSSR Doklady* 30, pp. 301–305.

Könyves, V. et al. (2010). "The Aquila prestellar core population revealed by Herschel". In: *A&A* 518, L106, p. L106.

Kouwenhoven, M. B. N., A. G. A. Brown, S. F. Portegies Zwart, & L. Kaper (2007). "The primordial binary population. II.. Recovering the binary population for intermediate mass stars in Scorpius OB2". In: *A&A* 474, pp. 77–104.

Kramer, C., J. Stutzki, R. Rohrig, & U. Corneliussen (1998). "Clump mass spectra of molecular clouds". In: *A&A* 329, pp. 249–264.

Kritsuk, A. G., C. T. Lee, & M. L. Norman (2013). "A supersonic turbulence origin of Larson's laws". In: *Mon. Not. R. Astron. Soc.* 436, pp. 3247–3261.

Krumholz, M. R., J. M. Stone, & T. A. Gardiner (2007). "Magnetohydrodynamic Evolution of H II Regions in Molecular Clouds: Simulation Methodology, Tests, and Uniform Media". In: *ApJ* 671, pp. 518–535.

Kudritzki, R.-P. & J. Puls (2000). "Winds from Hot Stars". In: *Annual Review of Astronomy and Astrophysics* 38, pp. 613–666.

Lada, C. J. & E. A. Lada (2003). "Embedded Clusters in Molecular Clouds". In: *Annual Review of Astronomy and Astrophysics* 41, pp. 57–115.

Lamers, H. J. G. L. M. & J. P. Cassinelli (1999). *Introduction to Stellar Winds*.

Langer, N. (2012). "Presupernova Evolution of Massive Single and Binary Stars". In: *Annual Review of Astronomy and Astrophysics* 50, pp. 107–164.

Larson, R. B. (1981). "Turbulence and star formation in molecular clouds". In: *Mon. Not. R. Astron. Soc.* 194, pp. 809–826.

Lequeux, J. (2005). *The Interstellar Medium*.

Lucy, L. B. (1977). "A numerical approach to the testing of the fission hypothesis". In: *AJ* 82, pp. 1013–1024.

Mac Low, M.-M. & M. L. Norman (1993). "Nonlinear growth of dynamical overstabilities in blast waves". In: *ApJ* 407, pp. 207–218.

Mac Low, M.-M., R. Klessen, & F. Heitsch (1999). "MHD Turbulence in Star-Forming Clouds". In: *Optical and Infrared Spectroscopy of Circumstellar Matter*. Ed. by E. Guenther, B. Stecklum, & S. Klose. Vol. 188. Astronomical Society of the Pacific Conference Series, p. 177.

Mackey, J., N. Langer, & V. V. Gvaramadze (2013). "Dynamics of H II regions around exiled O stars". In: *ArXiv e-prints*.

Massey, P. & J. Johnson (1993). "Massive stars near Eta Carinae - The stellar content of TR 14 and TR 16". In: *AJ* 105, pp. 980–1001.

Mathis, J. S., W. Rumpl, & K. H. Nordsieck (1977). "The size distribution of interstellar grains". In: *ApJ* 217, pp. 425–433.

Matsuura, M., A. A. Zijlstra, F. J. Molster, S. Hony, L. B. F. M. Waters, F. Kemper, J. E. Bowey, H. Chihara, C. Koike, & L. P. Keller (2004). "Polycyclic Aromatic Hydrocarbons and Crystalline Silicates in the Bipolar Post-Asymptotic Giant Branch Star IRAS 16279-4757". In: *ApJ* 604, pp. 791–799.

Matzner, C. D. & C. F. McKee (2000). "Efficiencies of Low-Mass Star and Star Cluster Formation". In: *ApJ* 545, pp. 364–378.

McKee, C. F. & E. C. Ostriker (2007). "Theory of Star Formation". In: *Annual Review of Astronomy and Astrophysics* 45, pp. 565–687.

McKee, C. F. & J. P. Ostriker (1977). "A theory of the interstellar medium - Three components regulated by supernova explosions in an inhomogeneous substrate". In: *ApJ* 218, pp. 148–169.

McSwain, M. V., S. M. Ransom, T. S. Boyajian, E. D. Grundstrom, & M. S. E. Roberts (2007). "Runaway Massive Binaries and Cluster Ejection Scenarios". In: *ApJ* 660, pp. 740–746.

Moeckel, N. & M. R. Bate (2010). "On the evolution of a star cluster and its multiple stellar systems following gas dispersal". In: *Mon. Not. R. Astron. Soc.* 404, pp. 721–737.

Mohamed, S., J. Mackey, & N. Langer (2012). "3D simulations of Betelgeuse's bow shock". In: *A&A* 541, A1, A1.

Monaghan, J. J. (1992). "Smoothed particle hydrodynamics". In: *Annual Review of Astronomy and Astrophysics* 30, pp. 543–574.

Monaghan, J. J. (1997). "SPH and Riemann Solvers". In: *Journal of Computational Physics* 136, pp. 298–307.

Monaghan, J. J. (2005). "Smoothed particle hydrodynamics". In: *Reports on Progress in Physics* 68, pp. 1703–1759.

Monaghan, J. J. & J. C. Lattanzio (1985). "A refined particle method for astrophysical problems". In: *A&A* 149, pp. 135–143.

Motte, F., P. Andre, & R. Neri (1998). "The initial conditions of star formation in the rho Ophiuchi main cloud: wide-field millimeter continuum mapping". In: *A&A* 336, pp. 150–172.

Mottram, J. C., M. G. Hoare, S. L. Lumsden, R. D. Oudmaijer, J. S. Urquhart, T. L. Sheret, A. J. Clarke, & J. Allsopp (2007). "The RMS survey: mid-infrared observations of candidate massive YSOs in the southern hemisphere". In: *A&A* 476, pp. 1019–1111.

Mouschovias, T. C. & E. V. Paleologou (1979). "The angular momentum problem and magnetic braking - an exact time-dependent solution". In: *ApJ* 230, pp. 204–222.

Nakamura, F. & Z.-Y. Li (2007). "Protostellar Turbulence Driven by Collimated Outflows". In: *ApJ* 662, pp. 395–412.

Ngoumou, J., T. Preibisch, T. Ratzka, & A. Burkert (2013). "The Mysterious Sickle Object in the Carina Nebula: A Stellar Wind Induced Bow Shock Grazing a Clump?" In: *ApJ* 769, 139, p. 139.

Ntormousi, E., A. Burkert, K. Fierlinger, & F. Heitsch (2011). "Formation of Cold Filamentary Structure from Wind-blown Superbubbles". In: *ApJ* 731, 13, p. 13.

O'Dell, C. R., W. J. Henney, N. P. Abel, G. J. Ferland, & S. J. Arthur (2009). "The Three-Dimensional Dynamic Structure of the Inner Orion Nebula". In: *AJ* 137, pp. 367–382.

Oey, M. S. & C. J. Clarke (2005). "Statistical Confirmation of a Stellar Upper Mass Limit". In: *ApJ* 620, pp. L43–L46.

Oey, M. S. & G. García-Segura (2004). "Ambient Interstellar Pressure and Superbubble Evolution". In: *ApJ* 613, pp. 302–311.

Ohlendorf, H., T. Preibisch, B. Gaczkowski, T. Ratzka, R. Grellmann, & A. F. McLeod (2012). "Jet-driving protostars identified from infrared observations of the Carina Nebula complex". In: *A&A* 540, A81, A81.

Osterbrock, D. E. & G. J. Ferland (2006). *Astrophysics of gaseous nebulae and active galactic nuclei*.

Ostriker, J. P. & C. F. McKee (1988). "Astrophysical blastwaves". In: *Reviews of Modern Physics* 60, pp. 1–68.

Padoan, P. & Å. Nordlund (2002). "The Stellar Initial Mass Function from Turbulent Fragmentation". In: *ApJ* 576, pp. 870–879.

Pauldrach, A. W. A., T. L. Hoffmann, & M. Lennon (2001). "Radiation-driven winds of hot luminous stars. XIII. A description of NLTE line blocking and blanketing towards realistic models for expanding atmospheres". In: *A&A* 375, pp. 161–195.

Pekruhl, S., T. Preibisch, F. Schuller, & K. Menten (2013). "The clump mass function of the dense clouds in the Carina nebula complex". In: *A&A* 550, A29, A29.

Peters, T., R. Banerjee, R. S. Klessen, & M.-M. Mac Low (2011). "The Interplay of Magnetic Fields, Fragmentation, and Ionization Feedback in High-mass Star Formation". In: *ApJ* 729, 72, p. 72.

Pikel'Ner, S. B. (1968). "Interaction of Stellar Wind with Diffuse Nebulae". In: *Astrophys. Lett.* 2, p. 97.

Poglitsch, A. et al. (2010). "The Photodetector Array Camera and Spectrometer (PACS) on the Herschel Space Observatory". In: *A&A* 518, L2, p. L2.

Pontefract, M. & J. M. C. Rawlings (2004). "The early chemical evolution of nova outflows". In: *Mon. Not. R. Astron. Soc.* 347, pp. 1294–1303.

Portegies Zwart, S. F., S. L. W. McMillan, & M. Gieles (2010). "Young Massive Star Clusters". In: *Annual Review of Astronomy and Astrophysics* 48, pp. 431–493.

Povich, M. S. et al. (2011). "A Pan-Carina Young Stellar Object Catalog: Intermediate-mass Young Stellar Objects in the Carina Nebula Identified Via Mid-infrared Excess Emission". In: *Astrophys. J. Supp.* 194, 14, p. 14.

Preibisch, T., Y. Balega, K.-H. Hofmann, G. Weigelt, & H. Zinnecker (1999). "Multiplicity of the massive stars in the Orion Nebula cluster". In: *New Astronomy* 4, pp. 531–542.

Preibisch, T. et al. (2005). "The Origin of T Tauri X-Ray Emission: New Insights from the Chandra Orion Ultradeep Project". In: *Astrophys. J. Supp.* 160, pp. 401–422.

Preibisch, T., F. Schuller, H. Ohlendorf, S. Pekruhl, K. M. Menten, & H. Zinnecker (2011a). "A deep wide-field sub-mm survey of the Carina Nebula complex". In: *A&A* 525, A92, A92.

Preibisch, T., T. Ratzka, B. Kuderna, H. Ohlendorf, R. R. King, S. Hodgkin, M. Irwin, J. R. Lewis, M. J. McCaughrean, & H. Zinnecker (2011b). "Deep wide-field near-infrared survey of the Carina Nebula". In: *A&A* 530, A34, A34.

Preibisch, T., S. Hodgkin, M. Irwin, J. R. Lewis, R. R. King, M. J. McCaughrean, H. Zinnecker, L. Townsley, & P. Broos (2011c). "Near-infrared Properties of the X-ray-emitting Young Stellar Objects in the Carina Nebula". In: *Astrophys. J. Supp.* 194, 10, p. 10.

Preibisch, T., V. Roccatagliata, B. Gaczkowski, & T. Ratzka (2012). "Herschel far-infrared observations of the Carina Nebula complex. I. Introduction and global cloud structure". In: *A&A* 541, A132, A132.

Price, D. J. (2007). "splash: An Interactive Visualisation Tool for Smoothed Particle Hydrodynamics Simulations". In: *Publ. Astron. Soc. Aust.* 24, pp. 159–173.

Price, D. J. (2012). "Smoothed particle hydrodynamics and magnetohydrodynamics". In: *Journal of Computational Physics* 231, pp. 759–794.

Price, D. J. & M. R. Bate (2007). "The impact of magnetic fields on single and binary star formation". In: *Mon. Not. R. Astron. Soc.* 377, pp. 77–90.

Price, D. J. & J. J. Monaghan (2007). "An energy-conserving formalism for adaptive gravitational force softening in smoothed particle hydrodynamics and N-body codes". In: *Mon. Not. R. Astron. Soc.* 374, pp. 1347–1358.

Reed, B. C. (2003). "Catalog of Galactic OB Stars". In: *AJ* 125, pp. 2531–2533.

Reynolds, R. J. (1991). "Ionized disk/halo gas - Insight from optical emission lines and pulsar dispersion measures". In: *The Interstellar Disk-Halo Connection in Galaxies*. Ed. by H. Bloemen. Vol. 144. IAU Symposium, pp. 67–76.

Roccatagliata, V., T. Preibisch, T. Ratzka, & B. Gaczkowski (2013). "Herschel far-infrared observations of the Carina Nebula complex. III. Detailed cloud structure and feedback effects". In: *A&A* 554, A6, A6.

Rosswog, S. (2009). "Astrophysical smooth particle hydrodynamics". In: *New Astronomy Review* 53, pp. 78–104.

Salpeter, E. E. (1955). "The Luminosity Function and Stellar Evolution." In: *ApJ* 121, p. 161.

Sana, H., Y. Momany, M. Gieles, G. Carraro, Y. Beletsky, V. D. Ivanov, G. de Silva, & G. James (2010). "A MAD view of Trumpler 14". In: *A&A* 515, A26, A26.

Schmitt, J. H. M. M., L. Golub, F. R. Harnden Jr., C. W. Maxson, R. Rosner, & G. S. Vaiana (1985). "An Einstein Observatory X-ray survey of main-sequence stars with shallow convection zones". In: *ApJ* 290, pp. 307–320.

Seab, C. G. & J. M. Shull (1983). "Shock processing of interstellar grains". In: *ApJ* 275, pp. 652–660.

Shu, F. H. (1991). *The physics of astrophysics. Volume 1: Radiation.*

Shu, F. H. (1992). *The physics of astrophysics. Volume II: Gas dynamics.*

Shu, F. H., F. C. Adams, & S. Lizano (1987). "Star formation in molecular clouds - Observation and theory". In: *Annual Review of Astronomy and Astrophysics* 25, pp. 23–81.

Smith, N. (2006). "A census of the Carina Nebula - I. Cumulative energy input from massive stars". In: *Mon. Not. R. Astron. Soc.* 367, pp. 763–772.

Smith, N. & K. J. Brooks (2008). "The Carina Nebula: A Laboratory for Feedback and Triggered Star Formation". In: *Handbook of Star Forming Regions, Volume II*. Ed. by B. Reipurth, p. 138.

Smith, N., J. Bally, & J. A. Morse (2003). "Numerous Proplyd Candidates in the Harsh Environment of the Carina Nebula". In: *ApJ* 587, pp. L105–L108.

Smith, N., R. H. Barbá, & N. R. Walborn (2004). "Carina's defiant Finger: HST observations of a photoevaporating globule in NGC 3372*". In: *Mon. Not. R. Astron. Soc.* 351, pp. 1457–1470.

Smith, N., J. Bally, & N. R. Walborn (2010a). "HST/ACS Hα imaging of the Carina Nebula: outflow activity traced by irradiated Herbig-Haro Jets". In: *Mon. Not. R. Astron. Soc.* 405, pp. 1153–1186.

Smith, N., M. S. Povich, B. A. Whitney, E. Churchwell, B. L. Babler, M. R. Meade, J. Bally, R. D. Gehrz, T. P. Robitaille, & K. G. Stassun (2010b). "Spitzer Space Telescope observations of the Carina nebula: the steady march of feedback-driven star formation". In: *Mon. Not. R. Astron. Soc.* 406, pp. 952–974.

Solomon, P. M., A. R. Rivolo, J. Barrett, & A. Yahil (1987). "Mass, luminosity, and line width relations of Galactic molecular clouds". In: *ApJ* 319, pp. 730–741.

Spitzer, L. (1978). *Physical processes in the interstellar medium.*

Springel, V. (2010a). "E pur si muove: Galilean-invariant cosmological hydrodynamical simulations on a moving mesh". In: *Mon. Not. R. Astron. Soc.* 401, pp. 791–851.

Springel, V. (2010b). "Smoothed Particle Hydrodynamics in Astrophysics". In: *Annual Review of Astronomy and Astrophysics* 48, pp. 391–430.

Starrfield, S., R. D. Gehrz, & J. W. Truran (1997). "Dust formation and nucleosynthesis in the nova outburst". In: *American Institute of Physics Conference Series*. Ed. by T. J. Bernatowicz & E. Zinner. Vol. 402. American Institute of Physics Conference Series, pp. 203–234.

Steigman, G., P. A. Strittmatter, & R. E. Williams (1975). "The Copernicus observations - Interstellar or circumstellar material". In: *ApJ* 198, pp. 575–582.

Stelzer, B., E. Flaccomio, T. Montmerle, G. Micela, S. Sciortino, F. Favata, T. Preibisch, & E. D. Feigelson (2005). "X-Ray Emission from Early-Type Stars in the Orion Nebula Cluster". In: *Astrophys. J. Supp.* 160, pp. 557–581.

Strömgren, B. (1939). "The Physical State of Interstellar Hydrogen." In: *ApJ* 89, p. 526.

Stutzki, J. & R. Guesten (1990). "High spatial resolution isotopic CO and CS observations of M17 SW - The clumpy structure of the molecular cloud core". In: *ApJ* 356, pp. 513–533.

Tapia, M., M. Roth, J. Bohigas, & P. Persi (2011). "Imaging study of NGC 3372, the Carina nebula - III. The properties of G287.47-0.54 (Tr 14-N4), an embedded young cluster and its associated H_2 emission". In: *Mon. Not. R. Astron. Soc.* 416, pp. 2163–2173.

Tatischeff, V. (2008). "Cosmic-ray acceleration in supernova shocks". In: *ArXiv e-prints.*

Taylor, G. (1950). "The Instability of Liquid Surfaces when Accelerated in a Direction Perpendicular to their Planes. I". In: *Royal Society of London Proceedings Series A* 201, pp. 192–196.

Townsley, L. K. et al. (2011a). "An Introduction to the Chandra Carina Complex Project". In: *Astrophys. J. Supp.* 194, 1, p. 1.

Townsley, L. K. et al. (2011b). "The Chandra Carina Complex Project: Deciphering the Enigma of Carina's Diffuse X-ray Emission". In: *Astrophys. J. Supp.* 194, 15, p. 15.

Townsley, L. K., P. S. Broos, Y.-H. Chu, R. A. Gruendl, M. S. Oey, & J. M. Pittard (2011c). "The Integrated Diffuse X-ray Emission of the Carina Nebula Compared to Other Massive Star-forming Regions". In: *Astrophys. J. Supp.* 194, 16, p. 16.

Tremblin, P., E. Audit, V. Minier, W. Schmidt, & N. Schneider (2012). "Three-dimensional simulations of globule and pillar formation around HII regions: turbulence and shock curvature". In: *A&A* 546, A33, A33.

Trumpler, R. J. (1930). "Absorption of Light in the Galactic System". In: *PASP* 42, p. 214.

Urquhart, J. S., A. L. Busfield, M. G. Hoare, S. L. Lumsden, A. J. Clarke, T. J. T. Moore, J. C. Mottram, & R. D. Oudmaijer (2007). "The RMS survey. Radio observations of candidate massive YSOs in the southern hemisphere". In: *A&A* 461, pp. 11–23.

Vishniac, E. T. (1983). "The dynamic and gravitational instabilities of spherical shocks". In: *ApJ* 274, pp. 152–167.

Walch, S. K., A. P. Whitworth, T. Bisbas, R. Wünsch, & D. Hubber (2012). "Dispersal of molecular clouds by ionizing radiation". In: *Mon. Not. R. Astron. Soc.* 427, pp. 625–636.

Wang, J. et al. (2011). "A Chandra ACIS Study of the Young Star Cluster Trumpler 15 in Carina and Correlation with Near-infrared Sources". In: *Astrophys. J. Supp.* 194, 11, p. 11.

Ward-Thompson, D. & A. P. Whitworth (2011). *An Introduction to Star Formation*.

Weaver, R., R. McCray, J. Castor, P. Shapiro, & R. Moore (1977). "Interstellar bubbles. II - Structure and evolution". In: *ApJ* 218, pp. 377–395.

Weidner, C. & P. Kroupa (2006). "The maximum stellar mass, star-cluster formation and composite stellar populations". In: *Mon. Not. R. Astron. Soc.* 365, pp. 1333–1347.

Westmoquette, M. S., J. D. Slavin, L. J. Smith, & J. S. Gallagher III (2010). "VLT/FLAMES-ARGUS observations of stellar wind-ISM cloud interactions in NGC 6357". In: *Mon. Not. R. Astron. Soc.* 402, pp. 152–160.

Wilkin, F. P. (1996). "Exact Analytic Solutions for Stellar Wind Bow Shocks". In: *ApJ* 459, p. L31.

Wilkin, F. P. (2000). "Modeling Nonaxisymmetric Bow Shocks: Solution Method and Exact Analytic Solutions". In: *ApJ* 532, pp. 400–414.

Williams, J. P., E. J. de Geus, & L. Blitz (1994). "Determining structure in molecular clouds". In: *ApJ* 428, pp. 693–712.

Wilson, T. L., K. Rohlfs, & S. Hüttemeister (2009). *Tools of Radio Astronomy*. Springer-Verlag.

Wolfire, M. G., D. Hollenbach, C. F. McKee, A. G. G. M. Tielens, & E. L. O. Bakes (1995). "The neutral atomic phases of the interstellar medium". In: *ApJ* 443, pp. 152–168.

Wolk, S. J. et al. (2011). "The Chandra Carina Complex Project View of Trumpler 16". In: *Astrophys. J. Supp.* 194, 12, p. 12.

Woosley, S. E., A. Heger, & T. A. Weaver (2002). "The evolution and explosion of massive stars". In: *Reviews of Modern Physics* 74, pp. 1015–1071.

Zacharias, N., C. T. Finch, T. M. Girard, A. Henden, J. L. Bartlett, D. G. Monet, & M. I. Zacharias (2012). "UCAC4 Catalogue (Zacharias+, 2012)". In: *VizieR Online Data Catalog* 1322, p. 0.

Zacharias, N., C. T. Finch, T. M. Girard, A. Henden, J. L. Bartlett, D. G. Monet, & M. I. Zacharias (2013). "The Fourth US Naval Observatory CCD Astrograph Catalog (UCAC4)". In: *AJ* 145, 44, p. 44.

Zuckerman, B. & N. J. Evans II (1974). "Models of massive molecular clouds". In: *ApJ* 192, pp. L149–L152.

Acknowledgements/Danksagung

The journey towards completing this doctoral thesis, has been very stimulating, challenging and formative. None of this work would have been possible without the help and support of a number of people, I am so very grateful to.

First, I thank my supervisor, Prof. Dr. Andreas Burkert for giving me the opportunity to learn and work in a fascinating research field, for communicating your enthusiasm and knowledge. I also thank Prof. Dr. Thomas Preibisch for all the support and the guidance, for including me in discussions, for sharing your insights and your knowledge and for helping me with my first publication. I learned so much.

To David Hubber and James Dale, I don't even know where to begin... There is so much I am grateful for. Thank you for sharing your experience and knowledge, for being so patient and forgiving, for letting me ask the most stupid questions and even more for actually answering them, for listening to me rambling and babbling. Your feedback, support and advice kept me going. Thank you David for explaining the rules of Rugby (Go Wales!!!) and for the cheese and wine parties. Thank you Jim and Emma for the beautiful hiking trips. It is always so much fun.

Thank you to Klaus Dolag for the support, for caring, for listening, for coffee and chocolate and for improving and expanding the computing resources at the USM. Thank you so much to Tadziu Hoffmann for the invaluable help and patience and for, literally, fixing everything. Thank you to Thorsten Ratzka and Matthias Gritschneder for the very helpful discussions. Thank you to Veronika Junk for helping me through my first years, I would not have made it so far without you. Thank you to Christian Alig for very helpful advice. Thank you to the entire CAST group and to the Young Stars and Star Formation group for the great discussions, the chats, the cakes, the coffees and teas, the beers. Thank you also to the entire USM.

This project was funded by the Deutsche Forschungsgemeinschaft, DFG PR 569/9-1. Additional support came from funds from the Munich Cluster of Excellence: "Origin and Structure of the Universe". The SPLASH software package Price (2007) was used to visualize the simulations.

Danke an meiner Familie, an Gonza, Bona, Sita, Helena, Zinzi, Joshua, Noni, Kemi und Amari. Ihr seid mein Zuhause. Danke an Tom und Pia für die Unterstützung. Vielen Dank liebe Caro für deine Fürsorge, dafür dass Du immer für mich da warst. Vielen Dank Olli für deine Freundschaft und für all die Hilfe.
Babak, ohne Dich hätte ich es nie geschafft. Danke für deine Unterstützung, danke für deine Geduld, danke für alles. ∞

خیلی ممنون عزیزم